Title: Stellate cells drive maturation of the entorhinal-hippocampal circuit

Authors: Flavio Donato[1*], R. Irene Jacobsen[1], May-Britt Moser[1] and Edvard I Moser[1*]

Affiliations:

1 Kavli Institute for Systems Neuroscience and Centre for the Biology of Memory, Norwegian University of Science and Technology, Olav Kyrres gate 9, MTFS, 7491 Trondheim, Norway.

*Correspondence to: flavio.donato@ntnu.no and edvard.moser@ntnu.no

Abstract:

The neural representation of space relies on a network of entorhinal-hippocampal cell types with firing patterns tuned to different abstract features of the environment. To determine how this network is set up during early postnatal development, we monitored markers of structural maturation in developing mice, both in naïve animals and after temporally restricted pharmacogenetic silencing of specific cell populations. We found that entorhinal stellate cells provide an activity-dependent instructive signal that drives maturation sequentially and unidirectionally through the intrinsic circuits of the entorhinal-hippocampal network The findings raise the possibility that a small number of autonomously developing neuronal populations operate as intrinsic drivers of maturation across widespread regions of cortex.

Main Text:

To create a neural representation of the external world, sensory stimuli are topographically mapped onto highly organized neural networks spanning multiple sensory areas in the neocortex (*1-4*). The early development of such topographical sensory representations depends strongly on spontaneous

and sensory-driven neural activity spreading bottom-up from sensory receptors to sensory cortices (*5-8*).

Like in the sensory systems, the brain's representation of space relies on an extended network of specialized cell types spanning multiple interconnected brain regions. Cell types involved in the representation of space include place cells in the hippocampus, and grid, border, head direction and speed cells in the medial entorhinal cortex (MEC) (*9*). Properties of these cells are thought to reflect the intrinsic connectivity of the MEC (*10*) as well as the unique unidirectional organization of entorhinal projections through the hippocampus (*11-14*) (Fig. S1A). However, in contrast to the primary sensory cortices, little is known about how the entorhinal-hippocampal microcircuit is assembled during development, or what role neural activity has in refining the connectivity and maturation of the circuit. Place, border and head direction cells exhibit adult-like features from the onset of spatial navigation at 2-3 weeks of age, (*15-18*), while the periodic firing pattern of grid cells emerges later, at approximately 4 weeks (*15, 16*). The spatial accuracy of place cells evolves with a similarly protracted time course (*15, 16, 19*), suggesting that early interactions between subregions of the network might be crucial for the eventual emergence of spatially specific firing.

With these parallels in mind, we sought to determine how structural elements of the entorhinal-hippocampal circuit are wired together during development. We monitored network-wide developmental changes in the expression of maturation-related anatomical markers, taking advantage of targeted pharmacogenetic silencing methods to determine whether activity in any elements of the circuit had particular functions in organizing maturation across the network as a whole. Our data show that the entorhinal-hippocampal circuit matures in a linear sequence that recapitulates excitatory information flow through the adult hippocampal network. Excitatory

activity at each stage of the circuit was necessary for the development of the following stages. Stellate cells in MEC-L2 were at the top of this developmental hierarchy, providing an instructive signal that drove maturation across the entire entorhinal-hippocampal network.

Stagewise maturation of the transverse hippocampal circuit.

To determine the temporal profile of maturation among identified populations of neurons in the entorhinal-hippocampal network, we first monitored the expression of doublecortin (DCX) in each area of the network during the first postnatal month. DCX is a microtubule-associated protein that is present in neuronal precursors and immature neurons, where it promotes dendritic growth, and is downregulated during the stabilization of synaptic connectivity at late developmental stages (*20, 21*). In adults, the protein is expressed only in immature neurons in areas with ongoing neurogenesis (*21*). Because of this unique association with immature neurons, we used DCX as a marker of the maturational state of different classes of entorhinal and hippocampal neurons. For each region or cell class, we quantified for every third day the fraction of neurons in which DCX expression had declined to undetectable levels (Fig. 1A and Fig. S1). We subsequently identified for each region or cell type the first day on which this fraction constituted 80% or more of the NeuN+ cells (Fig. 1C). The quantification was validated by testing it on entorhinal-hippocampal sections from adult mice (P90-P120). As expected, there were virtually no DCX+ neurons in any of the areas analyzed, in line with published values (*21*), except for the dentate gyrus, where adult neurogenesis accounts for DCX expression in progenitors and immature neurons (fraction of DCX+ cells: 0.05 ± 0.01, as in (*22*) (Fig. 1B).

DCX was expressed extensively in all entorhinal-hippocampal areas at P5 but subsequently declined (Fig. S1). Analysis of DCX levels revealed that the maturation was staggered between subregions of the circuit (Fig. 1C). Stellate cells in layer 2 of the medial entorhinal cortex (MEC-L2 St) were the first to mature (80% threshold crossed at P14), followed, in chronological order, by pyramidal cells in MEC layer 2 (MEC-L2 Pyr) and CA3 (P20), CA1 (P23), dentate gyrus (DG), subiculum (SUB), layer 5 of the medial (MEC-L5) and lateral (LEC-L5) entorhinal cortices (all P26), and, finally, layer 2 of the lateral entorhinal cortex (LEC-L2, > P30). Hierarchical clustering of the maturation curves for these areas identified synchronous maturation profiles for cell populations with similar synaptic distances from the stellate cells (Fig. 1D), suggesting that maturation occurred in successive waves through the intrinsic hippocampal circuit, with MEC-to-hippocampal directionality.

To support the DCX-based observations with an independent measure, we analyzed the time course of maturation in an inhibitory cell type. In fast-spiking interneurons, cytosolic expression of the protein parvalbumin (PV) has been correlated with their structural and functional maturation, as well as synaptic integration in the circuit (*23*). Thus we conducted a confocal-based analysis of PV expression in single neurons in each area of the entorhinal-hippocampal network (Fig. S1D, see Supplementary Methods). PV expression was staggered between regions in a sequence that mirrored the step-wise downregulation of DCX. MEC-L2 was the first area to upregulate PV expression (threshold set as in Fig. 1C, and crossed by P17), followed by CA3 (P20), CA1, MEC-L5, SUB and DG (all P26), LEC-L5 (P30), and LEC-L2 (> P30) (Fig. 1E and Fig. S1D).

Finally, as a third independent marker of maturation in the entorhinal-hippocampal neural circuit, we investigated synaptogenesis by assessing the increase in density of synaptic puncta in the

developing cortex. To estimate synaptic density, we performed immunological staining for the protein Bassoon (Bs), which localizes at the active zone of presynaptic nerve terminals (*24*). The local density of Bs puncta was normalized to the local density of puncta in the corresponding adult network (P90-120). Again, time courses were staggered between subregions and subpopulations in a sequence that matched the flow of information through the adult circuit. MEC-L2 was the first to demonstrate increased density of Bs puncta (threshold set as in Fig. 1C and crossed at P17), followed by CA3 (P20), CA1 (P23), DG, SUB, MEC-L5 and LEC-L5 (all P26), and finally LEC-L2 (> P30) (Fig. 1F).

Taken together, the data suggest that maturation of the hippocampal-entorhinal network follows a stereotyped sequence that recapitulates the stagewise unidirectional flow of information through the intrinsic hippocampal microcircuit. DG provided the only exception to this scheme. The temporal profile of maturation in dentate granule cells was closer to that of cells in the deep layers of the entorhinal cortex than to downstream CA3 (Fig. 1D). This exceptional time profile is in line with the late peak of neurogenesis in DG, which extends through the first postnatal week (*25, 26*).

Excitatory activity instructs stagewise circuit maturation.

The sequential maturation of the entorhinal-hippocampal circuit raises the possibility that maturation is caused by an instructive signal that originates at the first step in the sequence, in MEC-L2, and then propagates synaptically through the network over the course of many days. Such a signal could take the form of excitatory neural activity, which is known to shape the maturation of cortical columns in the sensory cortices (*4*). To determine if activity is necessary for maturation also in the entorhinal-hippocampal network, we used inhibitory DREADDs and

silenced cell populations at different stages of the circuit for up to 6 days during early postnatal development (Fig. S2A (*27*)). A viral mix targeting hM4D(Gi) to excitatory neurons was injected in entorhinal or hippocampal subregions in newborn pups (P1). Infected neurons were silenced two weeks after injection, from P14 to P20, when hM4D expression was extensive (Fig. S3A-C). hM4D receptors were activated by continuous delivery of the ligand CNO (1 mg/kg) through an osmotic minipump implanted subcutaneously on the pups' backs. Based on the anatomical spread and specificity of the infection (> 80% neurons infected in the target area, < 20% cells infected in off-target areas, Fig. S2B, C), we focused on three groups of animals, with either MEC-L2 specific, hippocampus-specific or LEC-specific DREADD expression. As expected if activity were silenced, CNO produced a decrease in the fraction of c-FOS+ cells in all areas expressing the viral construct. In the silenced groups, c-FOS was also reduced in downstream regions of the circuit (Fig. S3D).

The effect of silencing on circuit maturation was estimated at the end of the silencing window, on P20, by quantitative analysis of local DCX and PV expression as well as synaptic density. Silencing MEC-L2 prevented maturation across the whole entorhinal-hippocampal network. With the exception of the stellate cells of MEC-L2 itself, every cell population in the network exhibited significantly reduced levels of DCX– neurons at the end of the silencing window, when compared to non-silenced control animals (Fig. 2A and S4A, mean ± S.D., Student's t-test, t values from 4.7 to 70.0, P values < 0.0033, except for stellate cells, $t = 0.11$ and $P = 0.91$). In all areas, MEC-L2-specific silencing also prevented the maturation-related increase in PV expression (Fig. S4B, $t > 10.5$ and $P < 0.0001$), as well as the increase in the density of synaptic puncta (Fig. S4C, $t > 8.5$ and $P < 0.0001$). Taken together, these three lines of data suggest that excitatory activity from

MEC-L2 is necessary for maturation of cell populations across the entire entorhinal-hippocampal network.

In contrast, maturation in MEC-L2 was not affected when activity was inhibited during the same interval in the hippocampus (Fig. 2B, $t = 0.049$ and $P = 0.96$ for stellate cells, and $t = 1.3$ and $P = 0.22$ for pyramidal cells). However, after hippocampal inactivation, maturation was blocked in all areas within or downstream of the hippocampus (Fig. 2B, t from 7.4 to 68.5, $P < 0.0003$). The retarded maturation of these areas was also expressed by the blocked increase of PV+ neurons (Fig. S4D, $t > 10.1$ and $P < 0.0001$) and densities of synaptic puncta (Fig. S4E, $t > 8.515$ and $P < 0.0001$). PV+ neurons and synaptic puncta were not altered in MEC-L2 ($t = 0.18$, $P = 0.10$ and $t = 0.20$ and $P = 0.80$, respectively). These data suggest that excitatory activity from the hippocampus is necessary for the maturation of subfields within the hippocampus, as well as MEC-L5 and LEC, but dispensable for the maturation of the MEC-L2 circuit.

Finally, when inhibitory DREADDs were activated during the same time window in LEC, maturation was arrested only in LEC-L5 and LEC-L2, whereas no change in DCX could be observed in MEC or hippocampus (Fig. 2C, $t > 9.8$ and $P < 0.0001$ in LEC, but $t < 1.01$ and $P > 0.4$ elsewhere). The selective effect on maturation in LEC was confirmed by the failed increase of PV+ neurons in LEC-L5 and LEC-L2 (Fig. S4F, $t > 5.1$ and $P < 0.0001$ in LEC, but $t < 0.95$ and $P > 0.2$ elsewhere), as well as the absence of an increase in synaptic puncta in these two structures (Fig. S4G, $t > 8.1$ and $P < 0.0001$ in LEC, but $t < 1.5$ and $P > 0.52$ elsewhere). These data imply that excitatory activity in LEC is necessary for maturation in LEC itself, but not for the rest of the entorhinal-hippocampal network.

Topography of MEC maturation.

We next focused on the local circuit of the MEC. Quantification of DCX expression in deep and superficial MEC layers showed that maturation proceeds from dorsal to ventral in all layers. This developmental gradient confirms a previous observation (*28*) but extends it in the sense that DCX could here be monitored at single cell resolution, with clear differentiation between stellate and pyramidal cells. Our analysis showed that, at every dorso-ventral position, maturation of MEC-L2 stellate cells precedes that of pyramidal cells in layers 2 and 5 (Fig. 3A, B and Fig. S5). The lag between stellate and layer 2 pyramidal cells was 3-6 days, whereas layer 5 neurons were delayed by a further 3-6 days (2-way ANOVA, neuronal subpopulation × Postnatal Day, including comparisons at every segment along the MEC: $F(7, 32) > 22.3$, $P < 0.0001$). The progression of maturation from dorsal to ventral MEC was also observed in PV-expressing interneurons, in superficial as well as deep layers (Fig. S5, direct comparison between block I and more ventral segments: Group × Segment: $F(7, 32) > 14.2$, $P < 0.0001$).

To investigate whether the instructive signal that drives maturation through the transverse circuit is also responsible for maturation of the MEC, we silenced layer 2 cells in the MEC using inhibitory DREADDs in the same way as in the transverse study. Silencing excitatory neurons in MEC-L2 did not change DCX levels in stellate cells at any dorso-ventral level of the MEC (Fig. 3C, left panel, Group (silenced vs. control): $F(1,32) = 2.54$, $P = 0.81$; Group × Segment: $F(7, 32) = 0.42$, $P = 0.87$). In contrast, the maturation-related increase in DCX– pyramidal cells was prevented along the entire dorso-ventral MEC axis (Fig. 3C, central panel, MEC-L2 silencing in green, controls in black, 2-way ANOVA: $F(7, 32) = 15.9$, $P < 0.0001$). Silencing excitatory activity in MEC-L2 also affected PV expression in interneurons (Fig. 3C, right panel, Group × Segment: $F(7, 32) = 21.6$, P

< 0.0001). The effect of inactivating MEC-L2 cells was dependent on the fraction of local excitatory cells infected (Fig. S6A), regardless of their dorso-ventral location. In all animals, the proportion of infected stellate and pyramidal cells was comparable to the overall proportion of these cell types in the network (Fig. S2D).

In contrast to the rest of the MEC network, the maturation of stellate cells was not affected by silencing excitatory activity in any of the multiple regions they receive input from. We tested whether the maturation of stellate cells was affected when excitatory activity was silenced widely across areas of the ipsilateral retrohippocampal cortex that have projections to MEC-L2, such as postrhinal cortex and parasubiculum. Despite a significant disruption of maturation in pyramidal and parvalbumin neurons after silencing in these animals (Fig. 3C and S6C, central and right panel, respectively; Group: $F(1,32) < 2.78$, $P > 0.082$; Group × Segment: $F(7, 32) > 7.42$, $P < 0.001$), there was still no effect on the fraction of DCX– stellate cells (Fig. 3C and S6C, left panel, Group: $F(1,32) = 0.98$, $P = 0.93$; Group × Segment: $F(7, 32) = 2.30$, $P = 0.07$), suggesting that stellate cells mature independently of activity in major afferent cell populations to MEC-L2. Further support for this conclusion comes from the observation that downregulation of DCX expression in either stellate or pyramidal cells, or upregulation of PV expression in the interneuron population, was unaffected when MEC was selectively deprived of homotopic contralateral inputs (Fig. S6B).

We next asked if the blockade of stellate-cell maturation was ineffective because these cells or their inputs were silenced too late, given that the dorsal tip of MEC is already mature by P14. Silencing dorsal MEC-L2 or a larger portion of the ipsilateral retrohippocampal cortex between P11 and P14, before the network is mature (Fig. 1C, E), did not produce any effect on the fraction of stellate cells expressing DCX at P14 (Fig. 3D, left panel). This result is corroborated by data from the ventral

MEC. Although the ventral MEC network is still largely immature at P14-P20, the maturation of stellate cells was not affected by silencing the MEC or upstream areas between P14 and P20 (Fig. 3C and Fig. S6C). Taken together, these experiments rule out activity in MEC-L2 or afferent cell populations as an origin of the maturation signal for MEC-L2 stellate cells.

Finally, it is possible that the stagnation in DCX and PV levels after MEC-L2 silencing reflected not delayed maturation but a functional impairment of pyramidal cells and interneurons. To address this possibility, we investigated whether the network was still able to progress through maturation if the brake induced by silencing was relieved. Specifically, we allowed a set of animals to recover from MEC inactivation by removing the osmotic minipump and thereby ending CNO delivery at P20 (Fig. S7A). In these animals, after 6 days of recovery, the maturation of pyramidal cells and fast spiking interneurons was indistinguishable from controls, i.e. hM4D-expressing, saline-injected animals (DCX expression in Fig. S7B, Group: $F(1,32) = 2.84$, $P = 0.12$, Group × Segment: $F(7, 32) = 1.60$, $P = 0.10$; PV expression in Fig. S7B, Group: $F(1,32) = 1.26$, $P = 0.42$, Group × Segment $F(7, 32) = 0.51$, $P = 0.43$,). At an intermediate time point (P23, 3 days of recovery), DCX and PV expression levels were between those found in control animals and animals silenced without recovery (Group × Segment $F(7, 32) > 7.2$, $P < 0.03$, Fig. S7C). Surprisingly, in the recovering cohort of animals at P23, there was no dorso-ventral topography in the maturation of pyramidal cells or PV+ interneurons (flat curves in Fig. S7D, slope of the linear regression along MEC is near 0, Student's t-test, $t > 6.12$ and $P < 0.001$ when compared to age-matched controls, Fig. S7E), suggesting that the activity signal that is necessary for driving maturation sequentially through the transverse entorhinal-hippocampal circuit may also participate in setting up the dorso-ventral topography of pyramidal cells and PV+ interneurons in MEC-L2. As expected, stellate cells were not affected by the recovery from MEC silencing (Fig. S7B, C: $F(7, 32) < 0.82$, $P > 0.81$).

Maturation of stellate cells correlates with birthdate.

The silencing experiments suggest that maturation of stellate cells occurs independently of local excitatory activity, and that it might instead rely on a signal intrinsic to these cells. A strong predictor of maturation may be the cells' birthdate. Neurogenesis initiates a cascade of cell-autonomous transcriptional events that direct the differentiation of neurons in a stereotyped manner (*29*). If the timing of maturation in stellate cells was determined by neurogenesis, we would expect cells to be topographically arranged according to birthdate along the dorso-ventral MEC axis, with the oldest neurons at the dorsal end and the youngest ventrally. To test this prediction, we injected BrdU during gestation to quantify the proportion of local cells that underwent cell division at the time of injection, and then mapped their distribution in the adult (Fig. 4A and Fig. S8A).

Our analysis revealed that while entorhinal pyramidal cells and parvalbumin interneurons were distributed randomly with respect to birthdate (Fig. 4B, C, and Fig. S8B respectively. 2-way ANOVA, Segment × Injection Day: $F(7, 36) = 0.23$, $P = 0.98$ for pyramidal cells, and $F(7, 36) = 0.15$, $P = 0.87$ for PV+ interneurons), stellate cells exhibited an orderly birthdate-dependent distribution along the dorso-ventral MEC axis. Early-born stellate cells were prevailingly (but not exclusively) located at the dorsal MEC pole, whereas later-born cells were found at progressively more ventral positions (Fig. 4B, C, Fig. S8C, 2-way ANOVA with Segment and Injection Day as factors: $F(7, 36) = 105.32$, $P < 0.0001$; for each segment: $F(5, 24) > 4.301$, $P < 0.006$).

To verify the association between the topographies of neurogenesis and maturation, we further analyzed DCX expression in "isochronic cells" – cells that were born on the same day (*29*). If

maturation is entirely dependent on neurogenesis, then the fraction of DCX– cells should be at comparable levels among isochronic neurons, independent of their dorso-ventral location. We found that among E13-born stellate cells there was no effect of dorso-ventral location on the fraction of DCX– cells (Fig. 4D left, 2-way ANOVA with Segment for each of the three time points: $F < 0.837$ and $P > 0.3$). In contrast, among E13-born pyramidal cells, the fraction of DCX– cells remained correlated with anatomical position (Fig. 4D right, 2-way ANOVA, only Segment considered: $F > 29.8$ and $P > 0.0001$). This experiment confirms that maturation of stellate cells, but not pyramidal cells, is intrinsically correlated with birthdate.

Stellate cells drive stagewise network maturation.

Because the silencing experiments point to local excitatory activity in MEC-L2 as the main drive for pyramidal cell maturation, we next asked if stellate cells might be the source. To achieve cell type-specific silencing, we exploited the staggered neurogenesis of stellate and pyramidal cells (Fig. S8D). Since nearly all dorsal MEC cells from early isochronic cohorts are stellate cells, whereas those from late cohorts are predominantly pyramidal cells, it should be possible to distinguish between them by labelling cells either at the beginning or end of the neurogenesis window for dorsal MEC.

In order to gain genetic access to cells born within specific time windows during neurogenesis, we developed a method based on in utero injection of an insertion-deficient, recombinant adeno-associated virus into the lateral ventricle of the developing brain (Fig. S9A). The localization of the virus to the ventricle allowed for selective targeting of the viral construct to post-mitotic cells that had not yet at the time of infection migrated out of the ventricular zone where they were born

(Fig. S9A). Using a double viral-BrdU approach, we found that the method was specific in targeting cells born on the day of the viral injection in MEC-L2, within a time window of 24-32 hours (Fig. S9B, D). The method was validated on sections from visual cortex, where, as expected, neurogenesis showed an inside-out progression, with E12 injections only labelling cells in the deepest layers and E16 injections targeting exclusively cells in superficial layers (*30, 31*) (Fig. S9E). In MEC, the topographical distribution and dorso-ventral progression of neurogenesis was identical in BrdU and virally identified cohorts (Fig. S9F).

Using the viral approach, we were able to test the hypothesis that activity in stellate but not pyramidal cells is necessary for driving maturation throughout the entorhinal-hippocampal circuit. We first injected a Cre virus (AAV1-CaMKII-Cre) into the lateral ventricle at either E12 or E16, to prime isochronic cohorts of cells to express the recombinase Cre. Then, at P1, we targeted the inhibitory DREADD hM4D(Gi) to primed cells by injecting the Cre-dependent virus in MEC-L2. Finally, during multiple time windows of postnatal maturation we delivered CNO through osmotic minipumps, as in the previous experiments (Fig. 5A). Both cohorts of animals received CNO during a time window of 3 days (w1: from P14 to P17; w2: P17 to P20; w3: P20 to P23; w4: P23 to P26). We silenced early-born neurons (E12 labelled) during early (w1 and w2) and late (w3) windows of maturation (Fig. S11), and late-born neurons during early (w2) and late (w3 and w4) windows (Fig. S12). As expected, in the most dorsal part of the MEC, the composition of the labelled cohort was dominated by stellate cells when the injection was performed at E12 (Fig. 5B and S10A, 96% of infected cells colocalized with reelin). In contrast, pyramidal cells predominated when the viral mix was injected at E16 (Fig. 5B and S10A, 92% of infected cells colocalized with calbindin). Thus, at the dorsal pole of the MEC, silencing of E12-born cells inactivated almost exclusively stellate cells, whereas silencing of E16-born cells inactivated almost only pyramidal

cells. The two approaches labelled comparable fractions of neurons in the overall layer 2 network (Fig. S10B. Student's t-test, $t = 0.72$ and $P = 0.98$).

Inactivation during postnatal maturation revealed that stellate cell-specific silencing was sufficient to block maturation of pyramidal cells in MEC-L2 (Fig. S11A, 2-way ANOVA with Group and Segment as factors: Group: $F(1,32) = 27.01$, $P < 0.001$, Group × Segment: $F(7, 32) = 83.9$, $P < 0.0001$). In a similar fashion, silencing stellate cells born at E12 prevented maturation of PV+ interneurons (Fig. S11A, Group: $F(1,32) = 15.92$, $P < 0.001$; Group × Segment $F(7, 32) = 64.20$, $P < 0.0001$). As expected from the global layer 2 interventions described earlier, the stellate cells themselves were not affected (Fig. S11A, Group: $F(1,32) = 0.981$, $P = 0.78$; Group × Segment $F(7, 32) = 2.30$, $P = 0.30$).

In contrast, pyramidal cell-specific inactivation did not affect the expression of DCX in the pyramidal cells themselves (Fig. S12C, Group: $F(1,32) = 1.59$, $P = 0.32$; Group × Segment: $F(7, 32) = 0.73$, $P = 0.51$) or in stellate cells (Fig. S12C, 2-way ANOVA, Group: $F(1,32) = 1.72$, $P = 0.25$; Group × Segment: $F(7, 32) = 0.98$, $P = 0.23$), and did not affect PV expression in interneurons (Fig. S12C, 2-way ANOVA, Group: $F(1,32) = 2.12$, $P = 0.08$; Group × Segment: $F(7, 32) = 1.04$, $P = 0.50$). To test if the ineffectiveness of pyramidal cell silencing was dependent on the timing of CNO delivery, we delivered CNO in adjacent time windows in a parallel set of experiments. No significant difference in DCX or PV expression could be detected between silenced and control animals when CNO was delivered in a time-unmatched fashion, with either stellate cell-specific silencing (Fig. 11B, C; Group: $F(1,32) < 1.59$, $P > 0.70$; Group and Segment as factors; pyramidal cells or interneurons vs. their controls: $F(7, 32) < 1.654$, $P > 0.54$), or with selective silencing of pyramidal cells (Fig. S12A, B; Group: $F(1,32) < 2.13$, $P > 0.15$; Group × Segment: $F(7, 32) <$

2.124, P > 0.30). Collectively, these experiments suggest that activity in stellate but not pyramidal cells is necessary for the maturation of the local network in MEC-L2.

The localization of the instructive signal in MEC to stellate cells raises the question of whether activity from isochronic stellate cells might also be necessary for the sequential maturation across subdivisions of the transverse entorhinal-hippocampal circuit. Silencing isochronic stellate cells was sufficient to prevent the maturation-associated downregulation of DCX in every area of the network (Fig. 5C and Fig. S13A, all comparisons with Student's t-test were significant, t > 7.44 and P < 0.01, with the exception of LEC-L2, t = 0.36 and P = 0.7, where most cells were in an immature state in the control condition too). Silencing stellate cells was also sufficient to decrease PV expression throughout the entorhinal-hippocampal loop (Fig. S13B, left panel; all comparisons were significant, t > 6.23 and P < 0.01, with the exception of LEC-L5 and LEC-L2, t < 0.13 and P > 0.15). Synaptogenesis was similarly retarded (Fig. S13B, right panel; all comparisons were significant, t > 4.71 and P < 0,01). In striking contrast, silencing isochronic pyramidal cells did not exert any effect on maturation of the entorhinal-hippocampal transverse circuit (Fig. 5D and Fig. S13A, C, t < 1.03 and P > 0.34). We also silenced stellate cells at later time points, between P20 and P23, after maturation of their postsynaptic partners is complete. This had no effect on DCX expression at any stage of the entorhinal-hippocampal network (Fig. S13D, t < 2.41 and P > 0.72), suggesting that the instructive role that stellate cells have on entorhinal-hippocampal circuit maturation is temporally limited.Taken together, the results identify stellate cells as the source of the activity-dependent instructive signal that drives the sequential maturation of the entorhinal-hippocampal network.

Isochronic cohorts of neurons act synergistically.

By exploiting our method to genetically label isochronic cohorts of neurons, we were able to show that silencing a small fraction of the MEC-L2 network is sufficient to interfere with maturation of the entorhinal-hippocampal circuit only if the silenced cohort predominantly consists of stellate cells (Fig. 5). At first glance, this observation is at odds with the observation in one of the earlier experiments that maturation requires silencing of more than 20% of the MEC-L2 cell population (Fig. S6A). One major difference between the two sets of experiments is that cells infected in utero were not randomly drawn from the network, but were born on the same day. If isochronic cells act synergistically during development, silencing a small, but isochronic, fraction of the network might be sufficient to efficiently affect network maturation. To test this idea, we silenced the isochronic cohort of MEC-L2 excitatory cells born on E12 and compared the result with the silencing of a comparable fraction of neurons whose labelling was independent of neurogenesis (Fig. S14A). The E12 isochronic cohort was primed for silencing in utero, and then targeted with the Cre-dependent hM4D(Gi) receptor at P1, before delivery of CNO during postnatal development (Fig. S14A, "Isochronic cells"). To label a comparable fraction of neurons randomly, we injected a mix of AAVs targeting hM4D(Gi) to excitatory cells postnatally, at P1, in order to avoid any bias to birthdate Fig. S14A, "Random cells"). The viruses were injected in proportions that allowed labelling of a sparse cohort of neurons, targeting a fraction of the L2 network ("Random cells – entire network"), or a fraction of the stellate cells in MEC-L2 ("Random cells – stellate cells"), that was comparable to the isochronic cohort.

Partial silencing of MEC-L2 was sufficient to affect DCX expression in pyramidal cells and PV expression in interneurons only if the targeted neurons were born on the same day, and not if they were drawn randomly with respect to their birthdate (Fig. 6, Group × Segment: $F(7, 32) > 5.86$, P

> 0.001; Group: $F(1,32) > 83.90$; $P < 0.0001$ for isochronic cells, $F(7, 32) < 1.78$, $P > 0.09$; Group: $F(1,32) < 0.42$, $P > 0.87$ for random cells). The effect of silencing was specific to the earliest window of circuit maturation (w1, Fig. 6); no effect was observed when CNO was delivered at later time points (w2 and w3, Fig. S14C, Group × Segment: $F(7, 32) < 0.38$, $P > 0.62$; Group: $F(1,32) < 3.22$, $P > 0.061$). In agreement with previous findings, stellate cells were not affected by silencing during any window of CNO delivery (Fig. 6 and Fig. S14C, Group: $F(1,32) < 1.38$, $P > 0.211$; Group × Segment: $F(7, 32) < 0.61$, $P > 0.8$). Taken together, these results indicate that isochronic cohorts of neurons in MEC-L2 exert a synergistic effect on microcircuit maturation.

Discussion.

We have shown that the entorhinal-hippocampal network matures in a stereotyped and directional sequence that, with the exception of the dentate gyrus, recapitulates the intrinsic excitatory connectivity of the hippocampal transverse circuit. At every level of the circuit, maturation and synaptogenesis rely on an excitatory activity-dependent instructive signal that originates in stellate cells of the MEC and spreads directionally throughout the circuit over the course of the first month of postnatal life. Stellate cells, being the first to mature, initiate maturation of the network by providing excitatory drive to their synaptic targets. These, in turn, subsequently exert a driving effect on areas further downstream, resulting in successive, stagewise maturation of the transverse entorhinal-hippocampal circuit. Maturation of stellate cells themselves is independent of local and incoming excitatory activity but correlates with birthdate, pointing to cell-autonomous molecular, genetic or epigenetic pathways, set up before birth, as potential sources of stellate-cell-initiated maturation in the entorhinal-hippocampal circuit.

In line with the role that sensory-driven activity exerts in the primary sensory cortices, stellate cells might influence computation in the entorhinal-hippocampal network by orchestrating the refinement of connectivity within MEC and hippocampus, as well as between these structures. By driving structural maturation of the interneuron network and of the backprojections from the hippocampus, stellate cells might serve as a developmental teaching layer to ensure strong coupling among cells that exhibit correlated neural activity in stimulus space (*32*). This may be crucial for the development of attractor network topologies thought to underlie the formation of grid patterns (*10, 32-36*).

The progression of neurogenesis and maturation along the dorso-ventral MEC axis may account for the topographic and modular organization of grid scale in grid cells along this axis. Moreover, because of the quantal nature of proliferation in neural progenitor cells (*37*), neurogenesis may contribute to discretization of grid cells into modules (*38*). The production of consecutive generations of "daughter cells" during neurogenesis may parcel stellate cells into cohorts that each are composed of neurons born on the same day ("isochronic cells"). Such waves of simultaneously born stellate cells may give rise to parallel networks with unique features, set up in ways that mirror the formation of parallel microcircuits of selectively interconnected neurons in the hippocampal trisynaptic loop (*26, 39*). These subnetworks born at different times might correspond to the modules of grid cells, which have a similar anatomical distribution as the cohorts presented here (*38*).

The nature of the instructive signal spreading through the network and driving local circuit maturation remains to be determined. Specific spatial or temporal patterns of depolarization in the network might be required to elicit post-synaptic responses leading to synaptogenesis and

maturation. One candidate activity pattern is the orchestrated change of calcium concentrations across populations of neurons defined as “calcium waves”, which has been implicated in the establishment of topography in sensory areas (*40, 41*). In the entorhinal-hippocampal circuit, isochronic neurons may exhibit similarly synchronized activity. Such activity may pattern network maturation stage by stage across the circuit (*42*). Isochronic neurons might exert a synergistic effect on maturation because of their tight temporal coupling during waves.

Our data show that stellate cells are at the top of the developmental hierarchy that instructs the linear sequence of maturation of the entorhinal-hippocampal circuit. Peripheral sensory organs have long been studied as the source of instructive signals driving the early development of the forebrain. For example, the olfactory organ instructs the central nervous system to reach its mature states (*43-45*), and in a similar fashion, thalamocortical axons are involved in cortical regionalization and the refinement of dendritic arborization and connectivity in the visual, somatosensory and auditory systems (*46, 47*). While activity from sensory organs provides a clear directionality to the maturation of cortical columns in sensory areas, we show here that in the entorhinal-hippocampal circuit, it is activity from stellate cells that drives the maturation of the entire circuit. Our data identify a network where such instructive excitatory activity does not originate from sensory neurons, but is provided by a subpopulation of neurons that functions as an “autonomous” intrinsic driver in a neurogenesis-dependent manner. The presence of a few of these intrinsic drivers in the brain during development might be particularly influential for the coordinated maturation of networks that are positioned at a great synaptic distance from sensory signals and extend across multiple areas in the associative cortices, thereby shaping network topologies supporting higher cognitive function.

Materials and Methods.

All experiments were performed in accordance with the Norwegian Animal Welfare Act and the European Convention for the Protection of Vertebrate Animals used for Experimental and Other Scientific Purposes, Permit numbers 6021, 6008 and 7163. C57/Bl6 mice were housed in social groups of 2-6 individuals per cage under a 12h light/12h darkness schedule, in a temperature- and humidity-controlled vivarium. Food and water were provided ad libitum.

Viral injections.

For all surgeries, on the day of the injection, anesthesia was induced by placing the subjects in a plexiglass chamber filled with isofluorane vapor (5% isofluorane in medical air, flow of 1 liters/minute). Surgery was performed on a heated surgery table (38°C), air flow was kept at 1 liters/minute with 1.5-3% isofluorane as determined from physiological monitoring of vital signs (breathing and heartbeat). Analgesics were provided immediately before the surgery (Rymadil, Pfizer, 5 mg/kg). After each procedure, subjects were allowed to recover in a heated chamber (33°C, 30-90 minutes) until they regained complete mobility and alertness.

Viral injections at P1.

Newborn pups were subjected to viral injection 1 day after birth (P1). Pre-heated ultrasound gel (39°C, Aquasonic 100, Parker) was generously applied on the pup's head in order to create a large medium for the transmission of ultrasound waves. Real-time ultrasound imaging (Vevo 1100 System, Fujifilm Visualsonics) allowed for targeted delivery of the viral mixture to specific areas. For imaging, the ultrasound probe (MS-550S) was lowered to be in close contact with the gel to allow visualization of the targeted structures, and was kept in place for the whole duration of the procedure via the VEVO injection mount (VEVO Imaging Station. Imaging in B-Mode, frequency:

40 MHz; power: 100%; gain: 29 Db; dynamic range: 60 Db). Target regions were identified by structural landmarks: the hippocampus was identified by the cytoarchitecture of CA3 and the appearance of the lateral ventricle (target area for injection was comparable to a coronal section at -1.46 mm from bregma in the adult animal (*48*)); the MEC and LEC were identified by the appearance of the aqueduct of Sylvius and the lateral sinus (target area for injection was comparable to a coronal section at -4.72 mm from bregma in the adult animal (*48*)).

A viral mixture (250 ± 50 nl per injection) was injected in the target regions via beveled glass micropipettes (Origio, custom made. Outer tip opening: 200 µm. Inner tip opening: 50 µm) with a pressure-pulse system (Visualsonics, 5 pulses, 50 nl per pulse). The anatomical specificity of the infection was verified by imaging serial sections of the infected hemispheres after experiment completion.

Virus injection in the embryo.

Pregnant females were subjected to the viral injection on a specific day of gestation, from E10 to E17. To achieve precise monitoring of gestation, a mating trio (one male and two females) was allowed to interact for a limited period of time (24 hours), after which the male was removed from the cage to prevent further mating. E1 was defined as the day on which the male was removed (vaginal plug could be observed in most of the cases). A longitudinal incision was performed on the shaved skin and peritoneum of the isoflurane anaesthetized female to reach the uterine horns. The abdominal cavity was kept irrigated with warm saline solution (0.9% NaCl, 39°C) for the entire procedure. Single embryos weretransferred one-by-one to a custom made, sterile surgical chamber to allow for viral injection. Pre-heated ultrasound gel (39°C, Aquasonic 100, Parker) was generously applied to the embryos. Real-time ultrasound imaging (parameters as above) allowed

for targeted delivery of the viral mixture to the lateral ventricle of the developing brain. The viral solution (containing AAV1-CaMKII-Cre; 150-350 nl per injection) was applied as previously described (UPenn Vector Core, University of Pennsylvania, Perelman School of Medicine). After injection, the ultrasound gel was removed with sterile gauze and the embryo placed back into the abdominal cavity. This procedure was repeated for all the other embryos in the litter. After injection of the last embryo, two independent sets of stitches were applied to the peritoneum and abdominal skin. The total length of the procedure was limited to less than 90 minutes to avoid unnecessary stress to the mother and the embryos. 80% of the injected embyros survived injection and delivery, and could be utilized for further studies.

Pharmacogenetic silencing.

On P11 or P14, a longitudinal incision was performed on the shaved skin of the isoflurane anaesthetized pup's back in order to allow for the insertion of a minipump subcutaneously. Warm saline solution (0.9% NaCl, 39°C) was injected subcutaneously in the area of the incision at multiple times during the minipump implant. The osmotic minipump (Alzet, 1007D: flow of 0.5 µl per hour for up to 7 days) filled with 100 µl of CNO solution (1 mg/ml in saline solution, Sigma) was then placed through the incision to rest comfortably on the mouse's back. No impairment of normal behavior as a result of discomfort from the implant could be observed in the days following the procedure. CNO delivery was protracted over the course of several days during maturation, with a steady flow of 0.5 µl per hour according to the manufacturer's specification (Alzet). In a subset of P14-implanted animals (14 subjects), the minipump was surgically removed at P20 through a second incision. Seven subjects were perfused after 3 days of recovery (P23), while another 7 were perfused after 6 days of recovery (P26) and processed for further analysis.

LEGENDS

Fig. 1: Stagewise sequential maturation of the entorhinal-hippocampal network.

(**A**) Schematic representation of information flow in the transverse entorhinal-hippocampal circuit (*49-53*). (**B**) Validation of DCX+ quantification in adult mice (P90-P120), > 1500 cells from 3 mice. (**C**) Fraction of neurons with DCX expression levels below the detection limit in each local network during successive days of maturation (DCX–, cumulative distributions, mean ± S.D., > 120000 neurons from 3 mice for each time point). (**D**) Hierarchical clustering of data in (C); *x* axis: length of the links of the dendrogram, arbitrary units. MEC-L2 St is the first population to exhibit dissimilarity from the rest of the network, followed by (i) MEC-L2 Pyr and CA3, (ii) CA1, (iii) DG, SUB, MEC-L5 and LEC-L5, and (iv) LEC-L2. (**E**) Fraction of cells in each local network exhibiting PV expression (PV+) at successive stages of maturation. Cumulative distributions are normalized to adult levels of PV+ neurons in each local network. Mean ± S.D., > 45000 neurons from 3 mice. (**F**) Density of synaptic puncta in each local neuropil volume normalized to adult levels for each area. Synaptic puncta are identified by the expression of the protein Bassoon (Bs+). Adult levels are quantified at P90 as number of puncta / neuropil μm^3, mean ± S.D. (9 independent areas from 3 mice for each time point).

Fig. 2: Excitatory activity in MEC-L2 provides an instructive signal for maturation across stages of the entorhinal-hippocampal circuit.

(**A**) Local fraction of DCX– neurons (mean ± S.D.) in control animals (black bars) and CNO animals upon MEC-L2 silencing (red bars). *x* axis: region of the entorhinal-hippocampal network.

y axis: fraction of NeuN+ cells with DCX levels below the detection limit; > 24000 cells from at least 3 animals per group. Three categorically different classes of treatments were pooled to form the control group: (i) No virus, No CNO; (ii) Virus, No CNO; (iii) No Virus, CNO. (**B**) DCX expression upon hippocampus-specific silencing. > 24000 cells from at least 3 animals per group, controls pooled across 3 categorically different classes of treatment, as in (A). (**C**) DCX expression upon LEC-specific silencing. > 24000 cells from at least 3 animals per group; controls pooled as above.

Fig. 3: Dorso-ventral topographical maturation of MEC is driven by excitatory activity in L2.

(**A**) The fraction of DCX– neurons was determined at eight positions of equal dimension (each 375 μm in length) along the dorso-ventral axis of MEC (Positions I-VIII) in a single sagittal section (NeuN+ cells, red). Dorsal and ventral borders of MEC were identified as sharp transitions in L2 cell density (position 0 corresponding to the MEC-postrhinal cortex transition (MEC-POR); position 3000 corresponding to MEC-LEC transition). The length of segment VIII was adjusted for early postnatal sections (P8-P14) to account for change in brain size (therefore, the MEC-to-LEC transition always fell into this block). The total number of NeuN+ cells in each block did not change significantly between P5 and P90 (except for block VIII). (**B**) Cumulative fractions of DCX– neurons in superficial and deep layers in every segment along the dorso-ventral MEC axis. Stellate and pyramidal cells were distinguished based on reelin and calbindin expression. > 45000 neurons from 3 animals per time point. (**C**) Fraction of DCX– excitatory neurons and PV+ inhibitory neurons after silencing excitatory neurons selectively in MEC-L2 (green) or widely across retrohippocampal cortices (orange) between P14 and P20. Controls were pooled as in Fig. 2. > 210000 neurons from at least 3 animals per treatment group. (**D**) Similar estimates of DCX

and PV expression after silencing excitatory neurons in MEC-L2 (green) or retrohippocampal cortices (orange) between P11 and P14. > 60000 neurons from at least 3 animals per treatment group.

Fig. 4: Topographic distribution of stellate cells reflects progression of neurogenesis.

(**A**) Expression of BrdU (yellow) in the adult MEC-L2 network as a result of BrdU injection in the pregnant mother (40× single confocal plane image from a sagittal section 3.5 mm lateral to the midline, reelin in magenta and calbindin in cyan; yellow arrows indicate stellate and pyramidal cells that are positive for BrdU). Anatomical mapping of isochronic cohorts of cells was performed at eight positions from the MEC-POR border; see Fig. 3A. Dorso-ventral segments are color-coded. (**B**) Fraction of BrdU+ stellate cells (upper panel) and pyramidal cells (lower panel) across embryonic days and segments along the dorso-ventral MEC axis. In each segment, we counted the number of neurons positive for either reelin (Rl+, stellate cells) or calbindin (Cb+, pyramidal cells), and analyzed the proportions of these that stained for BrdU in the nucleus (mean ± S.D.; > 450000 neurons from at least 3 mice per time point). (**C**) Cumulative probability distributions showing the same data as in (B). Injection of BrdU at E10 and E17 did not produce any detectable staining in the adult, thereby marking the beginning and the end, respectively, of the MEC neurogenesis window. (**D**) DCX expression in stellate and pyramidal neurons born on the same day at different dorso-ventral positions along the MEC (> 20000 neurons from at least 3 mice per time point). BrdU was injected at E13 and only stellate and pyramidal cells labelled by BrdU were considered for the analysis. The fraction of DCX negative BrdU-labelled cells was determined at three time points during network maturation (P11, P14 and P17, colour-coded).

Fig. 5: Excitatory activity from stellate cells drives network maturation.

(**A**) Schematic illustrating the experiment. **(B**) Molecular identity of infected neurons as a function of the embryonic day of viral injection. *y* axis: fraction of mCherry+ cells that coexpress a marker for stellate cells (reelin) or pyramidal cells (calbindin) (> 54000 neurons from at least 3 animals per timepoint). (**C**) Fraction of DCX– cells in different regions of the entorhinal-hippocampal network upon silencing of isochronic cohorts dominated by stellate cells in MEC-L2 (E12-born; mean ± S.D.). The fraction of neurons showing downregulated DCX expression after silencing is different from control animals in all cell types and areas, with the exception of MEC-L2 St and LEC-L2. The lack of effect on LEC-L2 is likely due to the immaturity of this local network at P17; note low value in control animals. All comparisons with Student's t-test were significant ($t > 7.44$ and $P < 0.01$), with the exception of LEC-L2 ($t = 0.36$ and $P = 0.70$). Analyses were conducted in the dorsal entorhinal cortex and hippocampus; > 27000 neurons from at least 3 mice per experimental group. 3 categorically different classes of treatment were pooled to form the control group, as in Fig. 2. (**D**) Fraction of DCX– cells upon silencing of isochronic cohorts dominated by pyramidal neurons (E16-born; mean ± S.D.). DCX expression in silenced animals is indistinguishable from that of controls ($t < 1.03$ and $P > 0.34$). Similar effects were obtained with other silencing windows (Fig. S11 and S12). Analysis conducted with similar control groups and a similar number of neurons and animals as in (B).

Fig. 6: Isochronic cohorts of neurons act synergistically to drive MEC-L2 maturation. Quantitative analysis of network maturation based on DCX expression along the dorso-ventral axis of MEC-L2. DCX– pyramidal cells and PV+ interneurons disappear when an isochronic population of E12-born neurons is silenced (green), but not when the ligand targets a comparable fraction of randomly labelled L2 cells (orange, "Random cells – entire network": 20% of MEC-L2 excitatory neurons labelled) or stellate cells (blue, "Random cells – stellate cells": 20% of MEC-L2 stellate

cells labelled). Data are based on > 45000 neurons from 3 animals per group. 3 categorically different classes of treatment were pooled to form the control group, as in Fig. 2.

Fig. 1

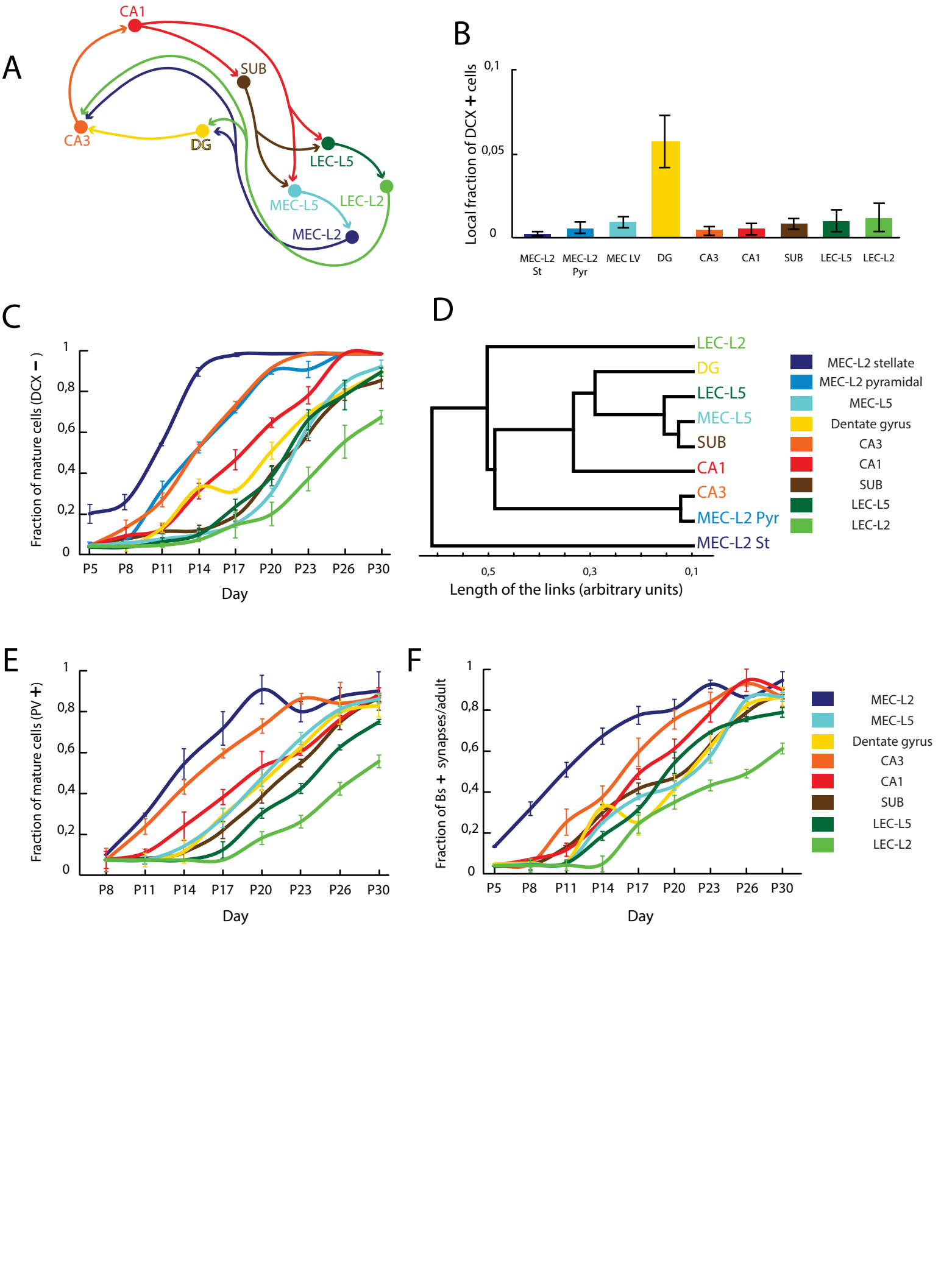
A
CA1
SUB
CA3
DG
LEC-L5
MEC-L5
LEC-L2
MEC-L2
B
Local fraction of DCX + cells
0,1
0,05
0
MEC-L2 St
MEC-L2 Pyr
MEC LV
DG
CA3
CA1
SUB
LEC-L5
LEC-L2
C
Fraction of mature cells (DCX +)
1
0,8
0,6
0,4
0,2
0
P5
P8
P11
P14
P17
P20
P23
P26
P30
Day
D
LEC-L2
DG
LEC-L5
MEC-L5
SUB
CA1
CA3
MEC-L2 Pyr
MEC-L2 St
0,5
0,3
0,1
Length of the links (arbitrary units)
MEC-L2 stellate
MEC-L2 pyramidal
MEC-L5
Dentate gyrus
CA3
CA1
SUB
LEC-L5
LEC-L2
E
Fraction of mature cells (PV +)
1
0,8
0,6
0,4
0,2
0
P8
P11
P14
P17
P20
P23
P26
P30
Day
F
Fraction of Bs + synapses/adult
1
0,8
0,6
0,4
0,2
0
P5
P8
P11
P14
P17
P20
P23
P26
P30
Day
MEC-L2
MEC-L5
Dentate gyrus
CA3
CA1
SUB
LEC-L5
LEC-L2

Fig. 2

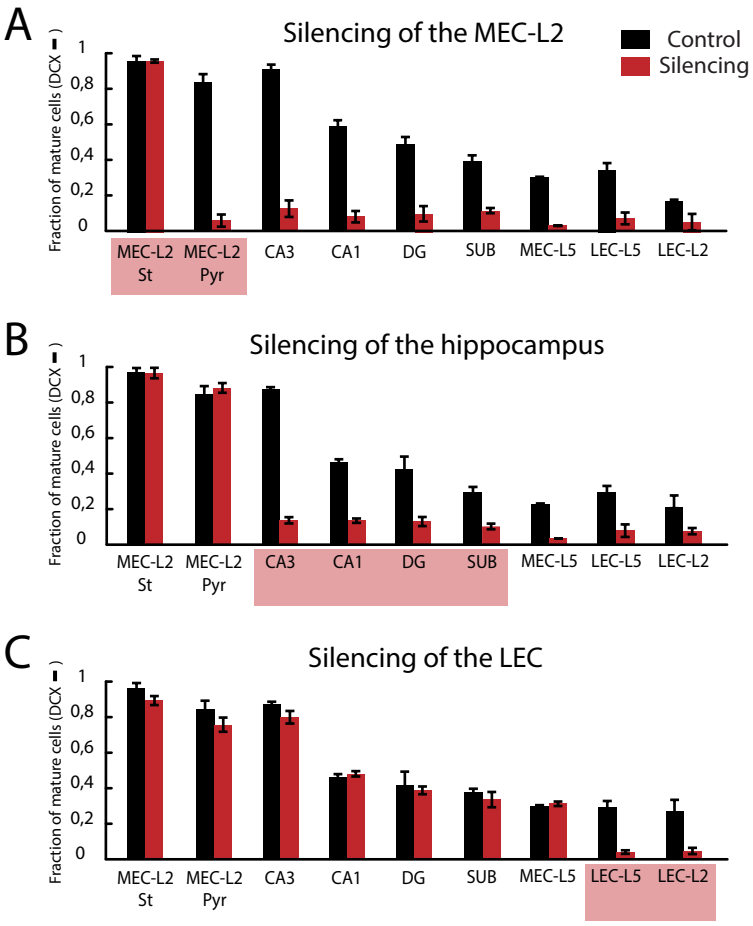
A
Silencing of the MEC-L2
Control
Silencing
Fraction of mature cells (DCX +)
1
0,8
0,6
0,4
0,2
0
MEC-L2 St
MEC-L2 Pyr
CA3
CA1
DG
SUB
MEC-L5
LEC-L5
LEC-L2
B
Silencing of the hippocampus
Fraction of mature cells (DCX +)
MEC-L2 St
MEC-L2 Pyr
CA3
CA1
DG
SUB
MEC-L5
LEC-L5
LEC-L2
C
Silencing of the LEC
Fraction of mature cells (DCX +)
MEC-L2 St
MEC-L2 Pyr
CA3
CA1
DG
SUB
MEC-L5
LEC-L5
LEC-L2

Fig. 3

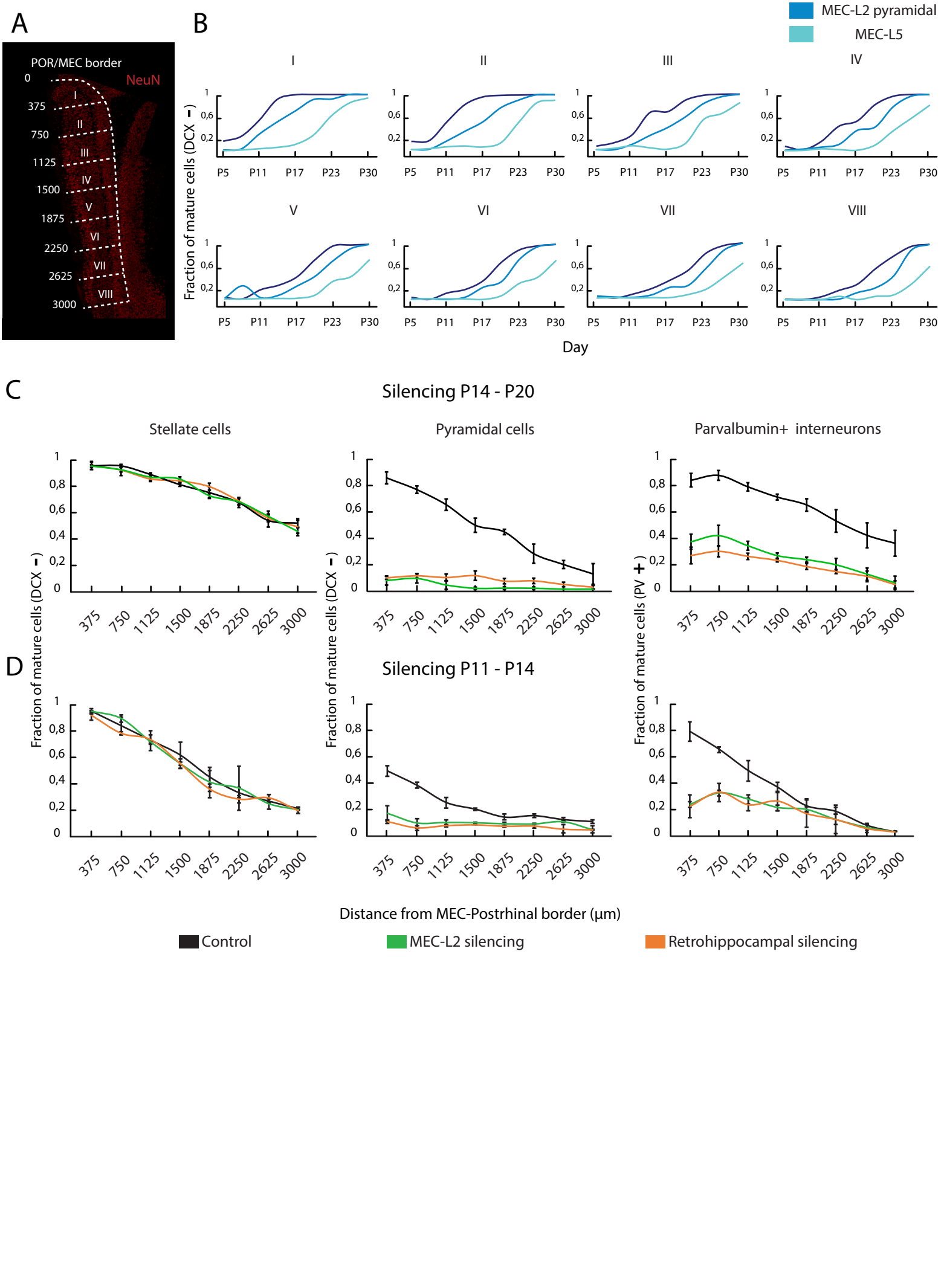
A
POR/MEC border
NeuN
0
375
750
1125
1500
1875
2250
2625
3000
I
II
III
IV
V
VI
VII
VIII
B
MEC-L2 stellate
MEC-L2 pyramidal
MEC-L5
Fraction of mature cells (DCX +)
P5
P11
P17
P23
P30
Day
C
Silencing P14 - P20
Stellate cells
Pyramidal cells
Parvalbumin+ interneurons
Fraction of mature cells (DCX +)
Fraction of mature cells (PV +)
D
Silencing P11 - P14
Distance from MEC-Postrhinal border (µm)
Control
MEC-L2 silencing
Retrohippocampal silencing

Fig. 4

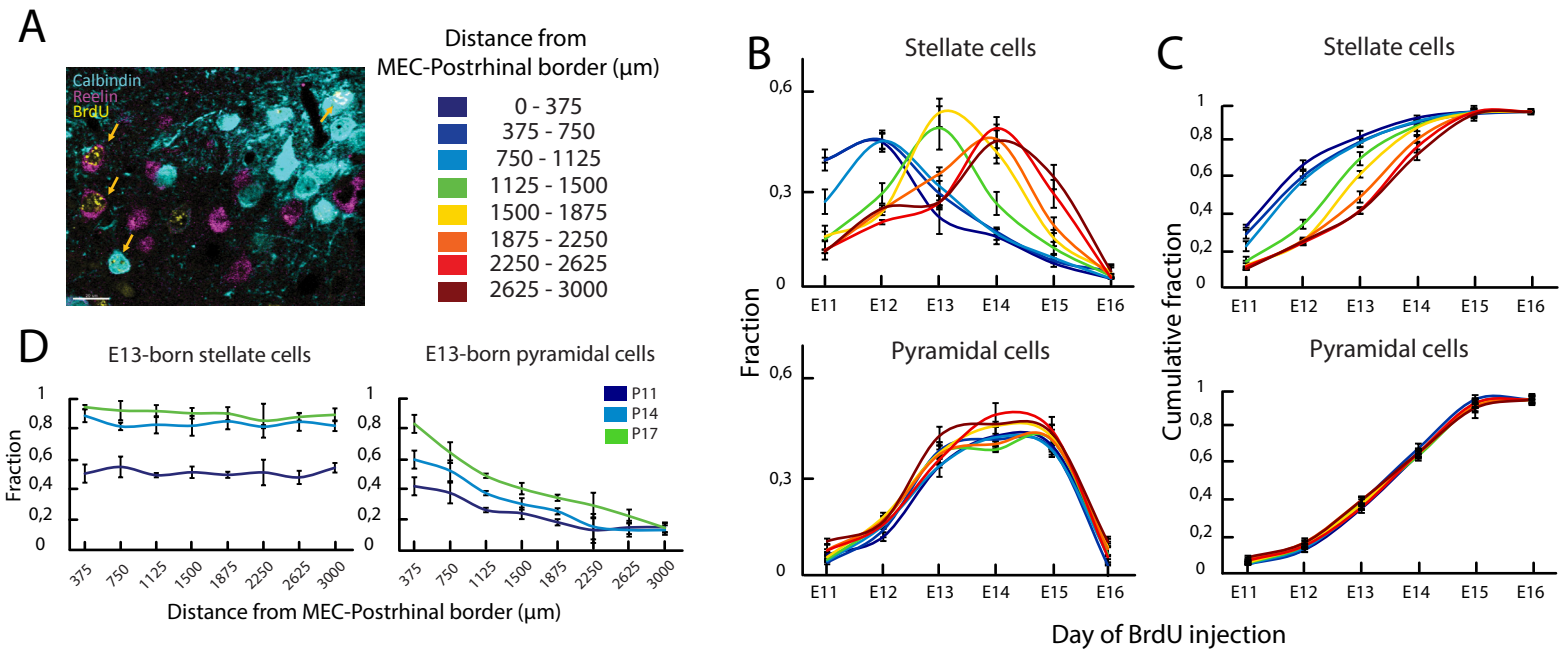
A
Calbindin
Reelin
BrdU
Distance from
MEC-Postrhinal border (µm)
0 - 375
375 - 750
750 - 1125
1125 - 1500
1500 - 1875
1875 - 2250
2250 - 2625
2625 - 3000
B
Stellate cells
Pyramidal cells
Fraction
E11
E12
E13
E14
E15
E16
C
Stellate cells
Pyramidal cells
Cumulative fraction
Day of BrdU injection
D
E13-born stellate cells
E13-born pyramidal cells
P11
P14
P17
Fraction
Distance from MEC-Postrhinal border (µm)

Fig. 5

A

Experiment timeline:

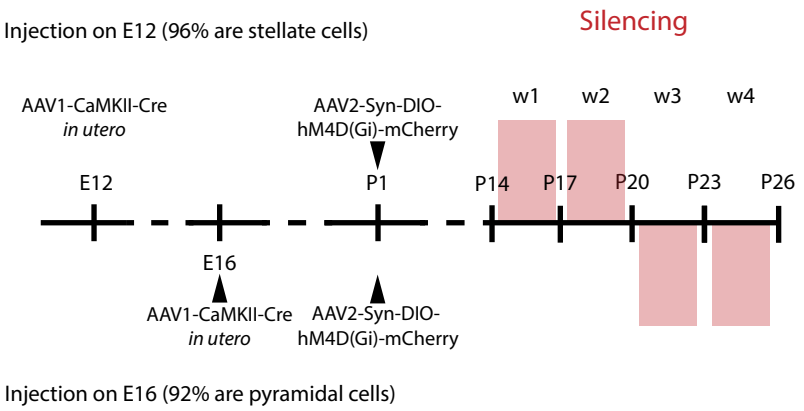

B

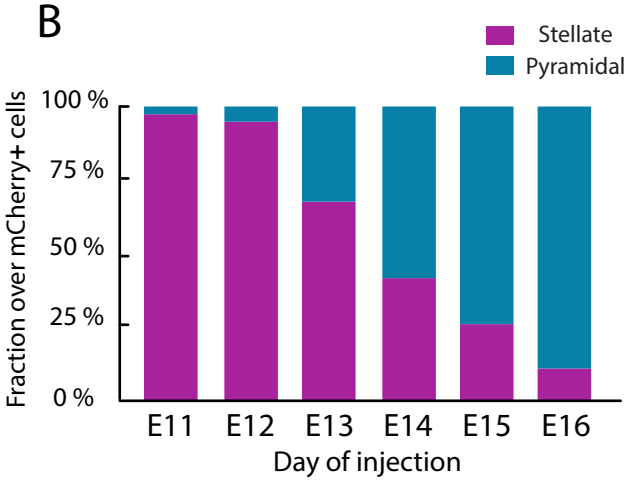

C

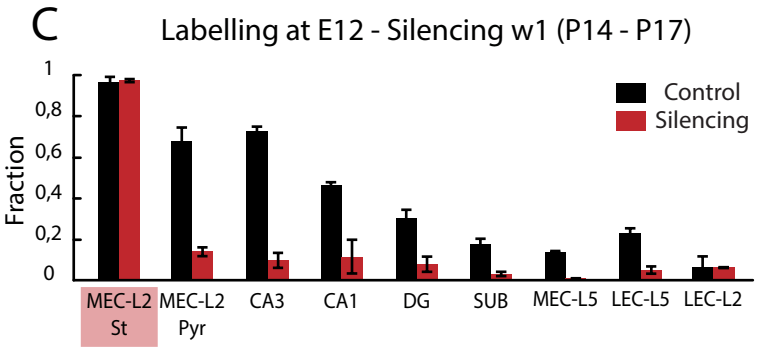

D

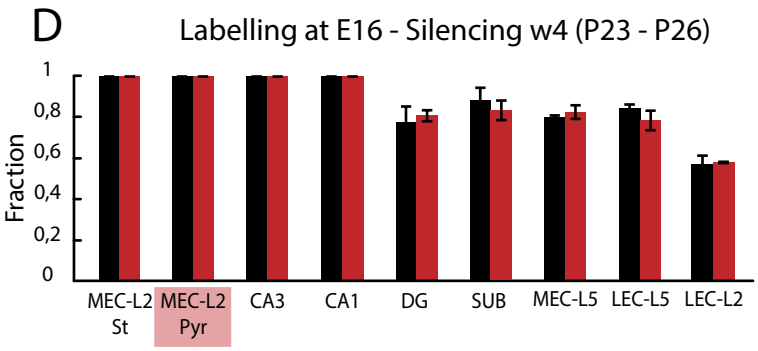

Fig. 6

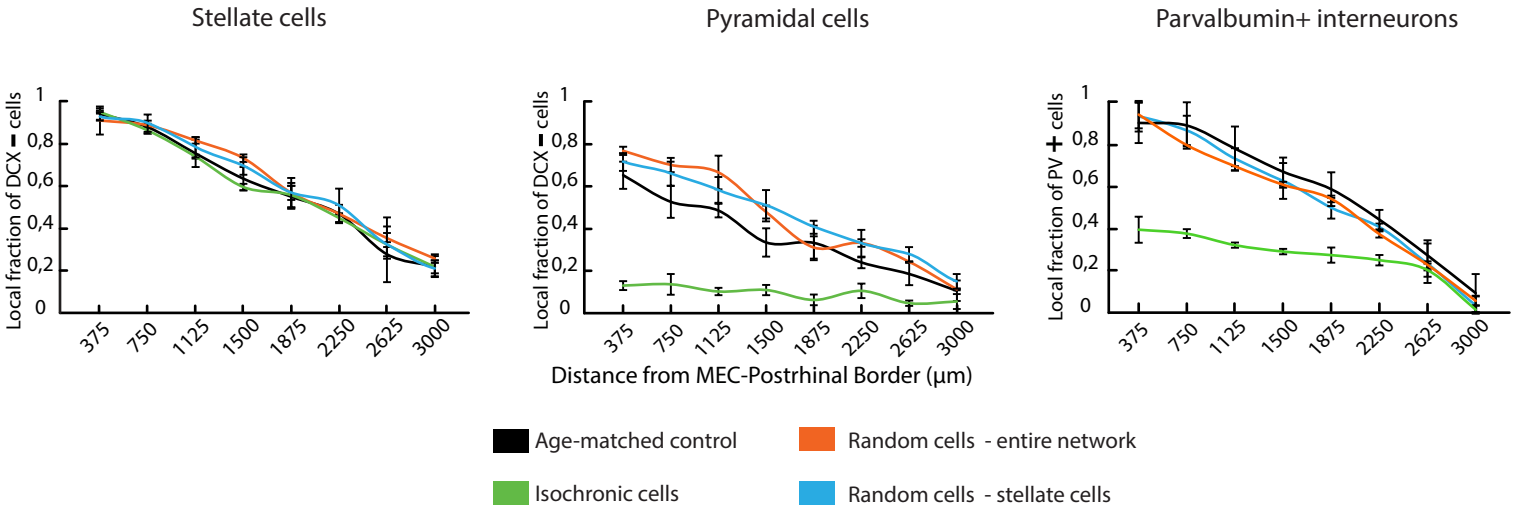
Stellate cells
Pyramidal cells
Parvalbumin+ interneurons
Local fraction of DCX - cells
Local fraction of DCX - cells
Local fraction of PV + cells
1
0,8
0,6
0,4
0,2
0
375
750
1125
1500
1875
2250
2625
3000
Distance from MEC-Postrhinal Border (µm)
Age-matched control
Random cells - entire network
Isochronic cells
Random cells - stellate cells

References:

1. W. P. E. Boldrey, Somatic motor and sensory representation in the cerebral cortex of man as studied by electrical stimulation. *Brain* **lx**, 389 (Dec 1937, 1937).

2. V. B. Mountcastle, Modality and topographic properties of single neurons of cat's somatic sensory cortex. *Journal of neurophysiology* **20**, 408 (Jul, 1957).

3. D. H. Hubel, T. N. Wiesel, Receptive fields, binocular interaction and functional architecture in the cat's visual cortex. *The Journal of physiology* **160**, 106 (Jan, 1962).

4. A. D. Huberman, M. B. Feller, B. Chapman, Mechanisms underlying development of visual maps and receptive fields. *Annual review of neuroscience* **31**, 479 (2008).

5. T. N. Wiesel, D. H. Hubel, Effects of Visual Deprivation on Morphology and Physiology of Cells in the Cats Lateral Geniculate Body. *Journal of neurophysiology* **26**, 978 (Nov, 1963).

6. D. H. Hubel, T. N. Wiesel, Receptive Fields of Cells in Striate Cortex of Very Young, Visually Inexperienced Kittens. *Journal of neurophysiology* **26**, 994 (Nov, 1963).

7. L. Galli, L. Maffei, Spontaneous impulse activity of rat retinal ganglion cells in prenatal life. *Science* **242**, 90 (Oct 7, 1988).

8. L. C. Katz, C. J. Shatz, Synaptic activity and the construction of cortical circuits. *Science* **274**, 1133 (Nov 15, 1996).

9. D. C. Rowland, Y. Roudi, M. B. Moser, E. I. Moser, Ten Years of Grid Cells. *Annual review of neuroscience* **39**, 19 (Jul 8, 2016).

10. E. I. Moser *et al.*, Grid cells and cortical representation. *Nature reviews. Neuroscience* **15**, 466 (Jul, 2014).

11. R. y. Cajal, Estructura del asta de Ammon y fascia dentata. *Charles Thomas*, (1893, 1893).

12. L. d. Nó, Studies on the structure of the cerebral cortex. *Journal of Psychology and Neurology* **45**, (1933).

13. M. P. Witter, E. I. Moser, Spatial representation and the architecture of the entorhinal cortex. *Trends in neurosciences* **29**, 671 (Dec, 2006).

14. N. Cappaert, N. Van Strien, M. Witter, *Hippocampal Formation*. The rat nervous system (2015), pp. 511-573.

15. R. F. Langston *et al.*, Development of the spatial representation system in the rat. *Science* **328**, 1576 (Jun 18, 2010).

16. T. J. Wills, F. Cacucci, N. Burgess, J. O'Keefe, Development of the hippocampal cognitive map in preweanling rats. *Science* **328**, 1573 (Jun 18, 2010).

17. T. L. Bjerknes, E. I. Moser, M. B. Moser, Representation of geometric borders in the developing rat. *Neuron* **82**, 71 (Apr 2, 2014).

18. T. L. Bjerknes, R. F. Langston, I. U. Kruge, E. I. Moser, M. B. Moser, Coherence among head direction cells before eye opening in rat pups. *Current biology : CB* **25**, 103 (Jan 5, 2015).

19. L. Muessig, J. Hauser, T. J. Wills, F. Cacucci, A Developmental Switch in Place Cell Accuracy Coincides with Grid Cell Maturation. *Neuron* **86**, 1167 (Jun 3, 2015).

20. J. G. Gleeson, P. T. Lin, L. A. Flanagan, C. A. Walsh, Doublecortin is a microtubule-associated protein and is expressed widely by migrating neurons. *Neuron* **23**, 257 (Jun, 1999).

21. J. Nacher, C. Crespo, B. S. McEwen, Doublecortin expression in the adult rat telencephalon. *The European journal of neuroscience* **14**, 629 (Aug, 2001).

22. H. van Praag, G. Kempermann, F. H. Gage, Running increases cell proliferation and neurogenesis in the adult mouse dentate gyrus. *Nature neuroscience* **2**, 266 (Mar, 1999).

23. D. Doischer *et al.*, Postnatal differentiation of basket cells from slow to fast signaling devices. *The Journal of neuroscience : the official journal of the Society for Neuroscience* **28**, 12956 (Nov 26, 2008).

24. S. tom Dieck *et al.*, Bassoon, a novel zinc-finger CAG/glutamine-repeat protein selectively localized at the active zone of presynaptic nerve terminals. *The Journal of cell biology* **142**, 499 (Jul 27, 1998).

25. J. B. Angevine, Jr., Time of neuron origin in the hippocampal region. An autoradiographic study in the mouse. *Experimental neurology. Supplement*, Suppl 2:1 (Oct, 1965).

26. Y. Deguchi, F. Donato, I. Galimberti, E. Cabuy, P. Caroni, Temporally matched subpopulations of selectively interconnected principal neurons in the hippocampus. *Nature neuroscience* **14**, 495 (Apr, 2011).

27. C. Miao *et al.*, Hippocampal Remapping after Partial Inactivation of the Medial Entorhinal Cortex. *Neuron* **88**, 590 (Nov 4, 2015).

28. S. Ray, M. Brecht, Structural development and dorsoventral maturation of the medial entorhinal cortex. *eLife* **5**, (2016).

29. L. Telley *et al.*, Sequential transcriptional waves direct the differentiation of newborn neurons in the mouse neocortex. *Science* **351**, 1443 (Mar 25, 2016).

30. J. B. Angevine, Jr., R. L. Sidman, Autoradiographic study of cell migration during histogenesis of cerebral cortex in the mouse. *Nature* **192**, 766 (Nov 25, 1961).

31. P. Rakic, Neurons in rhesus monkey visual cortex: systematic relation between time of origin and eventual disposition. *Science* **183**, 425 (Feb 1, 1974).

32. B. L. McNaughton, F. P. Battaglia, O. Jensen, E. I. Moser, M. B. Moser, Path integration and the neural basis of the 'cognitive map'. *Nature reviews. Neuroscience* **7**, 663 (Aug, 2006).

33. Y. Burak, I. R. Fiete, Accurate path integration in continuous attractor network models of grid cells. *PLoS computational biology* **5**, e1000291 (Feb, 2009).

34. J. J. Couey *et al.*, Recurrent inhibitory circuitry as a mechanism for grid formation. *Nature neuroscience* **16**, 318 (Mar, 2013).

35. M. C. Fuhs, D. S. Touretzky, A spin glass model of path integration in rat medial entorhinal cortex. *The Journal of neuroscience : the official journal of the Society for Neuroscience* **26**, 4266 (Apr 19, 2006).

36. T. Bonnevie et al., Grid cells require excitatory drive from the hippocampus. *Nature neuroscience* **16**, 309 (Mar, 2013).

37. P. Gao *et al.*, Deterministic progenitor behavior and unitary production of neurons in the neocortex. *Cell* **159**, 775 (Nov 6, 2014).

38. H. Stensola *et al.*, The entorhinal grid map is discretized. *Nature* **492**, 72 (Dec 6, 2012).

39. S. Druckmann *et al.*, Structured synaptic connectivity between hippocampal regions. *Neuron* **81**, 629 (Feb 5, 2014).

40. M. Meister, R. O. Wong, D. A. Baylor, C. J. Shatz, Synchronous bursts of action potentials in ganglion cells of the developing mammalian retina. *Science* **252**, 939 (May 17, 1991).

41. C. S. Goodman, C. J. Shatz, Developmental mechanisms that generate precise patterns of neuronal connectivity. *Cell* **72 Suppl**, 77 (Jan, 1993).

42. X. Leinekugel *et al.*, Correlated bursts of activity in the neonatal hippocampus in vivo. *Science* **296**, 2049 (Jun 14, 2002).

43. H. S. Burr, The effects of the removal of the nasal pits in Amblystoma embryos. *J. Exp Zool* **20**, (1916).

44. R. Levi-Montalcini, The development to the acoustico-vestibular centers in the chick embryo in the absence of the afferent root fibers and of descending fiber tracts. *The Journal of comparative neurology* **91**, 209 (Oct, 1949).

45. L. Dryer, P. P. Graziadei, Influence of the olfactory organ on brain development. *Perspectives on developmental neurobiology* **2**, 163 (1994).

46. P. Rakic, Specification of cerebral cortical areas. *Science* **241**, 170 (Jul 8, 1988).

47. G. Lopez-Bendito, Z. Molnar, Thalamocortical development: how are we going to get there? *Nature reviews. Neuroscience* **4**, 276 (Apr, 2003).

48. P. Franklin, *Paxinos and Franklin's the Mouse Brain in Stereotaxic Coordinates, 4th Edition*. (Elsevier, Academic Press, 2012).

49. P. Andersen, T. V. Bliss, K. K. Skrede, Lamellar organization of hippocampal pathways. *Experimental brain research* **13**, 222 (1971).

50. O. Steward, Topographic organization of the projections from the entorhinal area to the hippocampal formation of the rat. *The Journal of comparative neurology* **167**, 285 (Jun 1, 1976).

51. L. W. Swanson, W. M. Cowan, An autoradiographic study of the organization of the efferent connections of the hippocampal formation in the rat. *The Journal of comparative neurology* **172**, 49 (Mar 1, 1977).

52. M. F. Yeckel, T. W. Berger, Feedforward excitation of the hippocampus by afferents from the entorhinal cortex: redefinition of the role of the trisynaptic pathway. *Proceedings of the National Academy of Sciences of the United States of America* **87**, 5832 (Aug, 1990).

53. A. Hjorth-Simonsen, Hippocampal efferents to the ipsilateral entorhinal area: an experimental study in the rat. *The Journal of comparative neurology* **142**, 417 (Aug, 1971).

54. J. M. Wojtowicz, N. Kee, BrdU assay for neurogenesis in rodents. *Nature protocols* **1**, 1399 (2006).

55. F. Donato, S. B. Rompani, P. Caroni, Parvalbumin-expressing basket-cell network plasticity induced by experience regulates adult learning. *Nature* **504**, 272 (Dec 12, 2013).

56. C. Varga, S. Y. Lee, I. Soltesz, Target-selective GABAergic control of entorhinal cortex output. *Nature neuroscience* **13**, 822 (Jul, 2010).

Acknowledgments.

We thank A.M. Amundsgård, A. Burøy, V. Frolov, K. Haugen, E. Kråkvik, B. B. Løfaldli and H. Waade for technical assistance, Pico Caroni, Silvia Arber and Paolo Capelli for training on in utero injections, Clifford Kentros and Rajeevkumaar Raveendran for viral reagents, and Menno Witter for discussion. The work was supported by two Advanced Investigator Grants from the European Research Council ('GRIDCODE', Grant Agreement N°338865; ENSEMBLE', Grant Agreement no. 268598), the Kavli Foundation, The Egil and Pauline Braathen and Fred Kavli Centre for Cortical Microcircuits, the Louis-Jeantet Prize for Medicine, the Centre of Excellence scheme of the Research Council of Norway (Centre for Neural Computation, Grant Agreement N°223262), and the EMBO long-term fellowship (ALTF 246-2013).

F.D., M.-B.M. and E.I.M. designed experiments and analyses; F.D. and R.I.J performed the experiments; F.D. performed the analyses; F.D. and E.I.M. wrote the paper with input from all authors.

Supplementary Materials for

Stellate cells drive maturation of the entorhinal-hippocampal circuit

Flavio Donato, R. Irene Jacobsen, May-Britt Moser and Edvard I. Moser

correspondence to: flavio.donato@ntnu.no and edvard.moser@ntnu.no

This PDF file includes:

Supplementary Materials and Methods

Figs. S1 to S14

Supplementary references *54-56*

Supplementary methods:

Virus injection in the adult.

On the day of surgery, adult mice (P60-P365) were anesthetized and analgesics were provided (Rymadil, Pfizer, intraperitoneal injection, 5 mg/kg; Temgesic, Schering-Plouch, local subcutaneous injection, 0.05 mg/kg; Marcain, AstraZeneca, subcutaneous injection, 1 mg/kg). A high titer of rAAV was injected into the target areas using a 5 µl Neuro Syringe (Hamilton Company, USA) with a 33-gauge metal needle. The virus carried a Cre-dependent construct for expression of the marker protein mCherry (AAV1-CAG-FLEX-mCherry, UPenn Vector Core, University of Pennsylvania). Injection volume (up to 200 nl at each location for a maximum amount of 500 nl) and flow rate (0.1 µl/min) were controlled with a Micro4 Microsyringe Pump Controller (World Precision Instruments). Two injection sites were used to target the MEC at a medial and a lateral location (*48*). The medial injection was performed at 3.4 mm lateral to bregma, 0.3 mm anterior to the transverse sinus, at 3 locations in depth (1.7, 1.5 and 1.3 mm from the dura surface). The lateral injection was performed at 4 mm lateral to bregma, 0.2 mm anterior to the transverse sinus, at 2 location in depth (1.5 and 1.3 mm from the dura surface). After the injection, the needle was kept in position for 10 minutes before retraction. Finally, the skin was sutured, and the animal allowed to recover in a heated chamber (38°C, 30-90 minutes) until it regained complete mobility and alertness.

Temporal specificity of in utero viral labelling.

To verify the temporal specificity of the viral labelling, we used a combined viral/BrdU approach. Ultrasound imaging was used to target the viral solution (AAV1-CaMKII-Cre) into the developing lateral ventricle at E13 as described in the main methods section. BrdU (5-Bromo-2′-deoxyuridine ≥99% (HPLC), Sigma-Aldrich, 100 mg/Kg) was injected intraperitoneally in the pregnant mother at different intervals from the embryonic AAV injections, which was defined as time 0 in our time course. A second injection, aimed at the MEC, was performed in adult animals (P60-P90) as described above, and carried a Cre-dependent construct to highlight the cells targeted in utero. For every time point of BrdU

injection, we quantified the fraction of cells labelled by the virus that also exhibited BrdU reactivity in the nucleus.

Histology, staining and confocal imaging.

Mice received an overdose of sodium pentobarbital before transcardial perfusion with freshly prepared PFA (4% in PBS, flow of 2 ml/min). Samples were sliced on a cryostat (30-50 µm thick sections) and stained for immunodetection of specific proteins. Briefly, floating sections were incubated overnight with the primary antibody diluted in a solution of PBS + 0.3% Triton + 3% BSA; washed 3 times with PBS + 0.3% Triton; incubated for 1h at room temperature with the secondary antibody diluted in a solution of PBS + 0.3% Triton + 3% BSA; washed with PBS 3 times and then mounted on a slide (ProLong Gold Antifade used as embedding medium, Invitrogen). Primary antibodies were as follows: Rabbit anti NeuN (1:1000, AbCam), Mouse anti NeuN (1:200, Millipore), Mouse anti Reelin (1:200, MBL International), Rabbit anti Calbindin (1:1000, Swant), Goat anti Parvalbumin (1:10000, Swant), Goat anti Doublecortin (1:200, Santa Cruz Biotechnology), Rabbit anti c-FOS (1:1000, Santa Cruz Biotechnology) Mouse anti Bassoon (1:200, RY), Rat anti BrdU (1:500, Abcam). Different antibody combinations were applied to the same sections during individual reactions, according to the proteins under study. Secondary antibodies were reactive to the species that hosted the production of the primary antibodies, and conjugated to Alexa fluorophore 488, 568 or 647 (1:500, Molecular Probes).

BrdU labeling in vivo was carried out at 24h intervals as previously described (*54*). Briefly, we injected mice with BrdU (5-Bromo-2′-deoxyuridine ≥99% (HPLC), Sigma-Aldrich; 100 mg/kg) at defined times during embryonic development, and analyzed brain sections of 3 month old mice for BrdU labeling. Only strongly BrdU-labeled cells that did not undergo further rounds of DNA replication and cell division subsequent to BrdU incorporation were included in the analysis.

For confocal imaging, an LSM 510 Meta and a Zeiss LSM 880 microscope (Carl Zeiss, Germany) were used. Samples belonging to the same experiment (samples from experimental mice at a given time point, with their controls) were acquired in parallel and with the same

settings (laser power: 2-15%; optical slice: 1.28–1.35 airy units, step size: 2 µm for population analysis; 0.5 µm for synaptic analysis) using an EC Plan-Neofluar 20×/0.8 air immersion, 40×/1.3 oil immersion, and 63×/1.4 oil immersion objective (Zeiss). Before acquisition, gain and digital offset were established on sections from control animals to optimize the dynamic range of acquisition to the dynamic range of the staining (baselines were set independently for every staining based on the protein under investigation, see the following paragraphs). Pixel size was optimized for synaptic detection (200 nm axial resolution). Settings were kept constant during acquisition.

Automatic identification of BrdU, NeuN, Doublecortin, Reelin, Calbindin, Parvalbumin or c-FOS expressing cells was performed with commercially available software (ImageJ; Imaris, Bitplane). For the analysis of Doublecortin (DCX) expression, cells were first identified by the expression of the neuronal marker NeuN (NeuN+), Reelin (Rl+) or Calbindin (Cb+). Then the average intensity values of pixels in the somas of identified cells were compared to a baseline threshold to determine the level of DCX fluorescence. The threshold was set to the average level of fluorescence of pixels located in the nucleus of excitatory cells (DCX is excluded from the nuclear compartment, which hence constitutes an ideal baseline for evaluating expression, (*20*)). Neurons were considered as Doublecortin negative (DCX–) when the intensity of fluorescence of DCX in the soma fell below the threshold value. We limited analysis to the internal portion of the soma by excluding the subcortical portion of the cell (about 3 µm below the cell membrane) from further analysis, to avoid bleed-through of extracellular signal into the cell under study. DCX downregulation was expressed as the fraction of NeuN+ neurons with undetectable levels of DCX at the specific anatomical location under investigation (see below), giving a range from 0 (all NeuN+ cells are DCX+) to 1 (all NeuN+ are DCX–).

For the analysis of maturation in the fast-spiking interneuron network, parvalbumin (PV) expressing somas were detected using an immunological marker. Cells were considered positive when the expression of PV exceeded the noise level set at the intensity value of the extracellular matrix. The number of PV+ cells was subsequently normalized to the number of positive neurons detected in adult animals (P90-P120) in a comparable volume of tissue. We did not distinguish between high and low-expressing PV interneurons, because the difference

between these two subtypes of interneurons, linked to different regulations of plasticity in adult cortical circuits, is not expressed until approximately P60 in the mouse (*55*).

For the analysis of c-FOS expression, cells were first identified by expression of the neuronal marker NeuN (NeuN+). Then the average intensity values of pixels in the soma of identified cells were compared to a baseline threshold to determine the level of c-FOS fluorescence. The threshold was set to the average level of fluorescence of pixels located in the extracellular matrix (defined as the portion of the neuropil devoid of NeuN signal). We then quantified the fraction of the NeuN+ neurons with c-FOS expression at the specific anatomical location under investigation (see below), giving a range from 0 (all NeuN+ cells are c-FOS-) to 1 (all NeuN+ are c-FOS+).

For the analysis of synaptogenesis, Bassoon expressing puncta (Bs+) were automatically identified with commercially available software (ImageJ; Imaris, Bitplane). Baseline was set at pixel intensity values found in the nucleus. The number of Bs puncta was then normalized to the number of puncta detected in adult animals (P60-P120) in a comparable volume of neuropil (neuropil volume was calculated by subtracting the volume occupied by cell somas and neuronal processes, identified by NeuN+ signal, from the total volume under investigation). We analyzed nine independent field of views from each region in the network. The nine areas were chosen to minimize the volume occupied by blood vessels, which were excluded from the analysis.

For analysis of neurogenesis, BrdU injections were performed on each consecutive day between E10 and E17 (the dam of each litter was injected once). Injections at E10 and E17 did not label any cells in the adult, thereby marking the beginning and end of MEC-L2 neurogenesis. Reelin+ (Rl), calbindin+ (Cb) and parvalbumin+ (PV) cells were considered BrdU+ if the nucleus exhibited non-zero levels of fluorescence for BrdU (baseline set at the pixel intensity value found in the soma). BrdU labelling was expressed as the fraction of the Rl/Cb/PV expressing neurons with nuclear labelling for BrdU.

Due to the topographic organization of the entorhinal-hippocampal network, we focused our analysis on the dorsal portion of the entorhinal cortex and hippocampus (EC: up to 500 μm from the border to postrhinal cortex, 3.5mm lateral to the midline). Local network analysis in the MEC network was conducted at discrete positions long the dorsoventral axis by subdividing the longitudinal extent of the MEC into eight blocks of equal dimension (each 375 μm in length). The dorsal and ventral borders of the MEC were identified by using as references the sharp transition in layer 2 cell density at each end (position 0 in Fig 3A corresponding to MEC to postrhinal cortex transition; position 3000 corresponding to MEC to LEC transition at the medio-lateral level of the CNS where the analysis was conducted, 3.2-3.6 mm lateral to the midline).

Statistical analysis.

Statistical analysis was conducted with commercially available software; Prism 6.0 (Graphpad) and Matlab (Mathworks). P values considered significant were <0.05. All comparisons performed were between sets of independent measures (measurements were performed on different sets of animals, without any repeated measure from an individual subject).

To assess statistical significance of developmental time courses and neurogenesis time courses, we used a 2-way ANOVA. Group and Segment were defined as factors for comparisons of local networks along the dorso-ventral MEC. In the developmental time course experiments, we first performed a global analysis between datasets collected at every time point for each of the three variables under investigation (fraction of DCX– stellate cells, fraction of DCX– pyramidal cells and fraction of adult interneurons expressing PV). In the silencing experiments, we subsequently performed pairwise comparisons for each of the three variables under investigation. Independent analysis was also conducted between each silenced group and its controls. In the neurogenesis analyses, we first performed a global analysis between datasets collected at every segment along the dorso-ventral axis of the MEC for each of the three variables under investigation (individual analysis for the fraction of DCX– stellate cells, fraction of DCX– pyramidal cells and fraction of the adult interneurons expressing PV); then a pairwise analysis was conducted for every possible combination among time points across individual segments. To assess statistical significance between control and silenced animals, we used the Student's t-test and the Mann-Whitney-Wilcoxon test.

To investigate similarities in the maturation time courses across nodes of the entorhinal-hippocampal network, we conducted an unbiased clustering analysis. Hierarchical clustering was performed to obtain two types of information: the equivalence between nodes of the dendrograms to define structures with comparable time courses of maturation, and the hierarchy of nodes to establish the temporal sequence of the process under investigation. For the hierarchical clustering in Fig. 1D, we used the Machine Learning Toolbox and Statistic Toolbox in Matlab (Mathworks). The length of the links (horizontal bars) in the dendrograms represents the similarity between the connected nodes. The null hypothesis of the analysis is that all the structures exhibit comparable maturation profiles.

Fig. S1

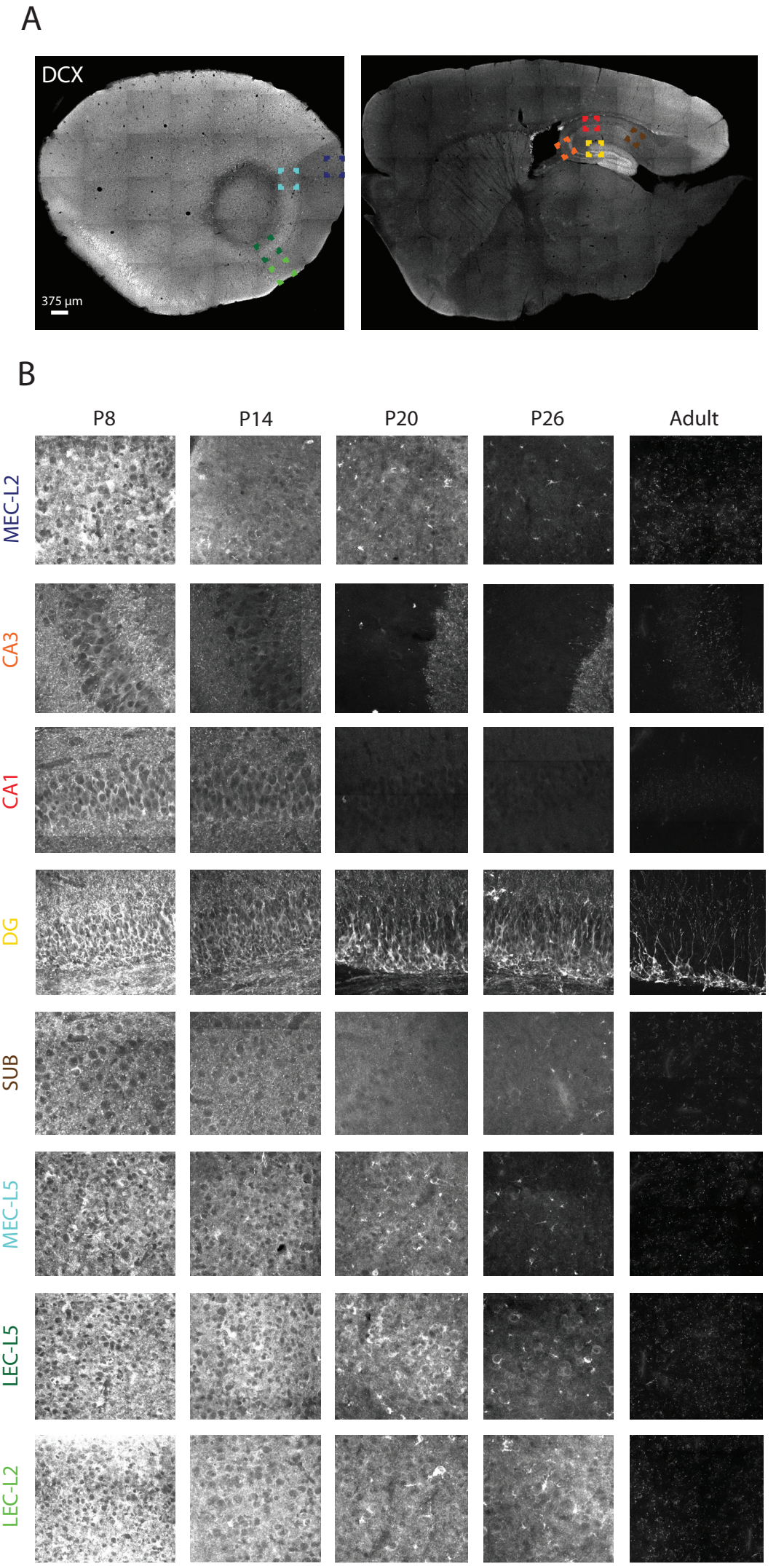
A
DCX
375 µm
B
P8
P14
P20
P26
Adult
MEC-L2
CA3
CA1
DG
SUB
MEC-L5
LEC-L5
LEC-L2

Fig. S1(Continued)

C

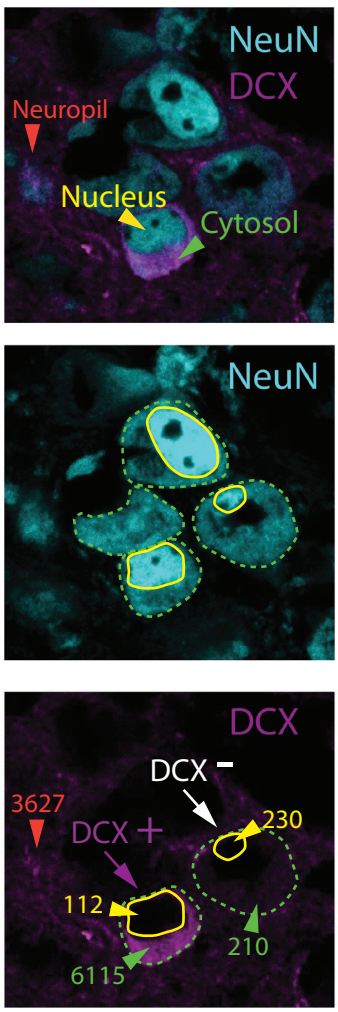

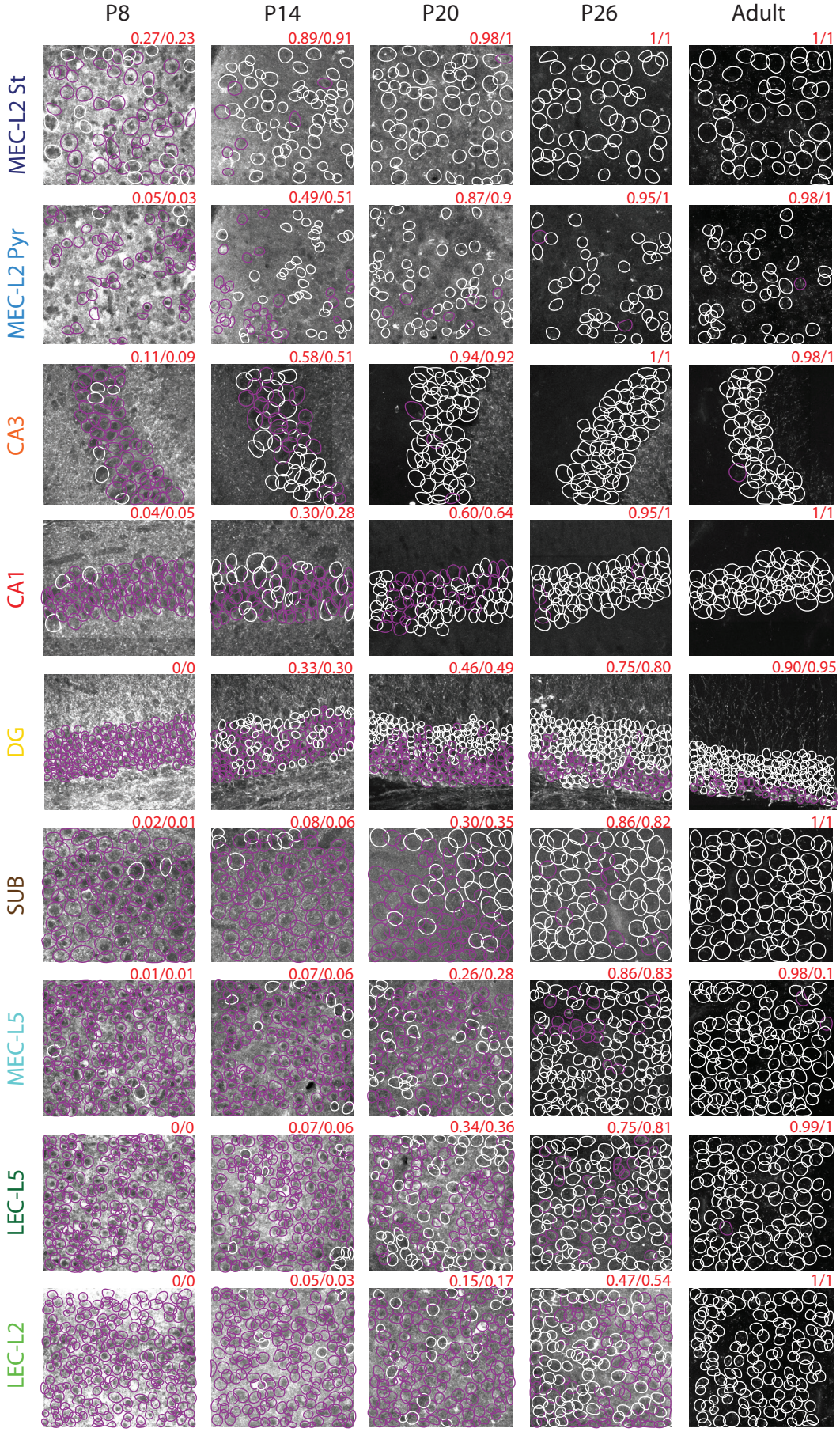

D

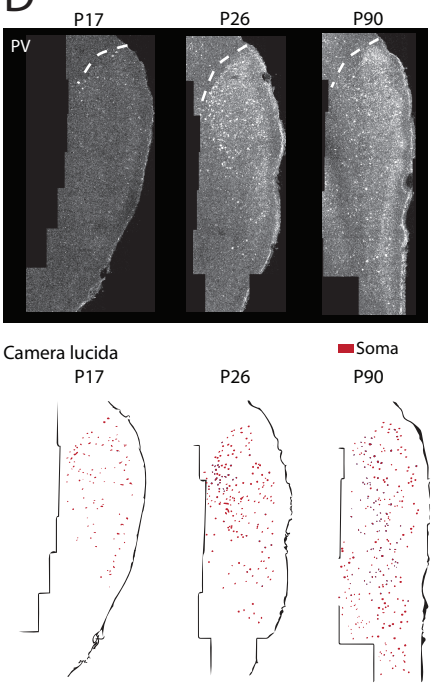

Fig. S1 Change in doublecortin expression across the entorhinal-hippocampal network during postnatal development.

(**A**) 10× confocal images with color-coded boxes showing the location of high-magnification images in (B). Sections are sagittal and show two different medio-lateral levels (through dorsal entorhinal cortex and hippocampus, respectively). Doublecortin (DCX) in white. (**B**) Confocal images showing DCX (white) across subregions of the entorhinal-hippocampal circuit at multiple time points during the first postnatal month (image locations as indicated in A). Validation of the quantification came from comparisons with adult expression levels (right panels; note exclusive expression in the dentate gyrus). Single fields of view were acquired with a 40×/1.3NA oil immersion objective (zoom 0.6×), and processed together, using constant parameters. Maximum intensity projections from 3D stacks recapitulate the quantification of DCX- cells presented in Fig. 1C. In CA3 panels, note high level of DCX immunoreactivity to the right, which reflects mossy fiber inputs from immature granule cells. (**C**) Left panels: 40× single confocal plane image of a cluster of 4 principal cells in MEC-L2 (NeuN+, cyan; Doublecortin, DCX, Magenta). Cytosolic signal (green arrows) and nuclear signal (yellow arrows) were distinguished from neuropil signal (orange arrows) by the expression of the neuronal marker NeuN (NeuN+) and either Reelin (Rl+) or Calbindin (Cb+) (NeuN staining is shown in the upper and middle panels). The average intensity values of pixels representing Doublecortin signal (DCX) were compared across identified cellular compartments (bottom panel, arbitrary units). In single cells, if the cytosolic signal exceeded the nuclear signal, the cell was considered to be DCX+ (cell identified by magenta arrow in lower panel; DCX is not present in the nuclear compartment, which hence constitutes an ideal baseline for evaluating expression (*20*)). Neurons were considered DCX negative (DCX–) when the intensity of fluorescence of DCX in the cytosol fell below the value for the nucleus (cell identified by white arrow in the lower panel). Neuropil signals were often as bright as cytosolic signals (Fig. S1B), and hence might contribute substantially to the fluorescence in cortical areas, but in the present analysis the neuropil signal was excluded from consideration. Right panels: processed dataset from (B). Individual neurons (identified automatically based on the expression of somatic markers, as in the left panels) have been labelled as regions of interest (ROI), and each individual ROI has been hand-drawn onto the maximum intensity projection of the DCX signal across the 3D dataset. Single ROIs (solid circles) are colour coded based on presence (magenta) or absence (white) of DCX, following the procedure in the left panels. Note that the overall

level of fluorescence present in specific regions of an image (hippocampus), or diffused through the whole extent of the cell layer (cortex), can be the result of neuropil contamination, which has been excluded from our single-cell analysis as previously explained. Above each image, its proportion of DCX- cells , compared to the mean value across animals (left and right side of slash, respectively; means as in Fig. 1C) is indicated. (**D**) Automatic quantification and analysis of parvalbumin-expressing neurons (PV+). Automatically detected somas of PV+ neurons (for detailed procedure, see Methods) were mapped along the dorso-ventral extent of the MEC to achieve local density estimates. Upper panels: 40× confocal images of sagittal sections from 3 different time points during postnatal development. Immunodetection was used to reveal PV expression (white) in the soma and neuropil processes of interneurons. Images are maximum intensity projections. Lower panels: camera lucida of upper panels. Each red dot is a PV+ soma.

Fig. S2

A

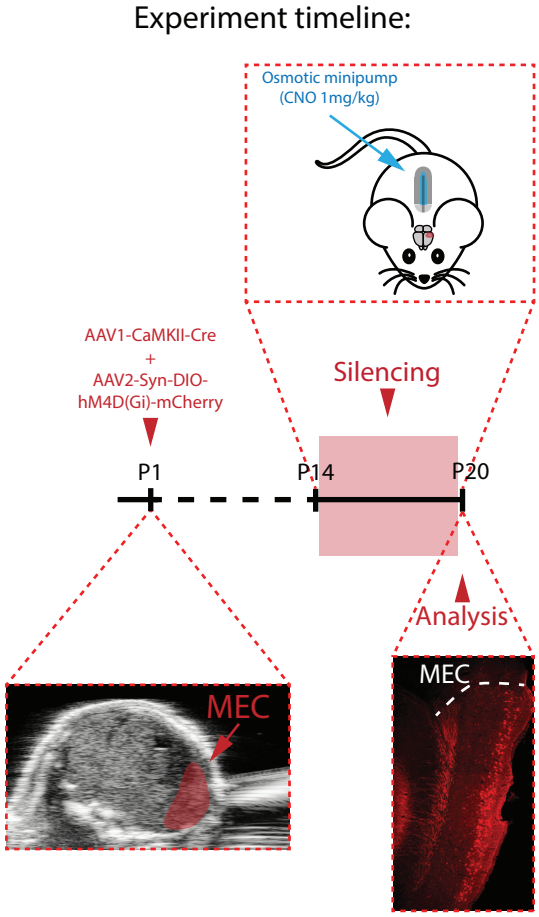

B

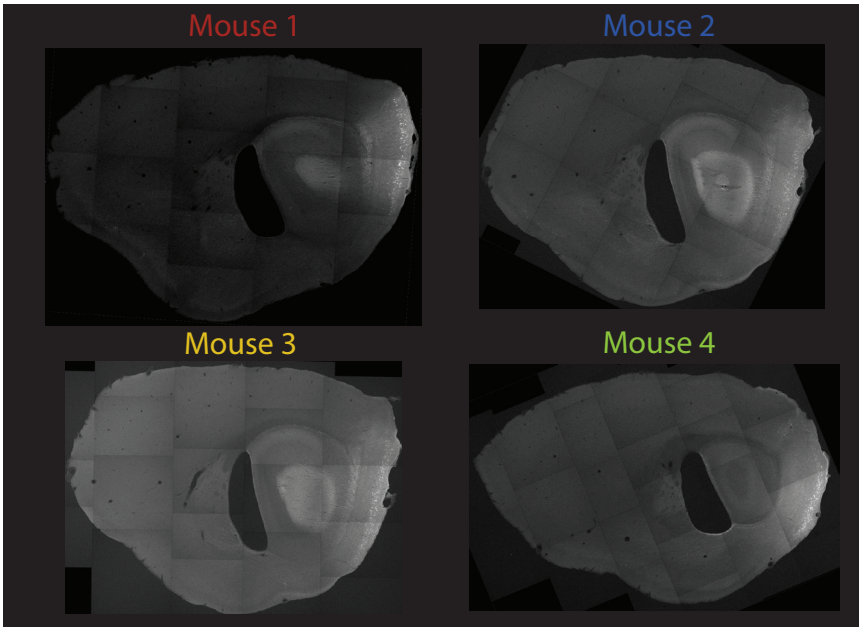

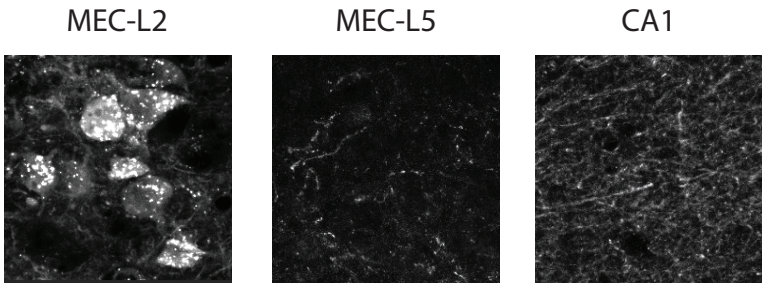

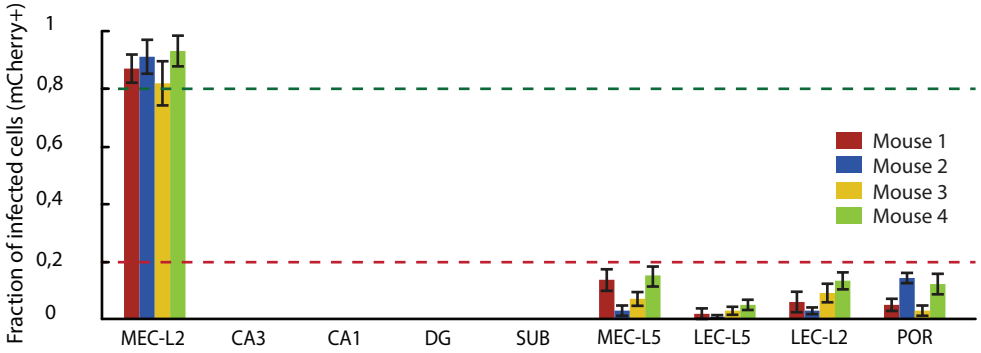

C

	MEC-L2	Hippocampus	LEC
MEC-L2	+	-	-
MEC-L5	-	-	-
LEC-L5	-	-	+
LEC-L2	-	-	+
DG	-	-	-
CA3	-	+	-
CA1	-	+	-
SUB	-	-	-
POR	-	-	-

D

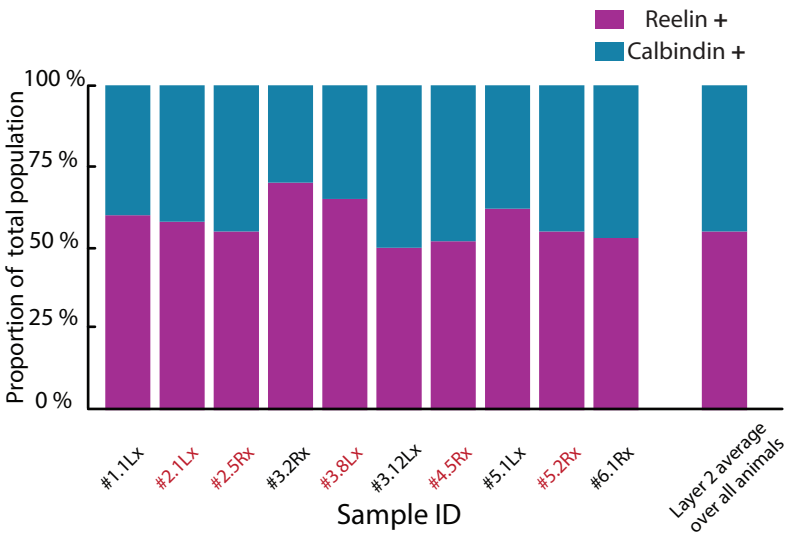

Fig. S2: Specificity of hM4D(Gi) expression after viral infection on postnatal day 1.

(**A**) Schematic illustration of experiment involving pharmacogenetic silencing of excitatory neurons in the entorhinal-hippocampal network during postnatal development. A viral mix (AAV1-CaMKII-Cre and AAV2-Syn-DIO-hM4D(Gi)-mCherry, 1:1) was injected into the brain of newborn pups at P1 in order to express hM4D(Gi) selectively in excitatory neurons, under the control of a CaMKII promoter. Injections were directed to MEC-L2, hippocampus or LEC, using ultrasound to identify structural landmarks and guide the pipette (bottom left). The anatomical specificity of the infection was later verified by imaging serial sections of the injected hemisphere, using mCherry expression as an indicator of infected cells (bottom right; 20× confocal image of a sagittal section from a P20 animal, maximum intensity projection). Somas of infected neurons were located selectively in the target area (MEC-L2). Staining in deep layers and hippocampus reflect axons only. Top panel: Pharmacogenetic silencing of virally infected neurons was performed two weeks after injection through continuous delivery of the ligand CNO (1 mg/kg) by an osmotic minipump implanted subcutaneously on the pups' backs. CNO was delivered at a constant rate over the course of several days during maturation, typically from P14 to P20. Quantitative analysis of maturational markers was conducted on P20, at the end of the silencing window. In a subset of animals, CNO was delivered from P11 to P14. (**B**) Spread of viral infection in P1-injected animals. Upper panel: 10× confocal images of sagittal sections from 4 injected animals with selective infection in MEC-L2. White: mCherry signal. Images are maximum intensity projections (MIPs). Middle panels: 40x MIPs of infected cells in MEC-L2, MEC-L5 and axonal tracts in hippocampal area CA1 (pictures from Mouse 1). Lower panel: Fraction of NeuN+ neurons in every area with mCherry expression (mean ± S.D., same 4 animals as in the upper panel). An area was considered infected when more than 80% of the NeuN+ neurons (green dashed line) expressed mCherry (virus-positive, + in panel C), and non-infected when mCherry was expressed in fewer than 20% of NeuN+ neurons (red dashed line; virus-negative, – in C). mCherry expression was taken as an indication of effective expression of the hM4D(Gi) construct. Mice with infection rates between the two cut-offs were excluded from further analysis (unless otherwise stated, Fig. S6). 102 out of 192 injected hemispheres were included in the analysis. (**C**) Overview quantification of anatomical spread of the viral infection. Based on areas exhibiting viral expression, animals were subdivided into multiple categories for analysis (MEC-L2 specific; hippocampus specific; LEC specific; + and – as described in (B)). (**D**) In MEC-L2, the viral mix did not exhibit any tropism for either stellate or pyramidal cells. We verified the identity of mCherry+ cells with

molecular markers selective for either stellate or pyramidal cells (reelin or calbindin, respectively). Local network analysis in individual animals confirmed that the proportion of stellate/pyramidal cells among the infected neurons for each animal was comparable to the average found in the MEC-L2 network across multiple animals (> 400000 neurons from over 50 animals analyzed). *x* axis: identification codes of samples analyzed in Fig 2A and 3C. Each cumulative bar represents one animal. Silenced animals: red labels. Control animals (No Virus, CNO): black labels. *y* axis: proportions indicating relative abundance of reelin+ neurons (magenta) and calbindin+ neurons (cyan) within each population of mCherry+ neurons.

Fig. S3

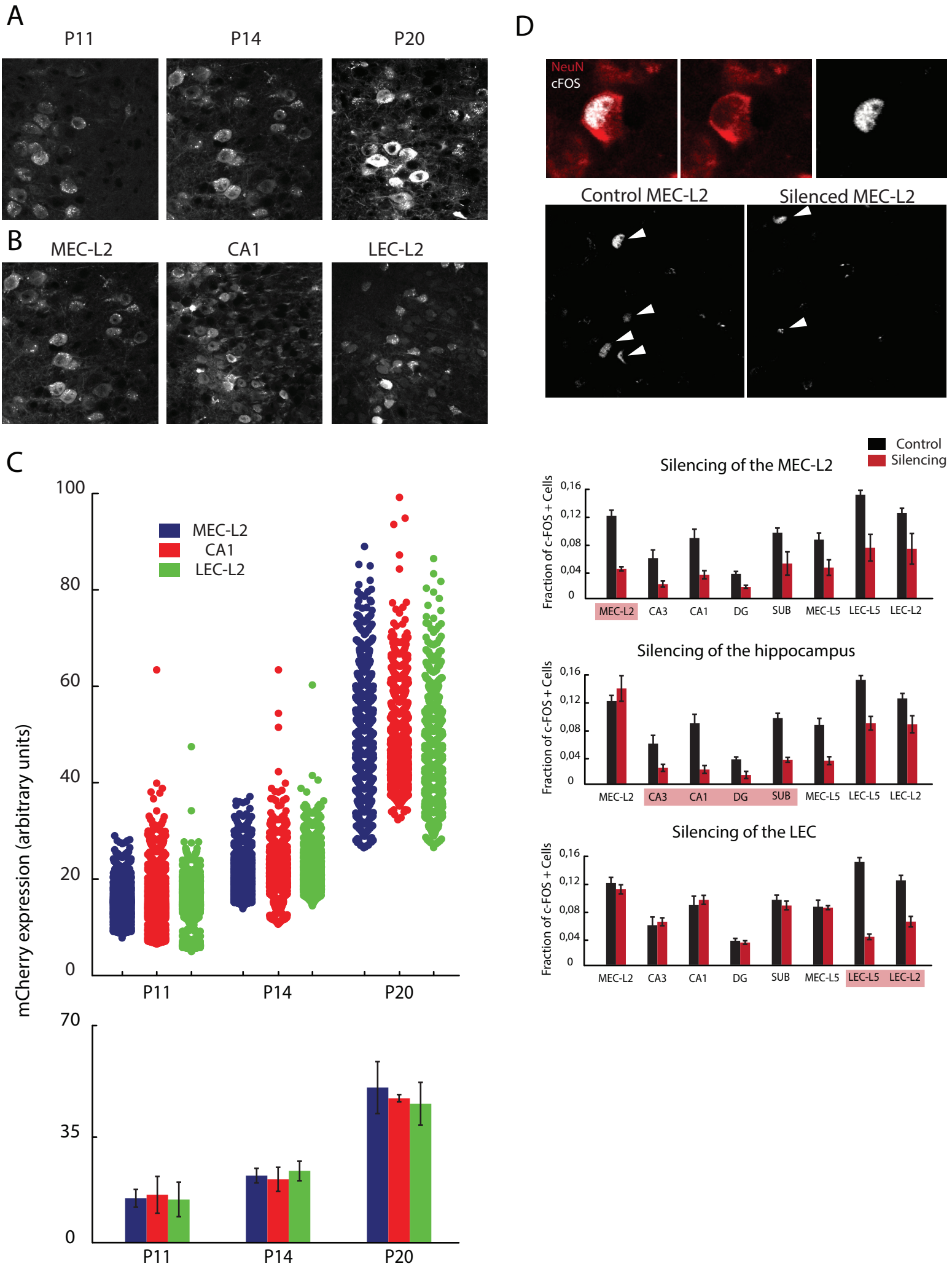
A
P11
P14
P20
B
MEC-L2
CA1
LEC-L2
C
100
80
60
40
20
0
MEC-L2
CA1
LEC-L2
mCherry expression (arbitrary units)
P11
P14
P20
70
35
0
P11
P14
P20
D
NeuN
cFOS
Control MEC-L2
Silenced MEC-L2
Control
Silencing
Silencing of the MEC-L2
Fraction of c-FOS + Cells
0,16
0,12
0,08
0,04
0
MEC-L2
CA3
CA1
DG
SUB
MEC-L5
LEC-L5
LEC-L2
Silencing of the hippocampus
Silencing of the LEC

Fig S3: Time course of hM4D(Gi) expression in infected neurons and validation of silencing.

(**A**) 40× single confocal planes showing mCherry expression (white) in MEC-L2 excitatory neurons at three postnatal ages (P11, P14 and P20). (**B**) 40× single confocal planes showing mCherry expression (white) in excitatory neurons of MEC-L2, CA1, and MEC-L2 at P14. (**C**) Quantification of mCherry expression in infected neurons of MEC-L2 (blue), CA1 (red) and LEC-L2 (green) across multiple ages. Single isosurfaces were built in Imaris around somas identified by mCherry fluorescence, and the mean intensity of the pixels included in the isosurfaces (expressed in arbitrary units, *y* axis) was taken as an indication of the level of mCherry expression in a single cell. Upper panel: values from single cells were pooled across animals for each experimental condition (each dot represents one neuron). Lower panel: bars represent average values across animals (means ± S.D.; >16000 neurons from 15 animals). **(D)** Upper panels: high magnification (60×) single confocal planes showing c-FOS expression (white) in neurons of MEC-L2 (NeuN, red) from a control mouse. Middle panels: low magnification (28×) single confocal planes showing c-FOS expression (white) in MEC-L2 of control (left) and silenced (right) animals. Lower panels: fraction of NeuN+ neurons with nuclear expression of c-FOS (c-FOS+) across subdivisions of the entorhinal-hippocampal circuit in control animals (black) and silenced animals (red). *y* axis: Fraction of double positive NeuN/c-FOS neurons. DREADD-mediated silencing induces a decrease in c-FOS expression in areas expressing the viral construct (*x* axis, red boxes) as well as downstream stations of the transverse hippocampal circuit (mean ± S.D., Student's t-test comparisons to controls, $t > 6.5$ and $P < 0.035$, $t < 1.63$ and $P > 0,52$ for comparisons with areas upstream of the infection site).

Fig. S4

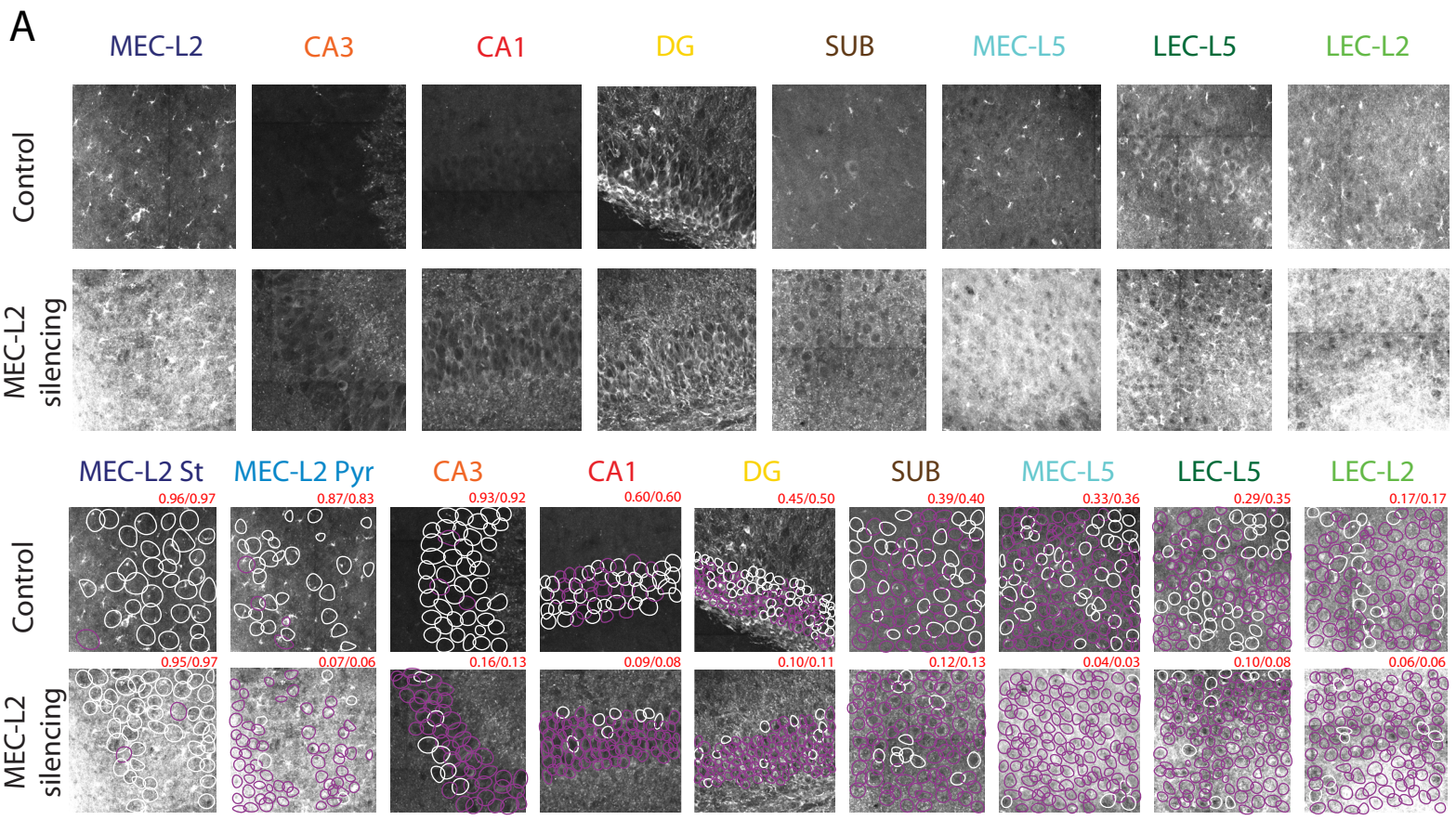

Silencing of MEC-L2

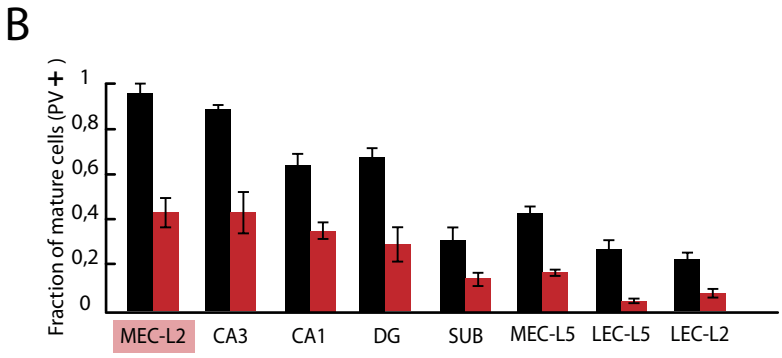

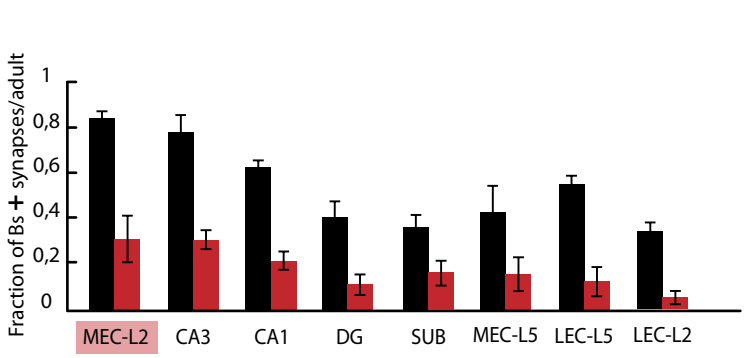

Silencing of hippocampus

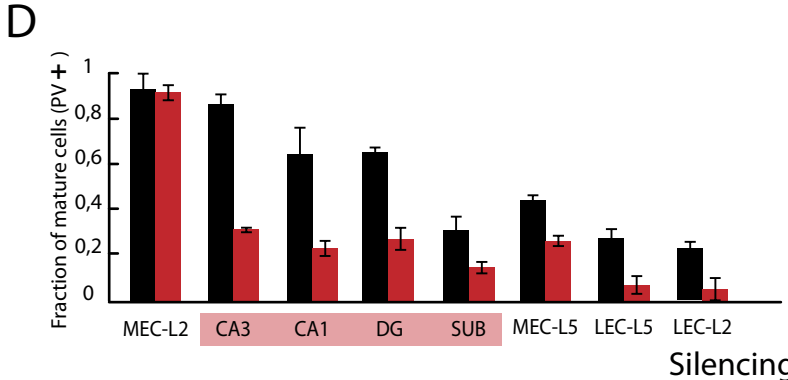

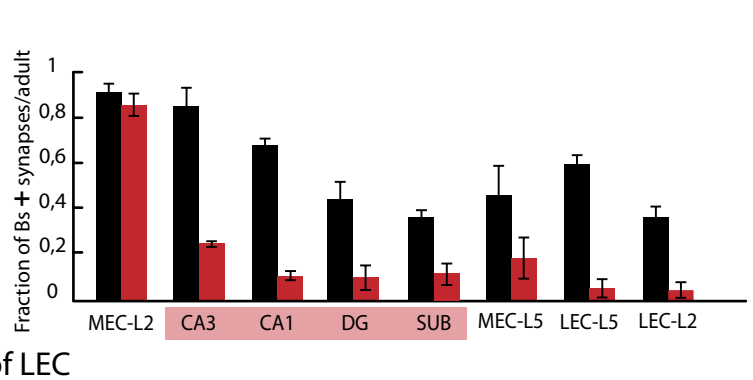

Silencing of LEC

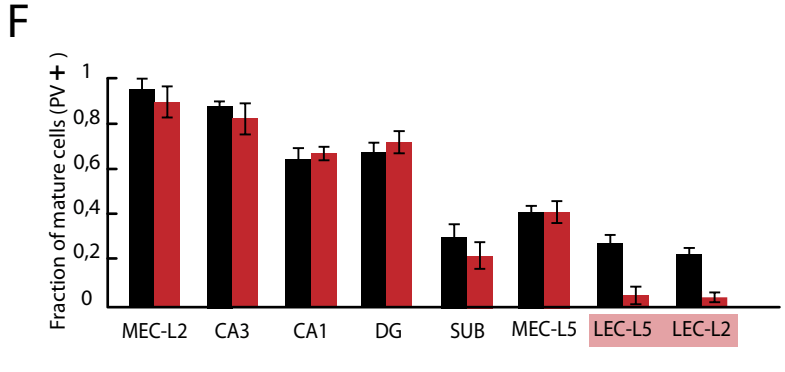

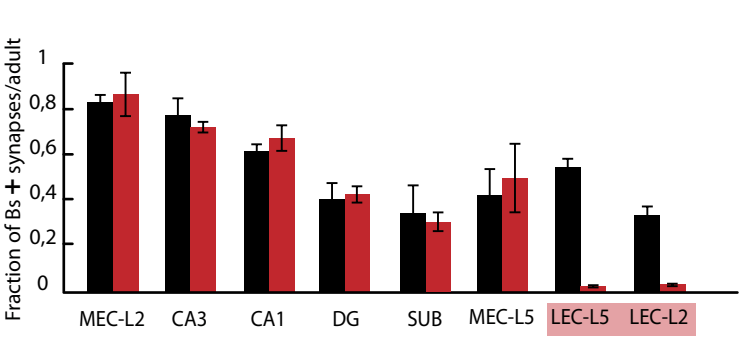

Fig. S4: PV expression and synaptic density upon developmental silencing of particular subregions of the entorhinal-hippocampal network.

(**A**) Upper pair of rows: confocal images showing DCX expression (white) across subregions of the entorhinal-hippocampal circuit. Upper row: control animals. Lower row: same regions after silencing MEC-L2 excitatory neurons for 6 days. Image locations are indicated in Fig. S1A. Single fields of view were acquired with a 40×/1.3NA oil immersion objective (zoom 0.6×), and processed together, with constant parameters. Lower pair of rows: processed dataset. Individual neurons (identified automatically based on the expression of somatic markers, as in Fig. S1C) have been labelled as regions of interest (ROI), and each individual ROI has been hand-drawn onto the maximum intensity projection of the DCX signal across the 3D dataset. Single ROIs (solid circles) are colour-coded based on presence (magenta) or absence (white) of DCX, as in Fig. S1C. Note that the overall level of fluorescence present in specific regions of an image (hippocampus), or diffused through the whole extent of the cell layer (cortex), can be the result of neuropil contamination, which has been excluded from our single-cell analysis as previously explained (Fig. S1C). Above each image its proportion of DCX- cells, compared to the mean value across animals (left and right of slash, rerspectively; means as in Fig. 2A) is indicated. **(B)-(G)**. Individual panels show local fractions of PV+ cells (**B**, **D**, **F**) and bassoon labelled synaptic puncta (Bs+; **C**, **E**, **G**) at P20 in different parts of the entorhinal-hippocampal circuit. Both PV+ and Bs+ numbers are normalized to counts from adult animals (P90). *x* axis: Local network under investigation. Areas highlighted in red on the *x* axis-label indicate silenced regions. (**B**) MEC-L2-specific silencing prevented maturation-related increase in PV expression throughout the entorhinal-hippocampal network (> 15000 neurons analyzed from at least 3 animals per experimental group; mean ± S.D., silenced vs. control: $t > 10.50$ and $P < 0.0001$). (**C**) MEC-L2-specific silencing prevented maturation-related increase in density of synaptic puncta throughout the entorhinal-hippocampal network.(mean ± S.D., $t > 8.463$ and $P < 0.0001$). (**D**) Hippocampus-specific silencing did not affect PV expression in MEC-L2, but affected the rest of the network ($t = 0.18$ and $P = 0.1$ for MEC-L2, $t > 10.1$ and $P < 0.0001$ for all other comparisons; > 15000 neurons analyzed from at least 3 animals per experimental group). (**E**) Hippocampus-specific silencing did not affect synaptic densities in MEC-L2, but reduced densities in the rest of the network ($t = 0.20$ and $P = 0.80$ for MEC-L2, $t > 8.5$ and $P < 0.0001$ for all other comparisons). (**F**) LEC-specific silencing affected PV expression only in LEC-L5 and LEC-L2 ($t > 5.1$ and $P < 0.0001$ for the LEC, $t < 0.95$ and $P > 0.2$ for all other comparisons; > 15000 neurons analyzed from at least 3 animals per experimental group). (**G**)

LEC-specific silencing affected synaptic densities only in LEC-L5 and LEC-L2 ($t > 8.1$ and $P < 0.0001$ for the LEC, $t < 1.5$ and $P > 0.52$ for all other comparisons).

Fig. S5

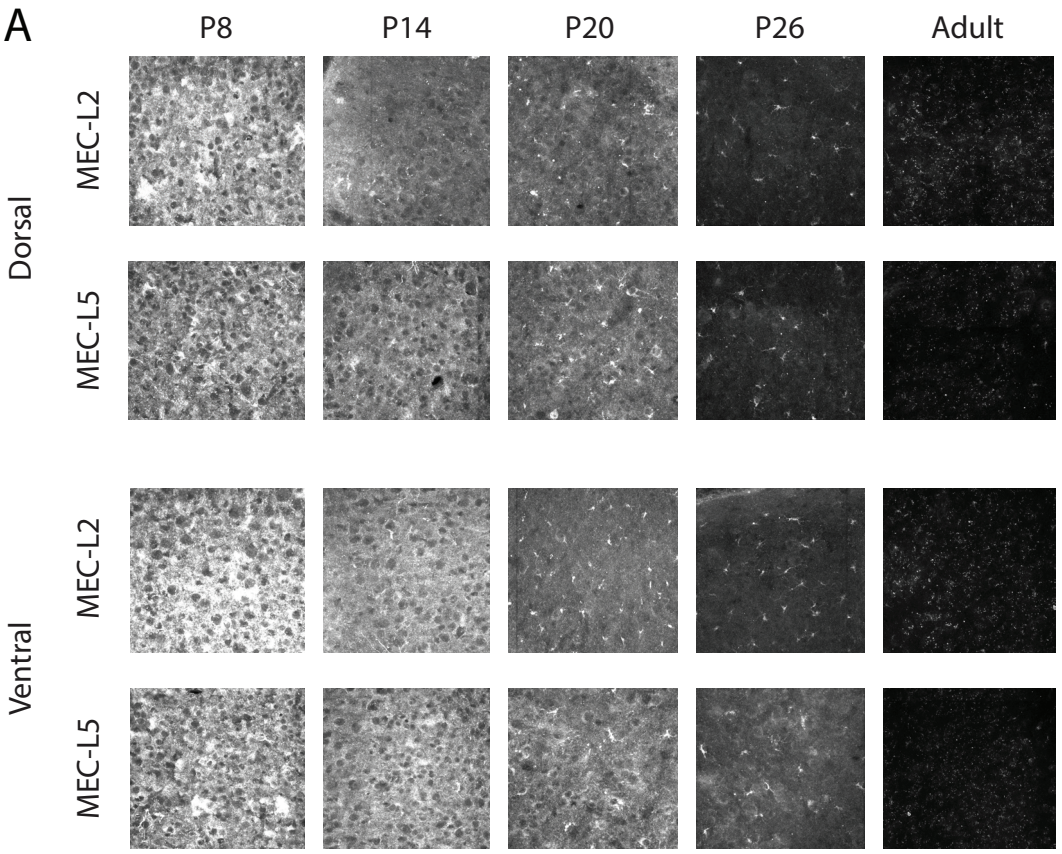
A
P8
P14
P20
P26
Adult
Dorsal
MEC-L2
MEC-L5
Ventral
MEC-L2
MEC-L5

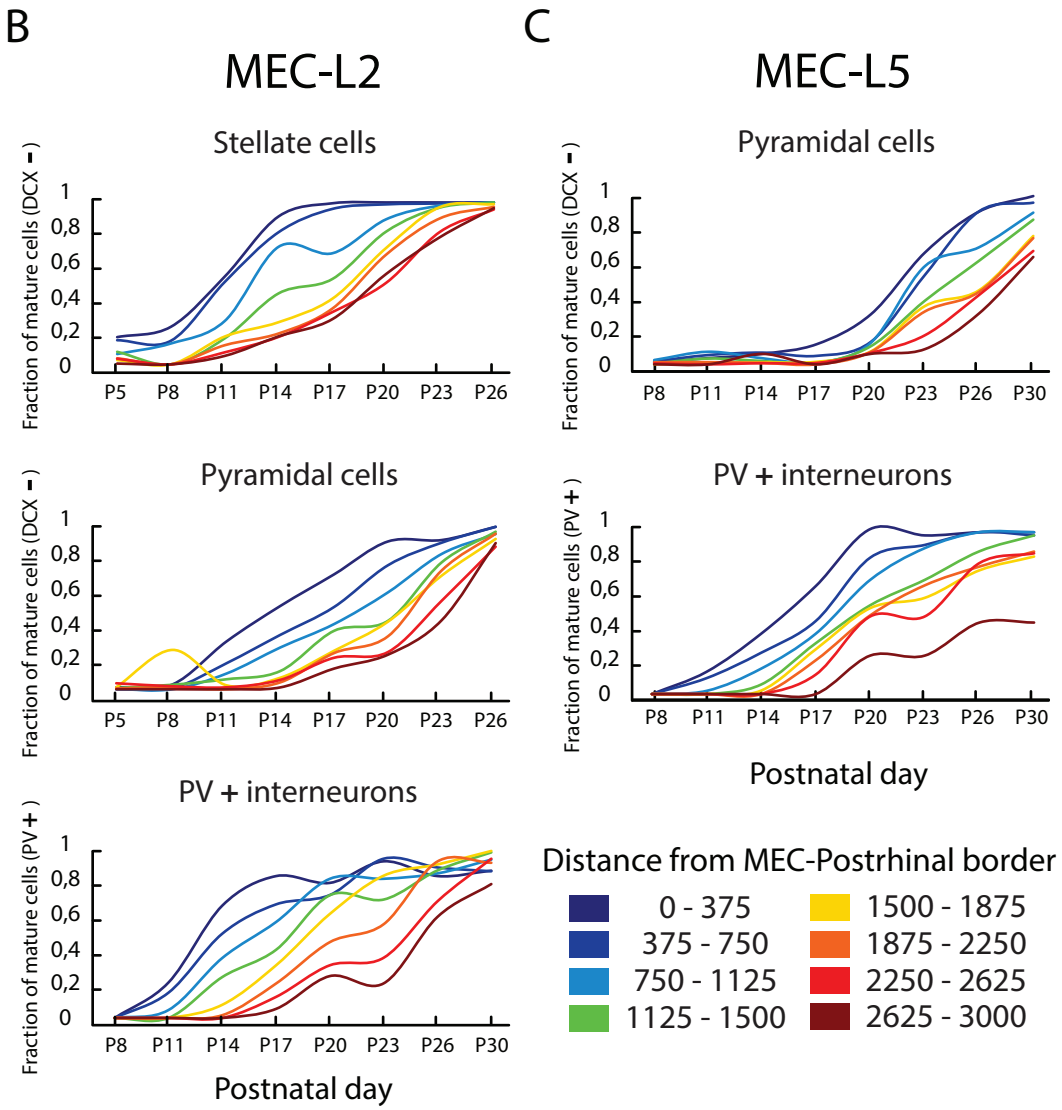
B
MEC-L2
Stellate cells
Fraction of mature cells (DCX -)
Pyramidal cells
Fraction of mature cells (DCX -)
PV + interneurons
Fraction of mature cells (PV +)
Postnatal day
C
MEC-L5
Pyramidal cells
Fraction of mature cells (DCX -)
PV + interneurons
Fraction of mature cells (PV +)
Postnatal day
Distance from MEC-Postrhinal border
0 - 375
375 - 750
750 - 1125
1125 - 1500
1500 - 1875
1875 - 2250
2250 - 2625
2625 - 3000

Fig. S5: Dorso-ventral topography of MEC maturation.

(**A**) Confocal images showing DCX expression (white) in dorsal and ventral MEC at multiple time points during the first postnatal month (image locations indicated in Fig S1B; dorsal and ventral MEC analyzed at the same medio-lateral location). Single fields of views were acquired with a 40×/1.3NA oil immersion objective (zoom 0.6×), and processed together, with constant parameters.

(**B**) Dorso-ventral topography of maturation in MEC-L2 (B) and MEC-L5 (C). Cumulative distributions are colour coded by location along the dorso-ventral axis of the MEC, from dorsal (blue) to ventral (red), with 0 set at the border between postrhinal and entorhinal cortex. *x* axis: day after birth. Upper panel: cumulative distributions of DCX– stellate cells. *y* axis: local fraction of reelin+ cells expressing DCX below detection level. 0: All cells express DCX. 1: No cells express DCX. 2-way ANOVA with Group and Segment as factors (Group × Segment: $F(7, 32) > 29.3$, $P < 0.0001$. The comparison between the first and second location was not significant, Group × Segment: $F(7, 32) = 0.98$, $P = 0.72$). Middle panel: cumulative distributions of DCX– pyramidal cells. *y* axis: local fraction of calbindin+ cells expressing DCX below detection level. 0: All cells express DCX. 1: No cells express DCX. Group × Segment: $F(7, 32) = 62.4$, $P < 0.0001$). Lower panel: cumulative distributions of PV+ neurons normalized to the adult network (P90-120). *y* axis: local fraction of PV+ network expressing PV at the time of analysis. 0: No cell expresses PV. 1: All cells express PV. (Group × Segment: $F(7, 32) = 43.6$, $P < 0.0001$). (**C**) Dorso-ventral topography of MEC-L5 maturation. Upper panel: cumulative distributions of DCX–, NeuN+ cells. *y* axis: local fraction of NeuN+ cells expressing DCX below detection level. 0: All cells express DCX. 1: No cells express DCX. *x* axis: day after birth. Color codes describe location along the dorso-ventral axis of the MEC, from dorsal (blue) to ventral (red). 0 is set at the border between postrhinal and entorhinal cortex. Group × Segment: $F(7, 32) = 32.4$, $P < 0.001$). Lower panel: cumulative distributions of PV+ neurons normalized by the adult network (P90-120). *y* axis: local fraction of the adult PV+ network expressing PV at the time of the analysis. 0: No cell expresses PV. 1: All cells express PV. *x* axis: day after birth. Color code as in (A). Group × Segment: $F(7, 32) = 52.7$, $P < 0.0001$).

Fig. S6

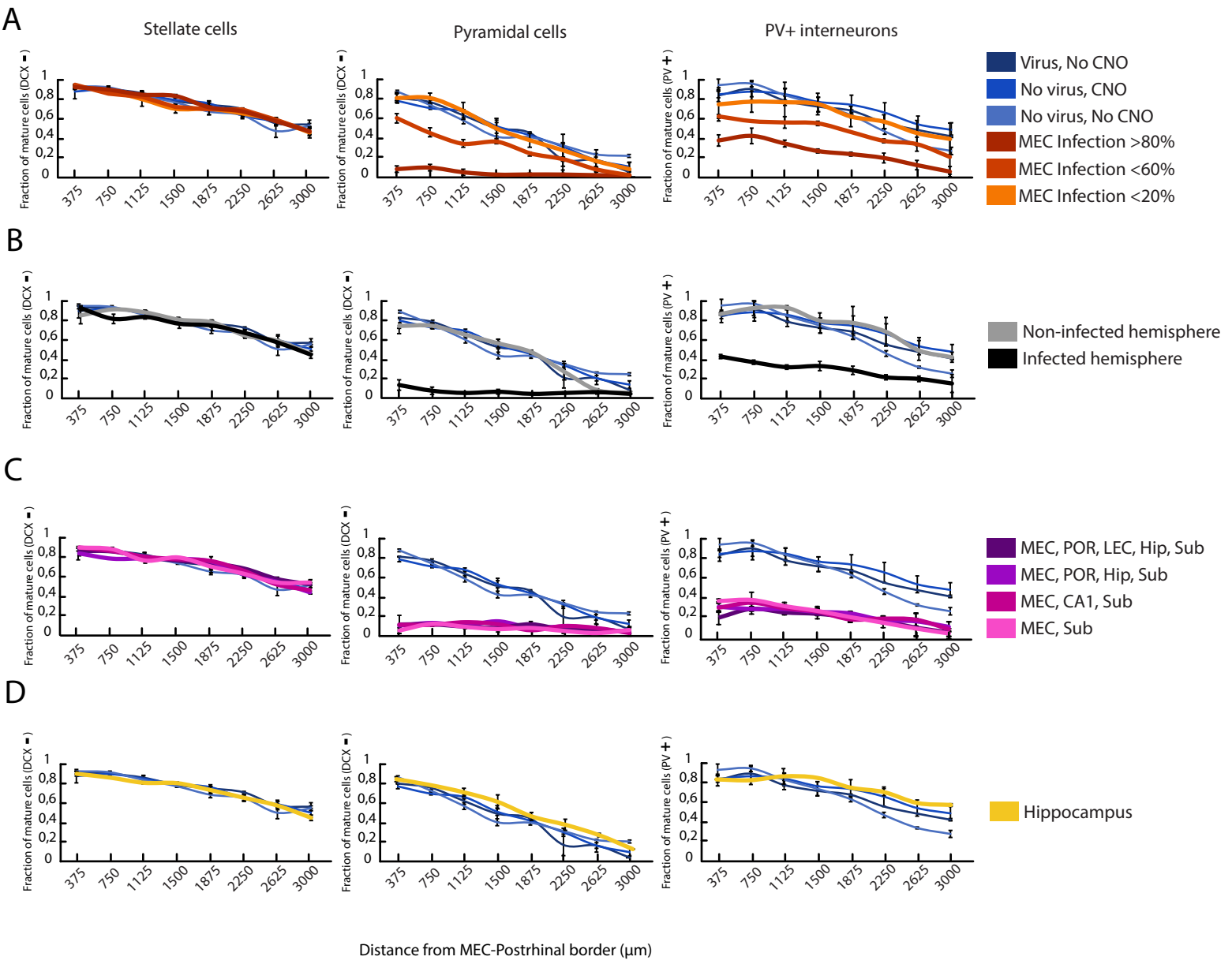
A
Stellate cells
Pyramidal cells
PV+ interneurons
Fraction of mature cells (DCX +)
Fraction of mature cells (PV +)
Virus, No CNO
No virus, CNO
No virus, No CNO
MEC Infection >80%
MEC Infection <60%
MEC Infection <20%
B
Non-infected hemisphere
Infected hemisphere
C
MEC, POR, LEC, Hip, Sub
MEC, POR, Hip, Sub
MEC, CA1, Sub
MEC, Sub
D
Hippocampus
Distance from MEC-Postrhinal border (μm)

Fig. S6: Local analysis of maturation in MEC-L2 excitatory and inhibitory neurons upon developmental silencing.

(**A**) Effect of silencing MEC-L2 on network maturation as a function of the fraction of neurons silenced. The fraction of DCX– pyramidal cells and PV+ interneurons was reduced in proportion to the fraction of neurons infected. Values in control animals were from three categorically different groups: (i) No virus, No CNO; (ii) Virus, No CNO; (iii) No Virus, CNO (different shades of blue). DCX–fractions ranged from 0.06 to 0 when more than 80% of the excitatory cells of MEC-L2 were silenced (2-way ANOVA with Group and Segment as factors, every combination of >80% silencing vs. control groups: $F(7, 32) > 10.6$ and $P < 0.0001$, in agreement with Fig. 3B). Fractions ranged from 0.60 to 0 when the proportion of MEC-L2 neurons silenced was between 20 and 60% (Group × Segment: $F(7, 32) > 4.7$ and $P < 0.01$), and from 0.83 to 0.07 when less than 20% of MEC-L2 neurons were silenced (Group × Segment: $F(7, 32) < 1.3$ and $P > 0.4$). Values for PV+ neurons ranged from 0.98 to 0.42 along the dorso-ventral MEC axis for controls, from 0.43 to 0.07 when more than 80% of the excitatory cells of MEC-L2 were silenced (Group × Segment: $F(7, 32) > 7.9$ and $P < 0.0001$, in agreement with Fig. 3B), from 0.70 to 0.24 when the proportion of neurons silenced ranged from 20 to 60% (Group × Segment: $F(7, 32) > 6.9$ and $P < 0.001$), and from 0.86 to 0.45 when less than 20% of neurons were silenced in MEC-L2 (Group × Segment: $F(7, 32) < 2.01$ and $P > 0.2$). For stellate cells, none of the silencing groups were different from controls (in agreement with Fig. 3B, Group × Segment: $F(7, 32) < 1.84$ and $P > 0.23$). (**B**) Silencing MEC of its homotopic contralateral inputs, which mainly come from pyramidal cells in layer 3 (*14, 56*), does not influence maturation of the layer2 network. Curves refer to animals in which only one hemisphere was infected by the DREADD virus, while the other was clear of infected cells (< 0.1 ± 0.005%). In the infected group, hM4D(Gi) expression was visible across layers (L2 to L5) but specific to MEC. Stellate cells (left panel), pyramidal cells (central panel) and PV+ interneurons (right panel) do not exhibit any delay in maturation of the contralateral hemisphere as a consequence of silencing (light grey curves) when compared to control animals (2-way ANOVA, Group × Segment: $F(7, 32) < 1.03$, $P > 0.23$). Note that the fraction of DCX– stellate and pyramidal cells and PV+ neurons is not different from that found in control animals in the contralateral hemisphere of infected animals. In the ipsilateral hemisphere, pyramidal cells and PV+ neurons, but not stellate cells, exhibited delays in maturation when compared to control animals (black, multiple comparisons between every combination of stellate, pyramidal cell and interneurons from silenced groups and their controls: Group × Segment: $F(7, 32)$: $F > 7.3$ and

$P < 0.001$ for pyramidal cells and PV+ neurons; Group × Segment: $F(7, 32)$: $F = 0.9$ and $P = 0.8$ for stellate cells). (**C**) Silencing an extensive part of the retrohippocampal area did not affect maturation of stellate cells but blocked maturation of pyramidal cells and PV+ neurons. Retrohippocampal silenced mice were split into three groups according to the spread of infection in the retrohippocampal areas (figure legend, different shades of purple). MEC layers 2 and 5 were silenced in all groups but the infection also extended into postrhinal cortex, lateral entorhinal cortex, hippocampus and subiculum in different groups. Values of DCX– pyramidal cells ranged from 0.85 to 0.11 along the dorso-ventral axis of the MEC for controls, but only from 0.04 to 0.02 when a large retrohippocampal region was silenced (Group × Segment: $F(7, 32) > 20.984$ and $P < 0.0001$). Values for PV+ neurons ranged from 0.98 to 0.42 along the dorso-ventral MEC for controls and from 0.40 to 0.02 when a large retrohippocampal region was silenced (Group × Segment: $F(7, 32) > 10.7$ and $P < 0.0001$). Stellate cells did not exhibit any differences from controls for any group of retrohippocampal silenced animals (Group × Segment: $F(7, 32) > 2.3$, $P > 0.07$). Data are from > 250000 neurons of > 30 animals, with at least 3 hemispheres for each condition. (**D**) Stellate cell, pyramidal cell and PV+ neuron maturation was not affected at any position along the dorso-ventral MEC axis when excitatory neurons in the hippocampus were silenced. Values were indistinguishable from controls for both DCX expression in stellate and pyramidal cells and for PV expression in interneurons (2-way ANOVA, Group: $F(1, 32) < 2.60$ and $P > 0.28$; Group × Segment: $F(7, 32) < 0.94$ and $P > 0.65$).

Fig. S7

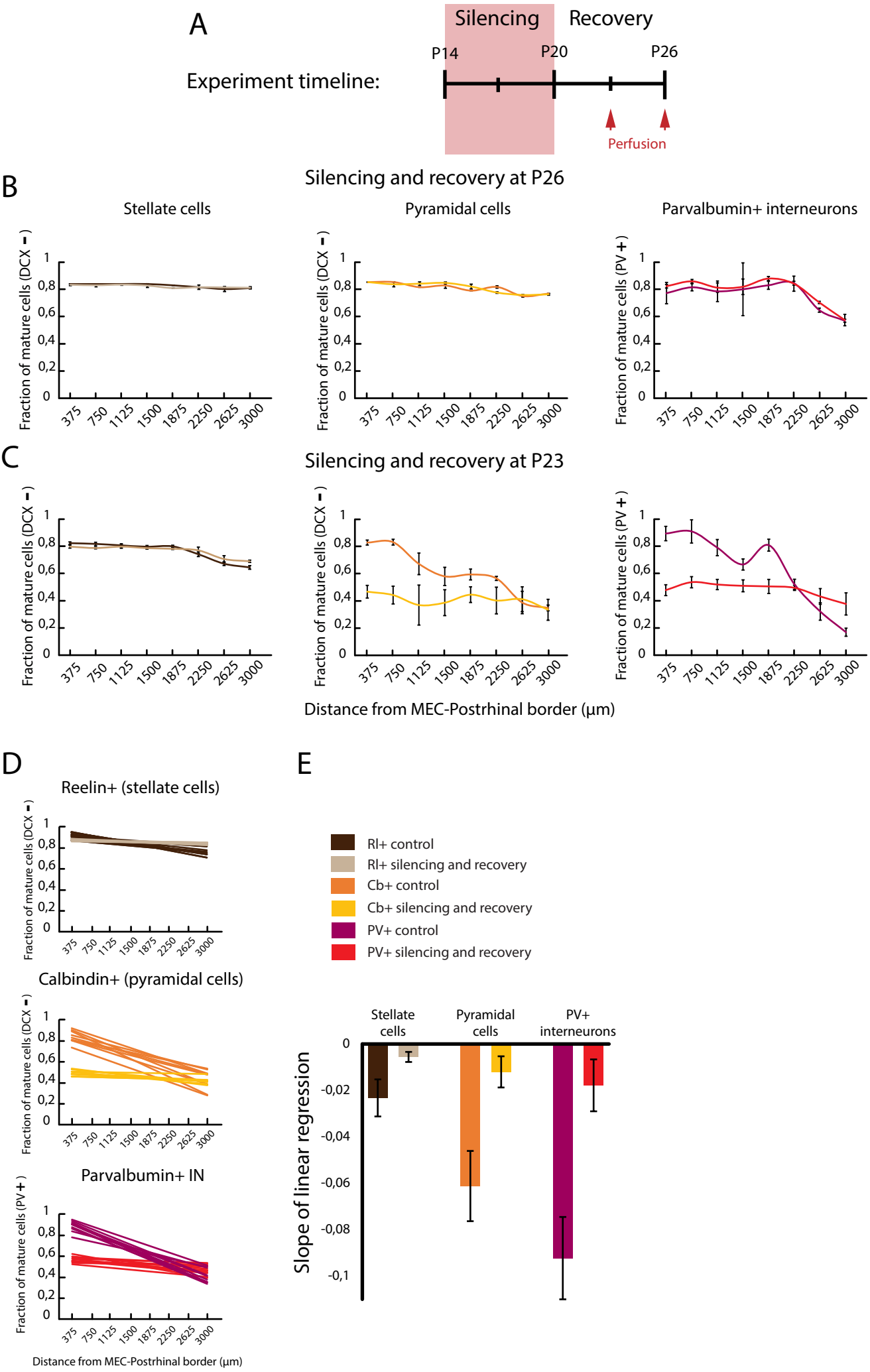
A
Experiment timeline:
Silencing
Recovery
P14
P20
P26
Perfusion
B
Silencing and recovery at P26
Stellate cells
Pyramidal cells
Parvalbumin+ interneurons
Fraction of mature cells (DCX -)
Fraction of mature cells (PV +)
C
Silencing and recovery at P23
Distance from MEC-Postrhinal border (µm)
D
Reelin+ (stellate cells)
Calbindin+ (pyramidal cells)
Parvalbumin+ IN
Distance from MEC-Postrhinal border (µm)
E
Rl+ control
Rl+ silencing and recovery
Cb+ control
Cb+ silencing and recovery
PV+ control
PV+ silencing and recovery
Stellate cells
Pyramidal cells
PV+ interneurons
Slope of linear regression

Fig. S7: Developmental silencing does not result in long-term impairment of MEC-L2 network maturation.

(**A**) To test if local silencing causes lasting damage to the network, as opposed to only delaying its maturation, we allowed a cohort of mice to recover after removal of the minipump at P20. We analyzed subsequent network maturation at two time points: P23 and P26 (red arrows). (**B**) After 6 days of recovery, at P26, DCX and PV expression levels were comparable to control animals (P26 cohort, comparison between silenced and control animals for DCX expression in pyramidal cells and PV expression in interneurons did not yield any significant difference, Group × Segment: $F(7, 32) < 0.51$, $P > 0.10$). (**C**) At P23, the fraction of DCX– pyramidal cells and PV+ interneurons was still significantly different from that of time-matched controls (No virus, Saline) at every level along the dorso-ventral axis of MEC (comparisons between pyramidal cells or interneurons and their controls: Group × Segment: $F(7, 32) > 7.23$, $P < 0.03$). However, fractions at P23 were also significantly different from values exhibited by silenced animals immediately after silencing at P20 (Fig. 3C and Fig. S6, pyramidal cells or interneurons vs. silenced animals: Group × Segment: $F(7, 32) > 4.02$ and $P < 0.01$). The findings indicate that the network was able to recover normally after silencing, and that no long-term impairment in maturation had been caused by silencing excitatory activity during development. Stellate cells were not affected by silencing at any time during recovery (all combinations of comparisons among different time points of recovery and their controls: Group × Segment: $F(7, 32) < 0.953$ and $P > 0.87$, (B) and (C) left panels). (**D**) Fraction of DCX– stellate cells (upper panel) and pyramidal cells (central panel), and PV expression in PV+ neurons (lower panel), in single sagittal sections from recovering mice at P23 (lighter colors) or time-matched control animals (darker colors). Each line represents the linear regression through the values calculated on a single sagittal slice. Note lack of dorso-ventral MEC gradient for DCX– pyramidal cells and PV+ interneurons, in contrast to control animals. For pyramidal cells, values in control animals ranged from 0.89 to 0.44 while they ranged from only 0.55 to 0.47 in recovering animals, suggesting minimal dorsal-to-ventral difference in the recovery group. Similarly, for PV+ cells, values ranged from 0.87 to 0.51 in control animals, but ranged only from 0.58 to 0.49 in silenced animals. (**E**) The slope of the linear regressions in (D) was close to 0 in pyramidal and PV+ cells of recovering animals at P23, indicating no topographical difference in maturation between dorsal and ventral MEC (Student's t-test, $t > 6.1$ and $P < 0.001$, mean ± S.D.). No significant dorsal-to-ventral difference could be observed for stellate cells in D or E.

Fig. S8

A

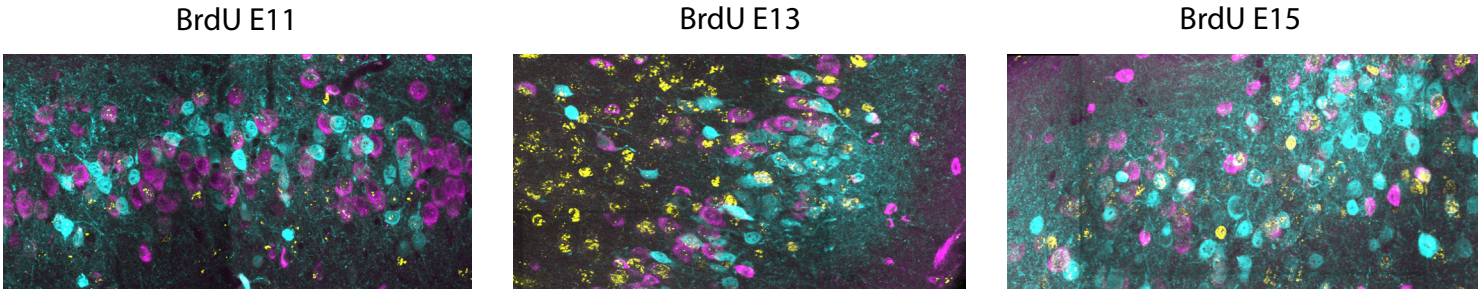
BrdU E11
BrdU E13
BrdU E15

B

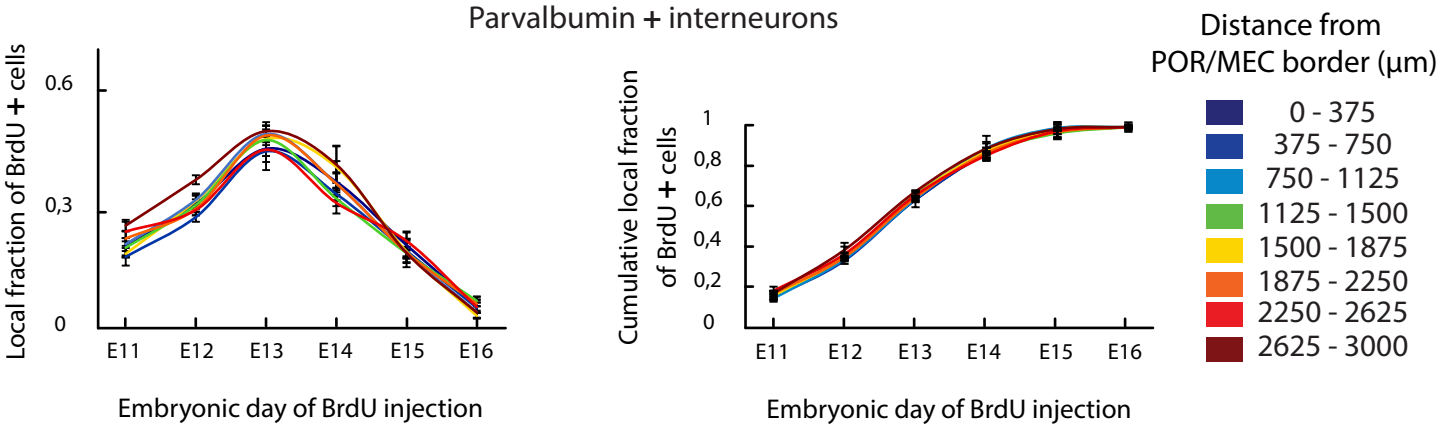
Parvalbumin + interneurons
Local fraction of BrdU + cells
0.6
0,3
0
E11 E12 E13 E14 E15 E16
Embryonic day of BrdU injection
Cumulative local fraction of BrdU + cells
1
0,8
0,6
0,4
0,2
0
E11 E12 E13 E14 E15 E16
Embryonic day of BrdU injection
Distance from POR/MEC border (µm)
0 - 375
375 - 750
750 - 1125
1125 - 1500
1500 - 1875
1875 - 2250
2250 - 2625
2625 - 3000

C

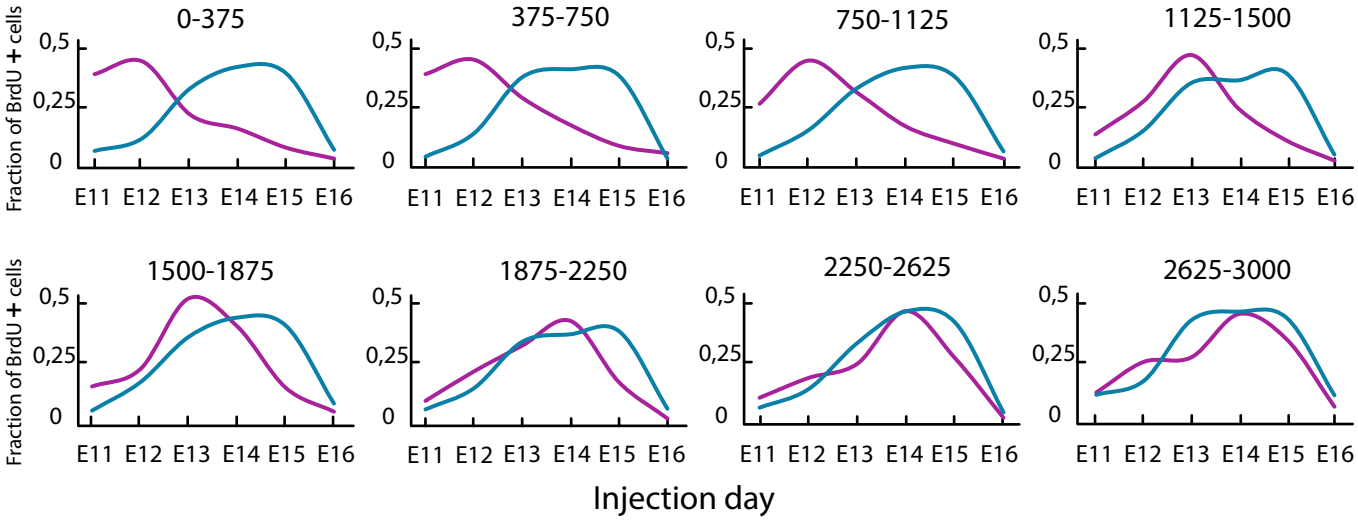
0-375
375-750
750-1125
1125-1500
1500-1875
1875-2250
2250-2625
2625-3000
Fraction of BrdU + cells
0,5
0,25
0
E11 E12 E13 E14 E15 E16
Injection day

D

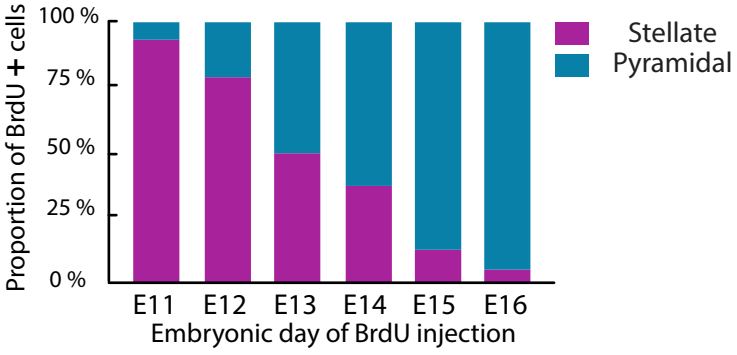
Proportion of BrdU + cells
100 %
75 %
50 %
25 %
0 %
E11 E12 E13 E14 E15 E16
Embryonic day of BrdU injection
Stellate
Pyramidal

Fig. S8: No topography in neurogenesis of PV+ cells along dorso-ventral MEC axis.

(**A**) 20× confocal images of sagittal sections from animals injected with BrdU at three time points during embryonic development (cyan: calbindin; magenta: reelin; yellow: BrdU, maximum intensity projections). (**B**) Local density estimates of neurogenesis of PV+ cells. For each of the eight blocks along MEC (Fig. 3A), we quantified the number of neurons positive for PV, and analyzed the proportion of them that exhibited BrdU staining in the nucleus. Left panel: *y* axis: proportion of the PV+ network labelled with BrdU for each embryonic day when BrdU was injected (*x* axis). 0: no PV+ cells labelled with BrdU; 1: all PV+ cells labelled with BrdU). Local peak indicates peak of neurogenesis. > 250000 neurons from at least 3 mice per time point. Right panel: cumulative distributions of the fraction of PV+ neurons labelled by BrdU across injection days (mean ± S.D.; same data as in left panel). Injection of BrdU at E10 and E17 did not produce any detectable staining in the adult, thereby marking the beginning and the end, respectively, of the MEC neurogenesis window. No staggering of curves indicates a homogenous distribution of neurogenesis along the dorso-ventral axis of MEC for PV+ cells (Injection day: $F(2, 36) = 0.79$, $P = 0.43$; Segment: $F(7, 36) = 1.53$, $P = 0.68$; Segment × Injection Day: $F(7, 36) = 0.15$, $P = 0.87$). (**C**) Neurogenesis profiles of stellate and pyramidal cells at every dorso-ventral position of the MEC. The fraction of stellate or pyramidal cells labelled by BrdU (*y* axis) was plotted as a function of BrdU injection time during development (*x* axis) for every block of MEC analyzed (ranges at top of individual panels indicate distance in μm from postrhinal/entorhinal border). Direct comparison of stellate and pyramidal cell neurogenesis at individual dorso-ventral levels revealed that stellate cells were consistently born before pyramidal cells in the dorsal half of the MEC. For pyramidal cells, the peak of neurogenesis occurred on E14 for every position along the dorso-ventral axis, while it varied from E12 to E14 for stellate cells because of their topographical distribution. (**D**) Bar diagram indicating the molecular identity of BrdU-labelled excitatory cells in MEC-L2 as a function of BrdU injection day. For all BrdU-labelled cells, we determined the expression of either reelin (stellate cells) or calbindin (pyramidal cells) with immunological methods, and calculated the proportions of the two classes of cells for every time point of BrdU injection. Note how cohorts of BrdU labelled neurons for earlier injections are dominated by stellate cells (96% of BrdU labelled cells at E11), while cohorts of BrdU labelled neurons for later injections are dominated by pyramidal cells (94% of neurons labelled at E16). The analysis was conducted on the most dorsal portion of the MEC (0-375 μm from the border to the postrhinal cortex).

Fig. S9

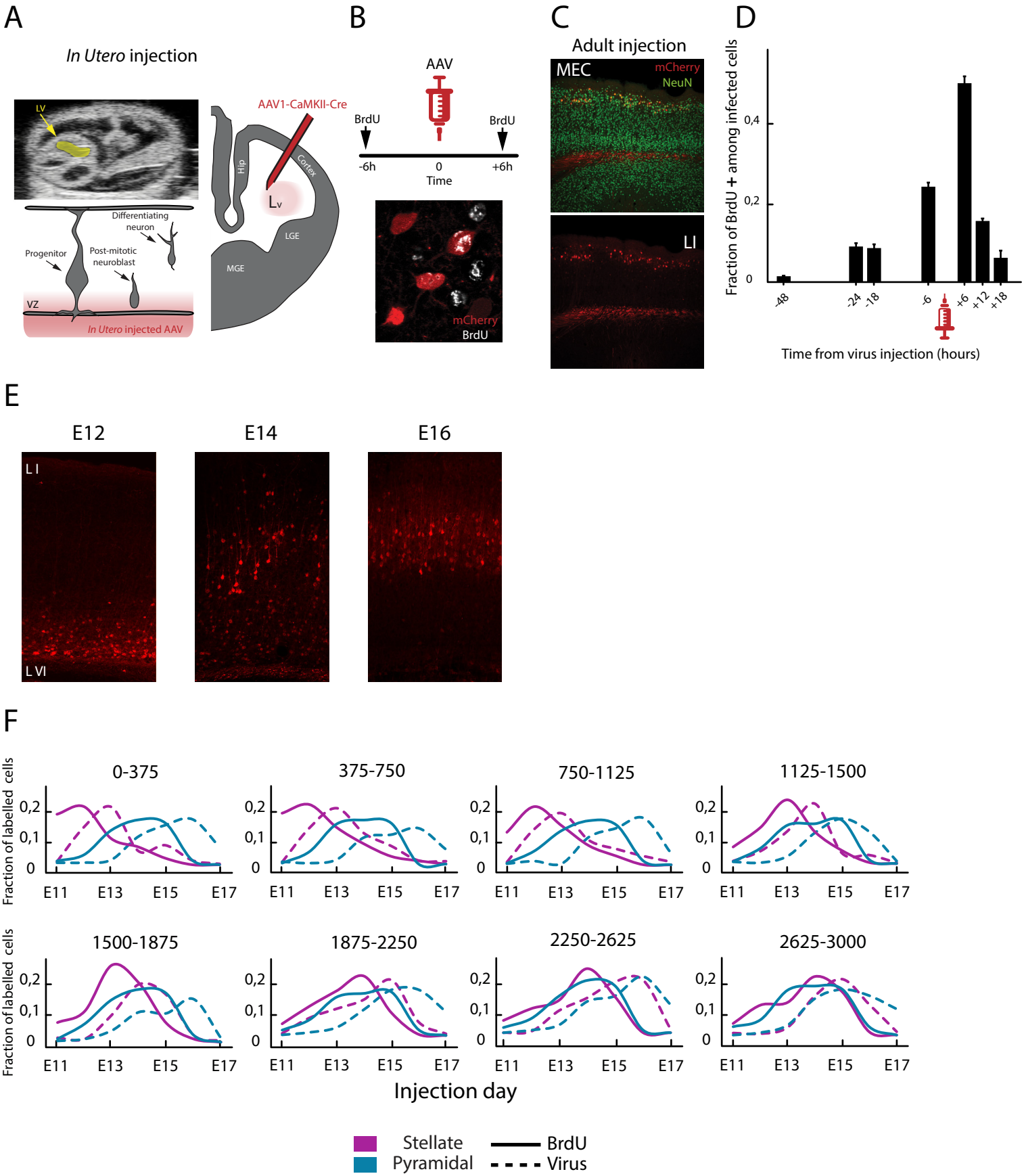
A
In Utero injection
LV
Differentiating neuron
Progenitor
Post-mitotic neuroblast
VZ
In Utero injected AAV
AAV1-CaMKII-Cre
Hip
Cortex
LV
LGE
MGE
B
AAV
BrdU
BrdU
-6h
0
+6h
Time
mCherry
BrdU
C
Adult injection
MEC
mCherry
NeuN
LI
D
Fraction of BrdU + among infected cells
0
0,2
0,4
-48
-24
-18
-6
+6
+12
+18
Time from virus injection (hours)
E
E12
E14
E16
L I
L VI
F
0-375
375-750
750-1125
1125-1500
1500-1875
1875-2250
2250-2625
2625-3000
Fraction of labelled cells
0
0,1
0,2
E11
E13
E15
E17
Injection day
Stellate
Pyramidal
BrdU
Virus

Fig. S9: Description and validation of method for genetic labelling of isochronic cohorts of neurons in the developing neocortex.

(**A**) Schematic illustrating key principles of the method. The temporal specificity of the genetic labelling is based on the deficiency of adeno-associated viral vectors to integrate into the genome of the infected cell, and on the transient permanence of post-mitotic neuroblasts in the ventricular zone (VZ) before migration. The viral construct does not integrate into the host genome, and hence the permanence of the viral genome at the episomal state should prevent inheritance of the viral construct by the progeny of infected progenitors (episomal DNA is effectively lost during cell division), while recycling of the cerebrospinal fluid should set a temporal limit for the action of the virus on progenitors and post-mitotic neuroblasts. Targeting the virus to the lateral ventricle (via ultrasound-guided injections, left upper and right panels) reduces the chances of infecting neuroblasts that have completed their final cell division before injection (and hence have migrated out of the ventricular zone, left lower panel), thereby setting a temporal limit for infection. (**B**) Double-labelling approach to verify the temporal specificity of viral labelling during development and to map the temporal extent of the neurogenesis window covered by viral injection. The pregnant mother was injected with BrdU either before or after viral injection of the embryos. Lower image: 40× maximum intensity projection, MEC-L2. White: immunodetection of BrdU; red: expression of mCherry as a consequence of viral infection. (**C**) A second viral injection (AAV1-CAG-Flex-mCherry) in the adult revealed developmentally labelled neurons in the MEC. Red, mCherry expressing neurons indicate neurons infected by the Cre virus during embryonic development, and by the FLEX-mCherry virus in the adult. Green: NeuN counterstaining. Note that a sparse number of neurons is labelled selectively in MEC-L2, as a consequence of the targeting of the virus and the time of infection during development. Red processes in deep layers represent axons projecting to the hippocampus. With this dual labelling approach, we first confirmed that our developmental viral infection was indeed effective in targeting a sparse population of cells, and that the proportion of labelled cells was constant during ageing across a period of 1 year. The infected fraction of cells in MEC-L2 after an injection at E13 was 21.4 ± 7% at 70 days post-injection, 20.8 ± 7% at 186 days post-injection and 23.1 ± 10% at 366 days post injection (Student's t-test, $t < 0.57$ and $P > 0,4$). The consistency of the number of labelled cells across days post injection rules out possible toxicity effects due to long-term permanence of the virus in the developmentally infected cells. (**D**) Fraction of mCherry-expressing cells that also stain for BrdU plotted as a function of temporal distance between BrdU and virus injection (*y* axis:

fraction of mCherry positive neurons labelled by BrdU at every time of BrdU injection. *x* axis: temporal distance between BrdU and *in utero* viral injection. 0 represents the time of viral injection. Values to the left of 0 represent time points when BrdU was injected before the virus; values to the right represent time points when BrdU was injected after the virus. Mean ± S.D.) The bell-shape appearance of the double-labelling time course confirmed that viral labelling was largely confined to neurons whose cell division happened in a window of 24-32 hours around and after the time of viral injection (note that, for comparable time points of injection, over 80% of the virally-targeted population was born with a 6-28 hour lag in comparison to BrdU-labelled neurons). Thus, the viral method is effective in labelling isochronic populations of cortical neurons. (**E**) 10× low magnification images of visual cortex from mice injected in the embryo at different times during cortical neurogenesis (E12, E14 and E16). Images display maximum intensity projections of sagittal sections located 1.56 mm lateral to bregma. Mice were first injected with AAV1-CaMKII-Cre in the lateral ventricle during the embryonic stage, then with AAV1-CAG-Flex-mCherry in the adult cortex (P90-180). mCherry signal in red. Note that labelled cells follow the characteristic inside-out progression of cortical neurogenesis (*30, 31*), validating the viral labelling method as a tool for specific labelling of isochronic cohorts. Labelling at E12 targeted selectively cells in the deepest layers of cortex (left panel). Labelling at E14 targeted predominantly layer 4, in addition to significant populations of deep and superficial layers (central panel). Labelling at E16 targeted almost exclusively superficial layers (right panel). (**F**) To further validate the *in utero* viral method, and to verify that the topographic distribution of stellate cells by neurogenesis was not an artifact of the BrdU labelling method, we analyzed the spatio-temporal distribution of virally labelled, isochronic stellate and pyramidal cells born at different times during neurogenesis, and compared these with results obtained with BrdU labelling. Each plot shows the distribution of stellate (magenta) and pyramidal cells (cyan) labelled by virus (dashed lines) or BrdU (solid lines) (*y* axis) as a function of the time of injection during gestation (*x* axis). Notice how solid and dotted lines follow the same trend at every position along the dorso-ventral MEC axis (ranges at the top of individual panels: distance from the postrhinal-entorhinal border in μm), confirming the topographical distribution of stellate cells as indicated by the BrdU approach. We did not fail to notice the rightward shift in the viral labelling curves with respect to the BrdU curves, which we attribute to the different phases of the cell cycle targeted by the two methods (S phase for BrdU and postmitotic phase for the viral injection), as well as the different temporal resolutions of the two approaches (6 vs. 24 hours, respectively).

Fig. S10

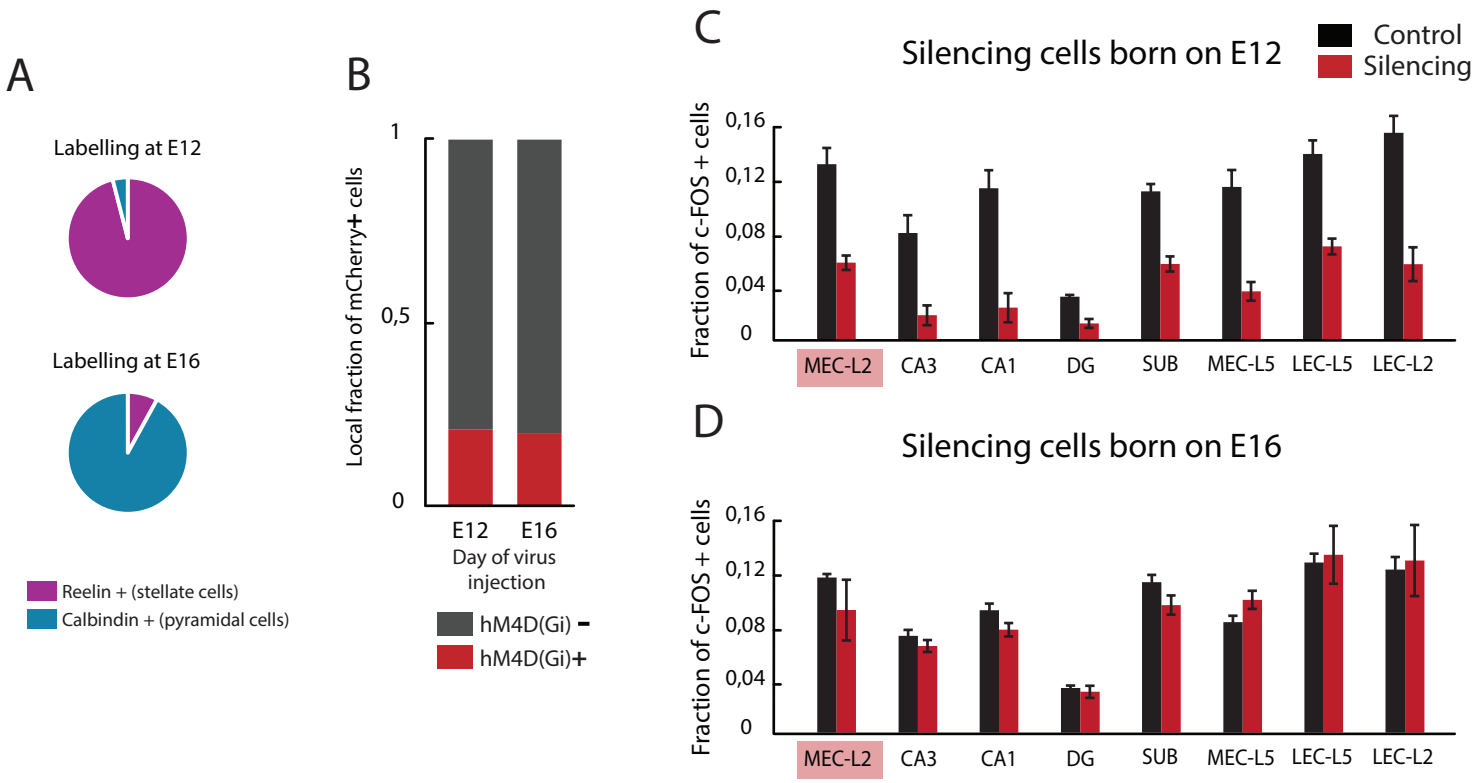
A
Labelling at E12
Labelling at E16
Reelin + (stellate cells)
Calbindin + (pyramidal cells)
B
Local fraction of mCherry+ cells
1
0,5
0
E12
E16
Day of virus injection
hM4D(Gi) –
hM4D(Gi)+
C
Silencing cells born on E12
Control
Silencing
Fraction of c-FOS + cells
0,16
0,12
0,08
0,04
0
MEC-L2
CA3
CA1
DG
SUB
MEC-L5
LEC-L5
LEC-L2
D
Silencing cells born on E16
Fraction of c-FOS + cells
0,16
0,12
0,08
0,04
0
MEC-L2
CA3
CA1
DG
SUB
MEC-L5
LEC-L5
LEC-L2

Fig. S10: Selective silencing of stellate or pyramidal cells in MEC-L2.

(**A**) Isochronic cohorts of neurons labelled by injection of the virus early during neurogenesis (E12) are dominated by stellate cells, which constitute 96 ± 3% of the infected neurons (upper pie chart), while isochronic cohorts of neurons labelled late during neurogenesis (E16) are dominated by pyramidal neurons, which constitute 92 ± 4% of the infected neurons (lower pie chart). Magenta: virally infected cells expressing reelin; cyan: virally infected cells expressing calbindin. (**B**) Fraction of the local network of excitatory cells in MEC-L2 expressing mCherry as a consequence of infection by AAV2-Syn-DIO-hM4D(Gi)-mCherry. Red bars: NeuN+ and mCherry+, Grey bars: NeuN+ and mCherry–. The fraction is 20 ± 3% for the animals injected at E12 and 18 ± 4% for animals injected at E16 (> 4000 cells from at least three animals for each injection group). (**C-D**) Fraction of NeuN+ neurons exhibiting nuclear expression of c-FOS (c-FOS+) across subdivisions of the entorhinal-hippocampal circuit in control animals (black) and silenced animals (red) (*y* axis: Fraction of double positive NeuN/c-FOS neurons. 0: no neurons express c-FOS; 1: all neurons express c-FOS). DREADD-mediated silencing induced a decrease in the fraction of c-FOS+ cells in the areas expressing the viral construct (*x* axis, red boxes) as well as areas downstream of the injected region only when isochronic neurons born on E12 were silenced (**C**, mean ± S.D., Student's t-test comparisons to controls, $t > 9.42$ and $P < 0.001$) and not when the hM4D receptor targeted isochronic neurons born on E16 (**D**; $t < 2.72$ and $P > 0.58$).

Fig. S11

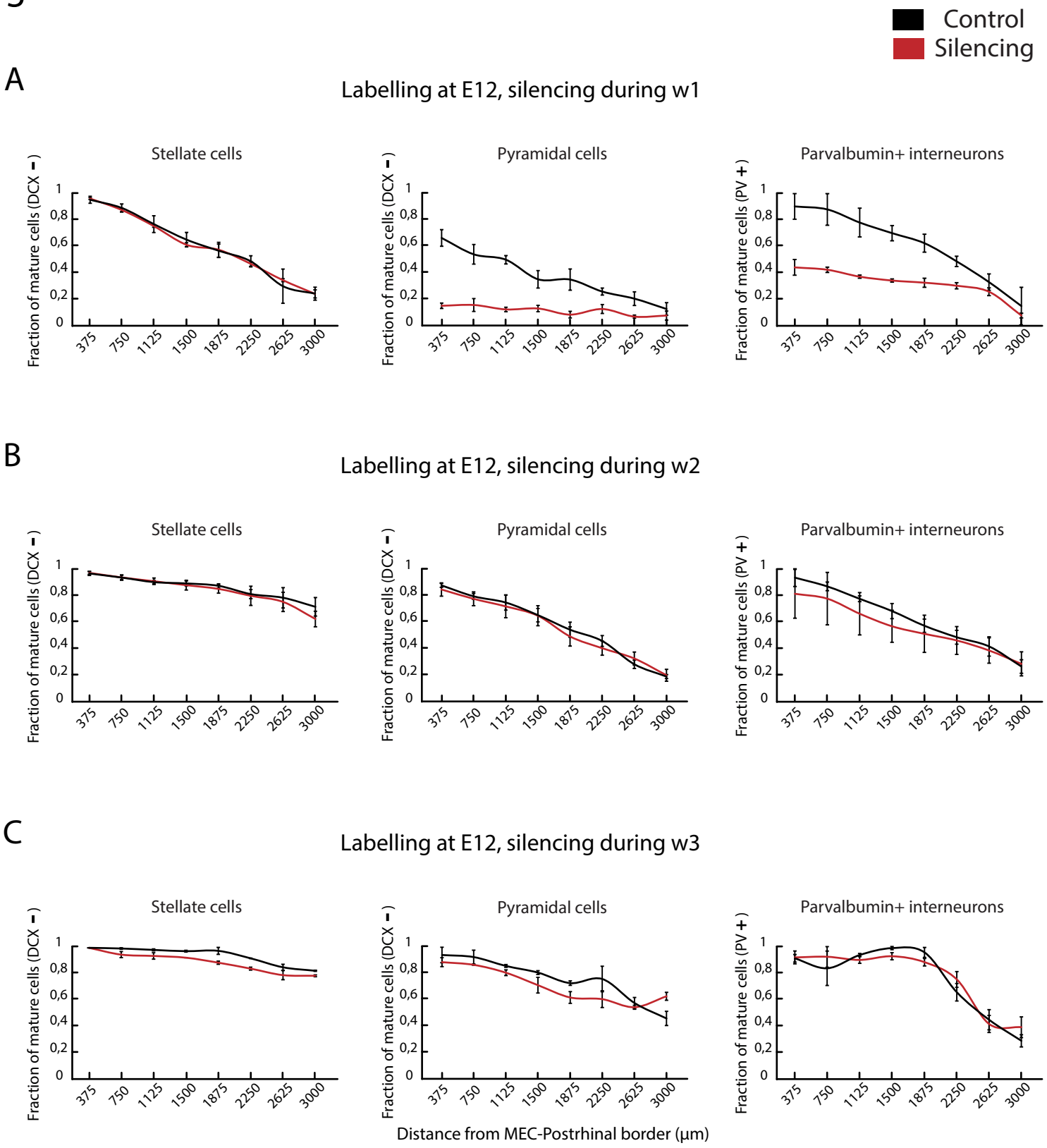
Control
Silencing
A
Labelling at E12, silencing during w1
Stellate cells
Pyramidal cells
Parvalbumin+ interneurons
Fraction of mature cells (DCX −)
Fraction of mature cells (PV +)
0
0,2
0,4
0,6
0,8
1
375
750
1125
1500
1875
2250
2625
3000
B
Labelling at E12, silencing during w2
Stellate cells
Pyramidal cells
Parvalbumin+ interneurons
C
Labelling at E12, silencing during w3
Stellate cells
Pyramidal cells
Parvalbumin+ interneurons
Distance from MEC-Postrhinal border (µm)

Fig. S11: Silencing stellate cells born on E12 blocks maturation in the local MEC-L2 network.

(**A**) Silencing stellate cells born at E12 during w1 (P14-P17) reduced the downregulation of DCX in pyramidal cells. The fraction of pyramidal cells with DCX expression below detection level ranged from 0.68 ± 0.07 (dorsal sector) to 0.11 ± 0.04 (ventral sector) in control animals (central panel, black line), and from only 0.14 ± 0.02 to 0.06 ± 0.04 in silenced animals (red line, Group × Segment: $F(7, 32) = 83.90$, $P = 0.0001$). Right panel: silencing stellate cells born at E12 during w1 (P14-P17) prevented maturation-related increase in the fraction of interneurons expressing PV. The fraction of PV-expressing cells, normalized to adult levels, ranged from 0.89 ± 0.10 (dorsal sector) to 0.09 ± 0.09 (ventral sector) in controls, and from only 0.40 ± 0.06 to 0.01 ± 0.009 in silenced animals (Group × Segment: $F(7, 32) = 64.2$, $P = 0.0001$). (**B**) and (**C**) No significant difference in DCX expression in pyramidal cells could be detected between silenced and control animals when CNO was delivered in a time-unmatched fashion during w2 (P17-P20, B; analysis at P20) or w3 (P20-P23, C; analysis at P23) (central panels, Group: $(1, 32) < 2.97$ and $P > 0.12$; Group × Segment: $F(7, 32) < 1.65$, $P > 0.54$). Similarly, there was no significant difference in PV expression between silenced and control animals when CNO was delivered in a time-unmatched fashion during w2 (P17-P20, B) or w3 (P20-P23, C) (right panels; Group: $F(1, 32) < 1.52$ and $P > 0.09$; Group × Segment: $F(7, 32) < 2.12$, $P > 0.63$). Stellate cells were not affected by silencing when CNO was given in a time-matched fashion (A, left panel, Group: $F(1, 32) = 0.76$ and $P = 0.89$; Group × Segment: $F(7, 32) = 2.30$, $P = 0.30$), or when silencing was offset from the normal maturation period (B and C, left panels, w2 vs. w3, Group: $F(1, 32) < 1.52$ and $P > 0.39$; Group × Segment: $F(7, 32) < 1.62$ and $P > 0.47$).

Fig. S12

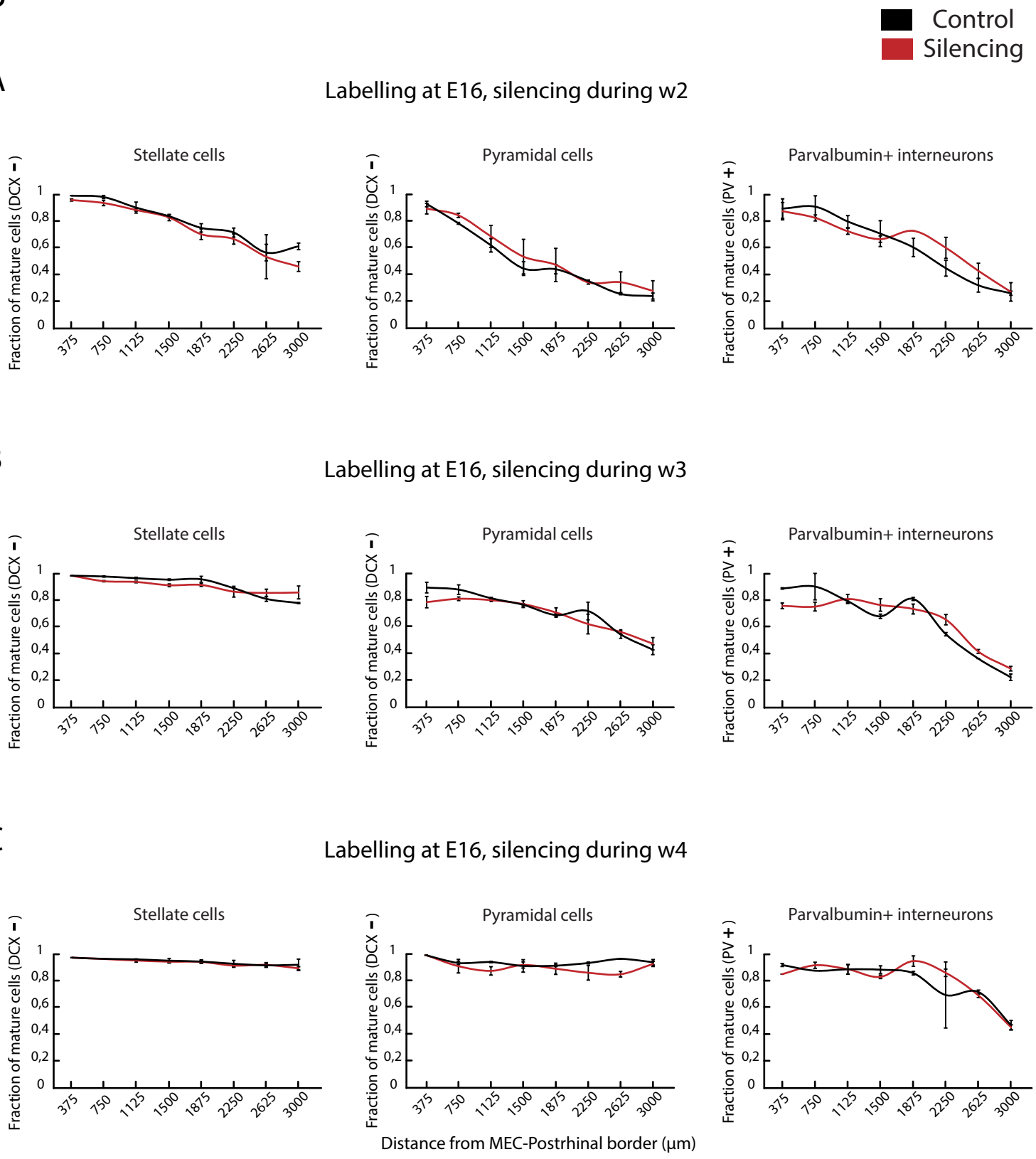
Control
Silencing
A
Labelling at E16, silencing during w2
Stellate cells
Pyramidal cells
Parvalbumin+ interneurons
Fraction of mature cells (DCX −)
Fraction of mature cells (PV +)
0
0,2
0,4
0,6
0,8
1
375
750
1125
1500
1875
2250
2625
3000
B
Labelling at E16, silencing during w3
C
Labelling at E16, silencing during w4
Distance from MEC-Postrhinal border (µm)

Fig. S12: Silencing pyramidal cells born on E16 does not affect maturation of the local MEC-L2 network.

(**A**), (**B**) and (**C**) Pyramidal cell-specific silencing did not affect maturation of the local MEC-L2 network. Silencing pyramidal neurons born at E16 produced no significant change in the expression of DCX in pyramidal cells (Group: $F(1, 32) < 3.68$ and $P > 0.08$; Group × Segment: $F(7, 32) < 0.73$, $P > 0.51$) or stellate cells (Group: $F(1, 32) < 0.58$ and $P > 0.72$; Group × Segment: $F(7, 32) < 0.98$, $P > 0.23$), or in the expression of PV in interneurons (Group: $F(1, 32) < 3.02$ and $P > 0.06$; Group × Segment: $F(7, 32) < 1.04$, $P > 0.50$) (w2, w3 and w4 for CNO delivery in a time-unmatched and a time-matched fashion, respectively). Control animals are shown in black; silenced animals in red.

Fig. S13

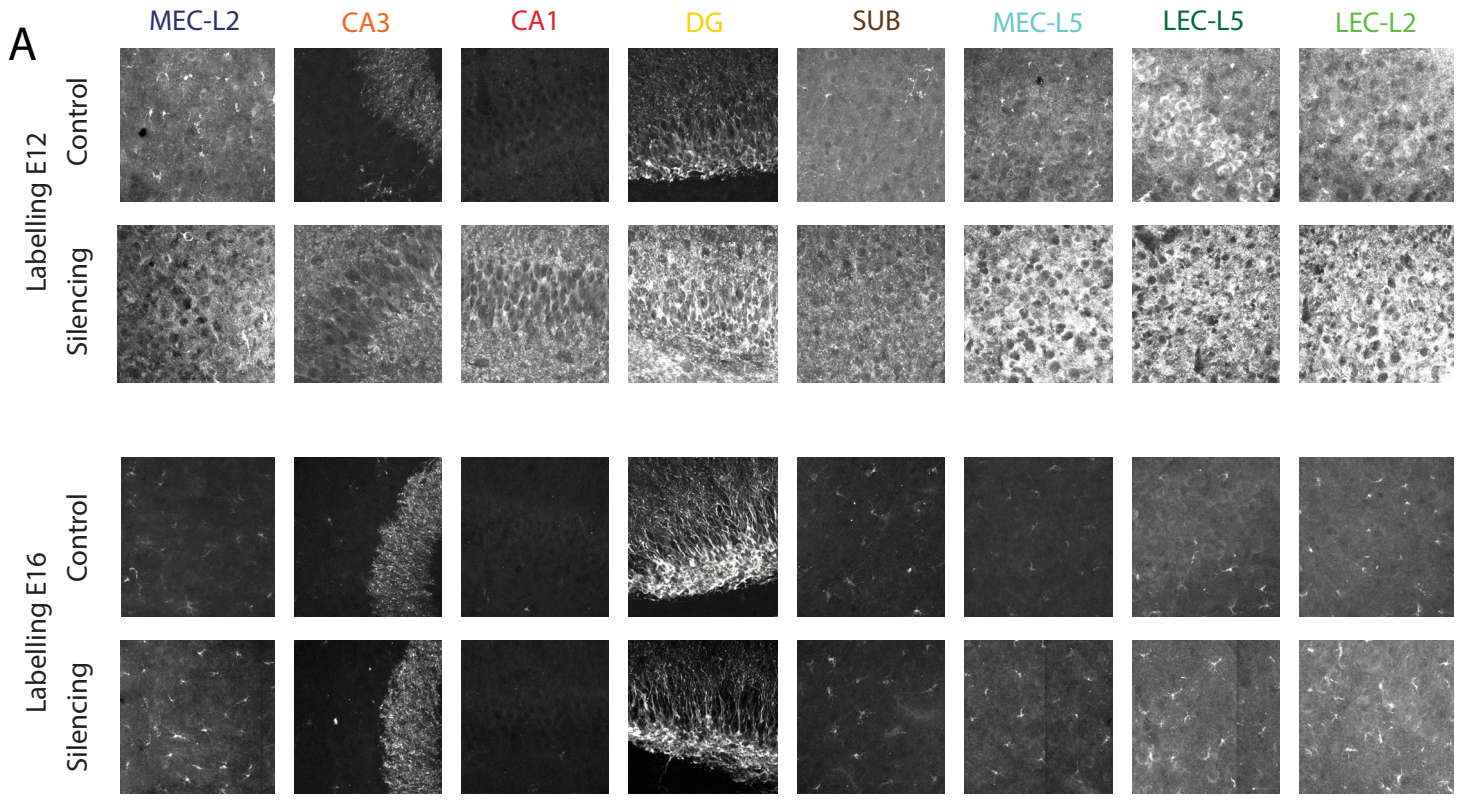
A
MEC-L2
CA3
CA1
DG
SUB
MEC-L5
LEC-L5
LEC-L2
Labelling E12
Control
Silencing
Labelling E16
Control
Silencing

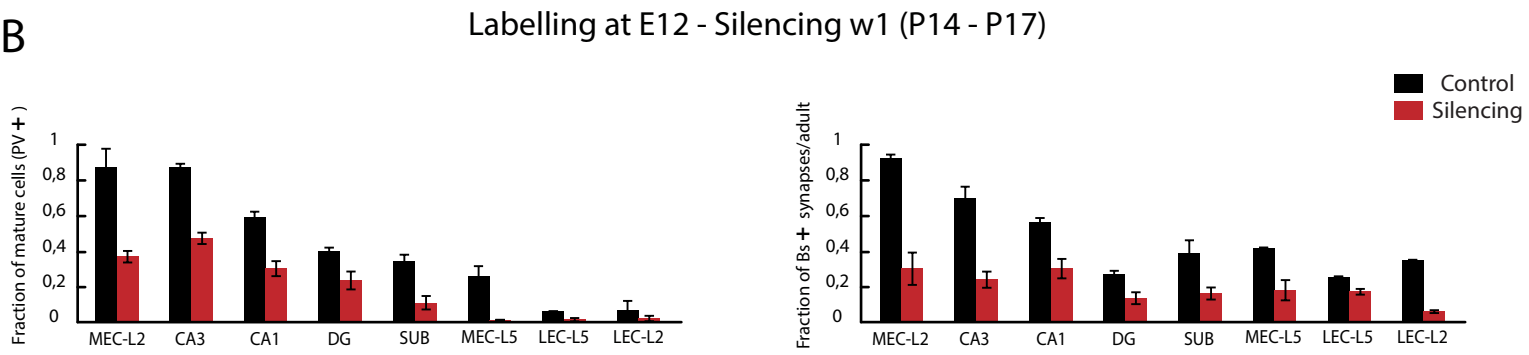
B
Labelling at E12 - Silencing w1 (P14 - P17)
Control
Silencing
Fraction of mature cells (PV +)
Fraction of Bs + synapses/adult
1
0,8
0,6
0,4
0,2
0
MEC-L2
CA3
CA1
DG
SUB
MEC-L5
LEC-L5
LEC-L2

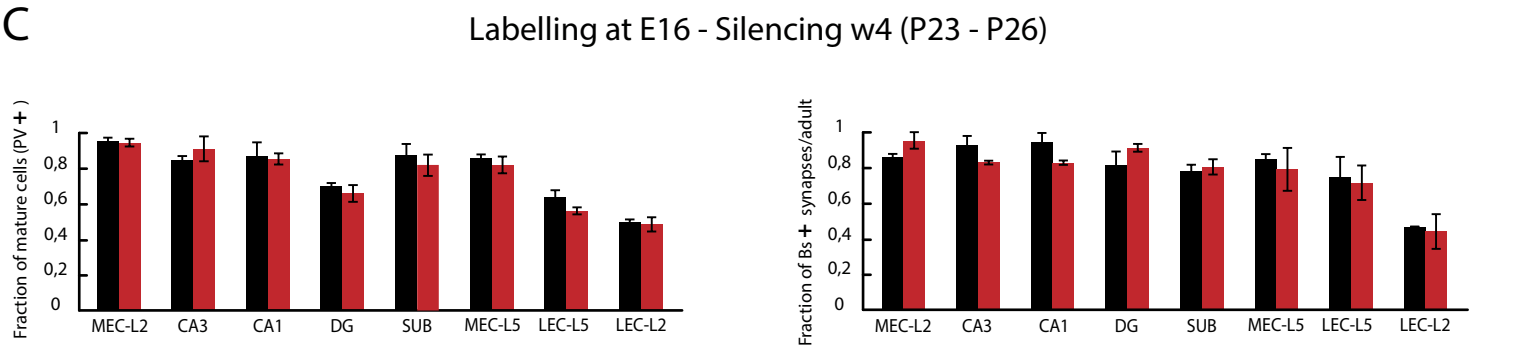
C
Labelling at E16 - Silencing w4 (P23 - P26)
Fraction of mature cells (PV +)
Fraction of Bs + synapses/adult
1
0,8
0,6
0,4
0,2
0
MEC-L2
CA3
CA1
DG
SUB
MEC-L5
LEC-L5
LEC-L2

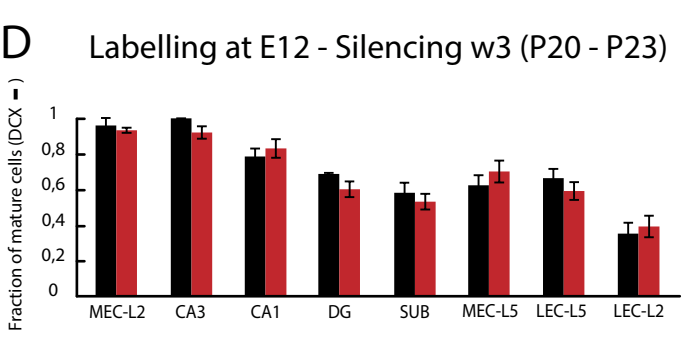
D
Labelling at E12 - Silencing w3 (P20 - P23)
Fraction of mature cells (DCX -)
1
0,8
0,6
0,4
0,2
0
MEC-L2
CA3
CA1
DG
SUB
MEC-L5
LEC-L5
LEC-L2

Fig. S13: PV expression and synaptic density after developmental silencing of either stellate or pyramidal cells.

(A) Maximum intensity projections from confocal images showing DCX expression (white) across subregions of the entorhinal-hippocampal circuit after selective silencing of stellate cells (upper 2 rows) or pyramidal cells (lower 2 rows). Single fields of view were acquired with a 40×/1.3NA oil immersion objective (zoom 0.6×), and processed together with constant parameters. Note that silencing a small portion of stellate cells located in MEC-L2 was sufficient to induce an effect on the development of the extended circuit. This results rules out the possibility that the block of maturation caused by pharmacogenetic silencing might be due to cell-autonomous artifacts caused by the activation of the hM4D(gi) receptor in infected cells. (**B**) Fraction of PV expressing cells (left) and density of bassoon puncta (right) across areas of the entorhinal-hippocampal network following silencing of E12-labelled neurons (predominantly stellate cells) at P14-P17. Analysis at P17. Stellate-cell specific silencing prevented the maturation-related increase in PV expression and synaptic densities across the whole entorhinal-hippocampal network. Silenced groups and control groups were compared with Student's t-test. PV cells: $t > 6.2$ and $P < 0.01$, with the exception of LEC-L5 and LEC-L2 where $t < 0.13$ and $P > 0.15$. Bs+ puncta: all pairwise comparisons with Student's t-test were significant ($t > 4.7$ and $P < 0{,}01$). (**C**) Fraction of PV expressing cells (left) and density of bassoon puncta (right) following silencing of E16-labelled neurons (predominantly pyramidal cells) at P23-P26. Analysis at P26. Silencing isochronic pyramidal cells did not exert any effect on maturation of the entorhinal-hippocampal network. Neither PV expression (left panel), nor densities of synaptic puncta (right panel) were different from controls in any area of the entorhinal-hippocampal network (no comparisons were significantly different, $t < 1.03$ and $P > 0.34$). (**D)** Fraction of DCX– cells upon silencing of isochronic cohorts dominated by stellate cells (E12-born; mean ± S.D.). Cells were silenced at P20-P23 and analyzed at P23. DCX expression in silenced animals was indistinguishable from that of controls ($t < 2.41$ and $P > 0.72$), similarly to what was obtained along the dorso-ventral axis of MEC (Fig. S11C). Analysis was conducted with similar control groups and a similar number of neurons and animals as in (B).

Fig. S14

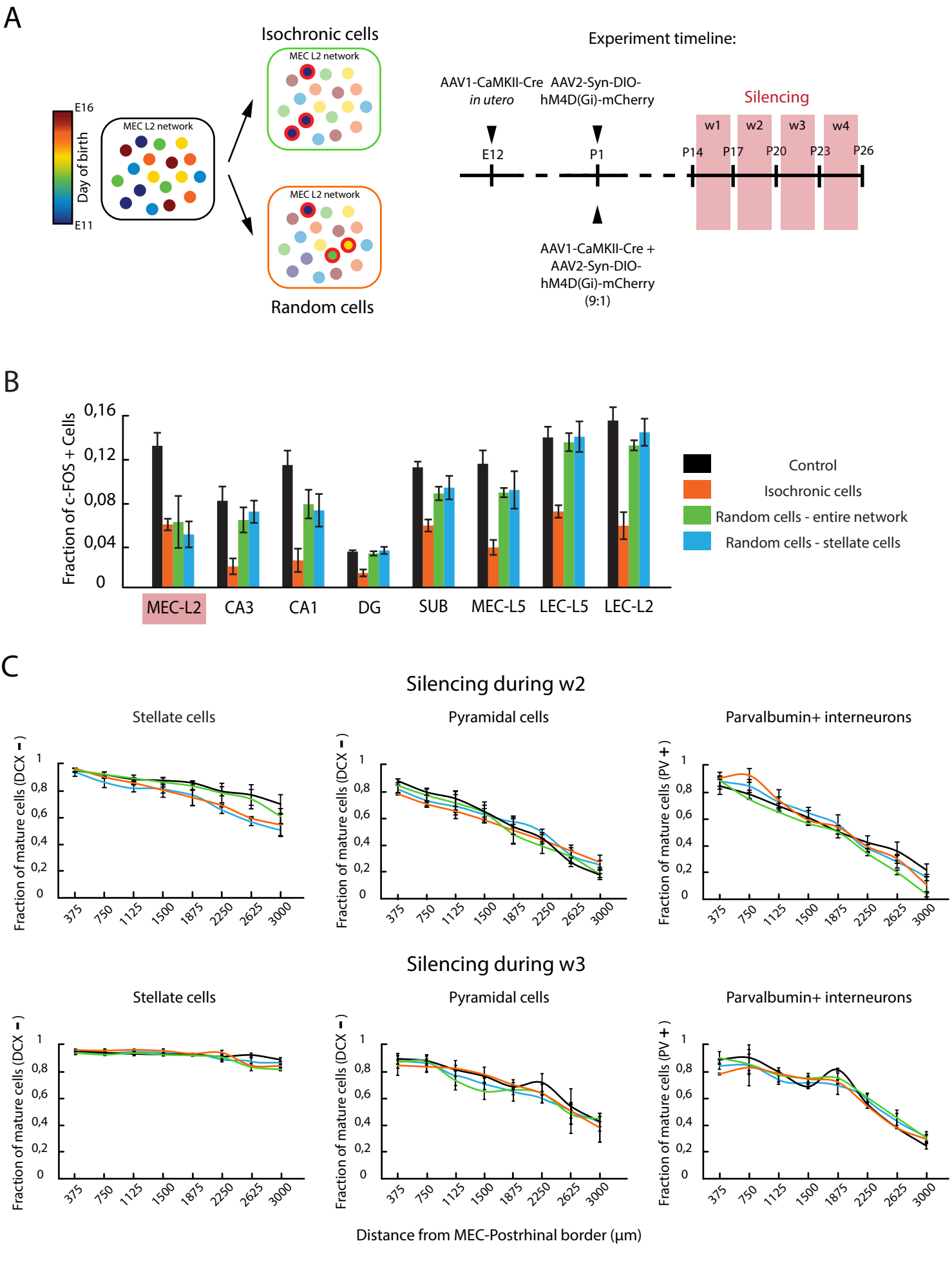
A
Isochronic cells
MEC L2 network
E16
Day of birth
E11
MEC L2 network
MEC L2 network
Random cells
Experiment timeline:
AAV1-CaMKII-Cre
in utero
AAV2-Syn-DIO-
hM4D(Gi)-mCherry
Silencing
w1
w2
w3
w4
E12
P1
P14
P17
P20
P23
P26
AAV1-CaMKII-Cre +
AAV2-Syn-DIO-
hM4D(Gi)-mCherry
(9:1)
B
Fraction of c-FOS + Cells
0,16
0,12
0,08
0,04
0
MEC-L2
CA3
CA1
DG
SUB
MEC-L5
LEC-L5
LEC-L2
Control
Isochronic cells
Random cells - entire network
Random cells - stellate cells
C
Silencing during w2
Stellate cells
Pyramidal cells
Parvalbumin+ interneurons
Fraction of mature cells (DCX +)
Fraction of mature cells (PV +)
1
0,8
0,6
0,4
0,2
0
375
750
1125
1500
1875
2250
2625
3000
Silencing during w3
Stellate cells
Pyramidal cells
Parvalbumin+ interneurons
Distance from MEC-Postrhinal border (µm)

Fig. S14: Isochronic cohorts of stellate cells act synergistically on microcircuit maturation.

(**A**) Schematic illustrating experiment to test for synergistic effects of isochronic stellate cells on microcircuit maturation. Left: schematic of MEC layer 2 network. Every circle represents a neuron. Neurons with the same color share the same birthdate. Circles with a red border indicate neurons infected by the viral mix. In one experiment, we silenced the isochronic cohort of MEC-L2 excitatory cells born at E12. In another, we silenced a comparable fraction of neurons whose labelling was independent of neurogenesis (i.e. random cells). The E12 isochronic cohort was primed for silencing by injecting AAV1-CaMKII-Cre *in utero* as previously described. Infected cells were then targeted with the Cre-dependent virus AAV2-Syn-DIO-hM4D(Gi)-mCherry at P1 ("Isochronic Cells"). To label a comparable fraction of neurons randomly ("Random Cells"), we injected a viral mix postnatally in order to avoid any bias of birthdating (AAVs are not intrinsically tropic for cells based on birthdate, and the probability of infecting a cell more likely reflects viral titer and proximity to the site of injection). A mix containing AAV1-CaMKII-Cre and AAV2-Syn-DIO-hM4D(Gi)-mCherry was injected at P1. The two viruses were mixed in proportions that allowed labelling of a sparse population of excitatory cells in MEC-L2 (proportion in the mix was 9:1 for the Cre-carrying and the Cre-dependent viruses, respectively). CNO was delivered by subcutaneously implanted minipumps during multiple windows of microcircuit maturation (w1 to w4, corresponding to P14-P17, P17-P20, P20-P23, and P23-P26, respectively). Each mouse received CNO for a single window, selected from the set of consecutive windows that were included to make sure that the lack of an effect on development could be attributed specifically to the ontogeny of the cells silenced. (**B**) Fraction of NeuN+ neurons exhibiting nuclear expression of c-FOS (c-FOS+) across subdivisions of the transverse entorhinal-hippocampal circuit in control animals (black) and silenced animals (silencing performed in w1. Orange: silencing of isochronic cells born on E12; green: silencing of a comparable fraction of excitatory neuron in MEC-L2 independently of their molecular identity, referred to as "Random cells – entire network"; blue: silencing of a comparable fraction of stellate cells in MEC-L2, referred to as "Random cells – stellate cells". *y* axis: Fraction of double positive NeuN/c-FOS neurons. 0: no neuron expresses c-FOS; 1: all neurons express c-FOS). Note that DREADD-mediated silencing induced a decrease in the fraction of cells expressing c-FOS throughout the entorhinal-hippocampal network only when isochronic cells were silenced, and not if random cells were targeted. Note also that upon silencing, MEC-L2 exhibited a decrease in c-FOS expression in every silencing group, $t > 6.92$ and $P < 0.01$). (**C**) The effect of silencing on DCX– and PV+ neurons was specific to the early window of

circuit maturation (w1) as no effect could be observed when CNO was delivered at later time points (w2 and w3). Note how, for DCX expression in stellate and pyramidal cells and for PV expression in interneurons, the curves for random, isochronic and control groups overlap for CNO delivery during either w2 or w3 (comparison between control, isochronic and random groups; 2-way ANOVA with Group and Segment as factors for all combinations among CNO delivery windows: Group: $F(1,32) < 3.40$; $P > 0.08$; Group × Segment: $F(7, 32) < 3.82$, $P > 0.21$).

Supplementary references:

54. J. M. Wojtowicz, N. Kee, BrdU assay for neurogenesis in rodents. *Nature protocols* **1**, 1399 (2006).

55. F. Donato, S. B. Rompani, P. Caroni, Parvalbumin-expressing basket-cell network plasticity induced by experience regulates adult learning. *Nature* **504**, 272 (Dec 12, 2013).

56. C. Varga, S. Y. Lee, I. Soltesz, Target-selective GABAergic control of entorhinal cortex output. *Nature neuroscience* **13**, 822 (Jul, 2010).